

AN ABSTRACT OF THE THESIS OF

Michael A. VanderPutten for the degree of Master of Science in Mechanical Engineering presented on May 5, 2017.

Title: Evaluation of the Predictive Capability of Two-Phase Flow Maps for Microchannel Condensation of R-134a at Low Mass Flux Conditions

Abstract approved:

Brian M. Fronk

Predicting condensation flow regimes and the associated heat transfer and pressure drop in microchannels is critical for designing terrestrial and space systems for heating, cooling, power generation, and advanced manufacturing. It is well established that in flows approaching the microscale ($D_h < 1$ mm) gravity-dominated flow regimes become less relevant, with stratified and wavy flows being replaced by the intermittent and annular regimes. While a large body of work has been developed to investigate fluid behavior in microscale channels, past research has focused primarily on adiabatic air-water studies at relatively high superficial velocities or condensing refrigerants at large mass fluxes ($G > 100$ kg-m⁻²-s⁻¹). Fluid visualization results from these studies have been used to develop many of the flow regime maps currently available for estimating heat transfer and pressure drop. Review of these flow maps shows that at microscale channel diameters and low mass fluxes, common flow regime predictions begin to break down.

In the current research, two-phase flow regime data is obtained via high-speed visualization of condensing flows of R-134a at mass fluxes from 80 to 150 kg-m⁻²-s⁻¹ in square microchannels ($D_h = 840$ μm) at quality ranging from 0.01 to 0.60. A relatively small experimental uncertainty in thermodynamic quality ($U_{avg} \approx 3\%$) was maintained by enforcing a large temperature difference across the water-side ($\Delta T > 10^\circ\text{C}$). To mitigate maldistribution in the channels, vapor enters the test section superheated and is condensed to the desired quality before entering the viewing section. All data points were found to be either wavy or wavy-annular flow, and did not compare well to predictions made by commonly used flow regime maps for both micro and macro channel flow. Additional research is required to better understand the characteristics of low mass-flux two phase flows in microchannel geometries.

©Copyright by Michael A. VanderPutten
May 5, 2017
All Rights Reserved

Evaluation of the Predictive Capability of Two-Phase Flow Maps for Microchannel
Condensation of R-134a at Low Mass Flux Conditions

by
Michael A. VanderPutten

A THESIS

submitted to

Oregon State University

in partial fulfillment of
the requirements for the
degree of

Master of Science

Presented May 5, 2017
Commencement June 2017

Master of Science thesis of Michael A. VanderPutten presented on May 5, 2017

APPROVED:

Major Professor, representing Mechanical Engineering

Head of the School of Mechanical, Industrial, and Manufacturing Engineering

Dean of the Graduate School

I understand that my thesis will become part of the permanent collection of Oregon State University libraries. My signature below authorizes release of my thesis to any reader upon request.

Michael A. VanderPutten, Author

ACKNOWLEDGEMENTS

I would like to express my sincere gratitude to Dr. Brian Fronk for his direction, support, and perseverance throughout this project. I came to this project to learn, and he shaped his goals accordingly to see that I succeeded. The guidance I received not only during my successes, but also during my failures, was an invaluable resource during my studies and one I cannot thank him enough for.

I would also like to acknowledge Dr. Javier Calvo, without whom I never would have begun this journey – and Dr. Nancy Squires, without whom I might have never chose to finish it. Thank you both for believing in me, and providing encouragement along the way.

Thanks are also due my colleagues in both the TEST and CIRE labs, who always offered me support during my research and studies. I owe special thanks to Kyle Zada, Tabeel Jacob, and Aaron Jesse Fillo, for their direct support of my research and encouragement in the face of difficulty. I would also like to thank Michael Polander for his help developing the Ref-Prop to LabVIEW integration programming, which was a great help in my research and a relief not to have to implement myself.

Lastly, I would like to thank my family and loved ones, who were always there for me when I needed to take a break, and who pushed me back to the task at hand when I had rested too long.

TABLE OF CONTENTS

	<u>Page</u>
1 Introduction	1
1.1 Flow Regimes	1
1.2 Applications of Low Mass-Flux Systems.....	2
2 Literature Review	4
2.1 Two-Phase Flow Regime Studies	4
2.1.1 Early Flow Regime Maps	4
2.1.2 Macroscale and Microscale Flow Transition	6
2.1.3 Varying Fluid Studies	7
2.2 Flow Regime Maps	9
2.2.1 Quantitative and Qualitative Observation.....	9
2.2.2 Available Flow Regime Maps and Transition Criteria	11
2.3 Goals of Current Research.....	15
2.3.1 Available Research.....	16
2.3.2 Research Objectives	18
3 Experimental Design & Instrumentation	19
3.1 Test Section Design	20
3.1.1 Design Methodology	21
3.1.2 Implementation	27
3.2 Working Fluid Loop.....	29
3.3 Cooling Fluid Loop.....	33
3.4 Instrumentation	35
3.4.1 Temperature	35
3.4.2 Pressure.....	36
3.4.3 Flow Rate.....	37
3.4.4 Visualization	38

TABLE OF CONTENTS (CONTINUED)

	<u>Page</u>
4 Data Collection and Analysis	39
4.1 Data Collection	39
4.1.1 Data Collection Process	39
4.1.2 Data processing	40
4.1.3 Data Collected.....	43
4.2 Analysis of Uncertainty.....	50
4.2.1 Instrument Uncertainty	51
4.2.2 Measurement Uncertainty.....	51
4.2.3 Variability Uncertainty	53
4.2.4 Additional Sources of Uncertainty	54
4.2.5 Estimated Uncertainty of Calculated Parameters	56
4.3 Analysis of Data	58
4.3.1 Flow Regime Observations.....	58
4.3.2 Comparison to Popular Flow Maps.....	58
4.4 Summary	74
5 Conclusion & Recommendations	75
5.1 Conclusions	75
5.1.1 Experiment.....	75
5.1.2 Setup	76
5.1.3 Results	76
5.1.4 Result Conclusion	76
5.2 Recommendations for Future Work.....	77
6 Sources Cited.....	78
7 Appendix.....	84

LIST OF FIGURES

<u>Figure</u>	<u>Page</u>
Figure 1.1 - Flow regimes recognized in this study	2
Figure 2.1 - Flow regime map proposed by Taitel & Dukler (1976)	12
Figure 2.2 - Map of currently available microscale flow visualization studies.....	17
Figure 3.1 - Schematic of experimental system with important state points labeled	19
Figure 3.2 - Fully assembled flow loop as run for experimental data (test section photographed before being insulated). Test section pictured to the left, downstream components pictured at right.	20
Figure 3.3 - Test section concept design.....	21
Figure 3.4 - Heat exchanging plate and flow channels.....	25
Figure 3.5 - Model of the experimental test section	26
Figure 3.6 - Sample channel depth measurement (axes not displayed to scale)	28
Figure 3.7 - Schematic of working fluid loop with labeled state points	29
Figure 3.8 - Diagram of vaporizer operation	31
Figure 3.9 - Tube-in-tube heat exchanger used for the post-condenser.....	32
Figure 3.10 - Cooling fluid loop configuration. Water shown as a solid line, ethylene-glycol as a dashed line. State points are shown as circumscribed letters	33
Figure 3.11 - Thermocouple incorporated into compression fitting for measuring flow temperature	35
Figure 3.12 - Operation of DEA Nutating flowmeter (DEA 2016).....	37
Figure 3.13 - Visualization set up used for data capture during experiment	38
Figure 4.1 - Control volume analyzed for heat transfer.....	42
Figure 4.2 - Collected data from both saturation temperatures, heat loss estimations and uncertainty incorporated into mass flux and quality estimations	43
Figure 4.3 - Visualization of intermittent flow, as captured during initial experimentation heater testing	45
Figure 4.4 - Comparing visualization results while varying saturation temperature.....	46
Figure 4.5 - Comparing visualization results while varying flow quality	47
Figure 4.6 - Comparing visualization results while varying mass flux	48
Figure 4.7 - DAQ systems diagram.....	50
Figure 4.8 - Heat map developed for working fluid operation.....	55
Figure 4.9 - Sample EES results from Kline-McClintock uncertainty analysis.....	57

LIST OF FIGURES (CONTINUED)

<u>Figure</u>	<u>Page</u>
Figure 4.10 - Experimental data plotted against the Taitel and Dukler (1976) proposed map	61
Figure 4.11 - Experimental data ($T_{\text{sat}} = 40^{\circ}\text{C}$) plotted against the Cavallini et al. (2002) proposed map at that temperature.....	63
Figure 4.12 - Experimental data ($T_{\text{sat}} = 55^{\circ}\text{C}$) plotted against the Cavallini et al. (2002) proposed map at that temperature.....	64
Figure 4.13 - Experimental data ($T_{\text{sat}} = 40^{\circ}\text{C}$) plotted against the El Hajal et al. (2003) proposed map at that temperature	66
Figure 4.14 - Experimental data ($T_{\text{sat}} = 55^{\circ}\text{C}$) plotted against the El Hajal et al. (2003) proposed map at that temperature	67
Figure 4.15 - Experimental data ($T_{\text{sat}} = 40^{\circ}\text{C}$) plotted against the Kim & Mudawar (2012) proposed map at that temperature.....	69
Figure 4.16 - Experimental data ($T_{\text{sat}} = 55^{\circ}\text{C}$) plotted against the Kim & Mudawar (2012) proposed map at that temperature.....	70
Figure 4.17 - Experimental data ($T_{\text{sat}} = 40^{\circ}\text{C}$) plotted against the Nema et al. (2014) proposed map at that temperature	72
Figure 4.18 - Experimental data ($T_{\text{sat}} = 55^{\circ}\text{C}$) plotted against the Nema et al. (2014) proposed map at that temperature	73

LIST OF TABLES

<u>Table</u>	<u>Page</u>
Table 2.1 - Studies showing the critical bond number under which surface tension forces begin to gain significance	6
Table 2.2 - Review of available flow visualization literature	16
Table 3.1 - Representative numbers used in calculations below for $G = 15 \text{ kg m}^{-2} \text{ s}^{-1}$ and $x = 0.5$	23
Table 3.2 - Relevant nominal test section dimensions	27
Table 3.3 - Stock used in machining the test section.....	27
Table 3.4 - As-machined dimensions of microchannel heat exchanger	28
Table 3.5 - Elements used in fluid loop assembly.....	33
Table 3.6 - Elements used in cooling-fluid loop assembly	34
Table 3.7 - Thermocouple calibration results	36
Table 4.1 - Collected data from both saturation temperatures	44
Table 4.2 - Instrument level uncertainty as reported by the manufacturer	51
Table 4.3 - Data acquisition level uncertainty	53
Table 4.4 - Flow transition criteria for the Taitel and Dukler flow map.....	60
Table 4.5 - Flow transition criteria for the Cavallini et al. (2002) flow model.....	62
Table 4.6 - Flow transition criteria for the El Hajal (2003) flow model.....	65
Table 4.7 - Flow transition criteria for the Kim & Mudawar flow model	68
Table 4.8 - Microscale transition criteria as proposed by Nema et al. (2014)	71
Table 4.9 - Summary of flow regime predictions by maps investigated	74
Table 7.1 - Measured and calculated values of data points used in study	84

To Kayla

*Thank you for your endless support, and unyielding encouragement,
you mean the world to me – to mars and back again*

1 INTRODUCTION

As the ability to accurately and affordably manufacture microscale flow channels grows, so does the drive to better understand and predict the operation of these systems. While a substantial body of work has been developed investigating pressure drop and heat transfer in macroscale flow systems, little focus has been devoted, until recently, to microscale systems. This thesis seeks to establish a base of empirically collected data detailing low mass flux microscale multi-phase fluid flow in order to evaluate the accuracy of currently accepted flow models as applied to low mass-flux systems.

1.1 FLOW REGIMES

The subject of two-phase flow regimes in tubes has been extensively studied due to its importance in oil and gas, power generation, chemical processing, and other industries. The structure and distribution of liquid and vapor phases in a system strongly influences pressure drop and the transfer of heat and mass between fluids. These physical structures of flow can be classified into different flow regimes, and are crucial in the design of multi-phase flow systems. Knowing the local flow regime, appropriate mechanistic models can be developed to accurately predict these transport phenomena. To aid in predicting two-phase flow regimes, researchers often develop flow regime maps which provide a correlation between some set of parameters and the local structure of liquid and vapor flowing through a channel. Some of these maps are developed empirically from databases, while others are based principally in theory, with experimental data used only as a validation. The focus of this study is on understanding the two-phase flow regimes of condensing low surface tension fluids in microchannels.

There exists a wide variety of flow regimes that have been previously catalogued and sub-divided by several different research groups. For the purposes of this study, the flow regimes considered will be limited to those shown below in Figure 1.1. These regimes were chosen as the heat and mass transport in each regime would require a significantly different mechanistic approach in macro and micro channels.

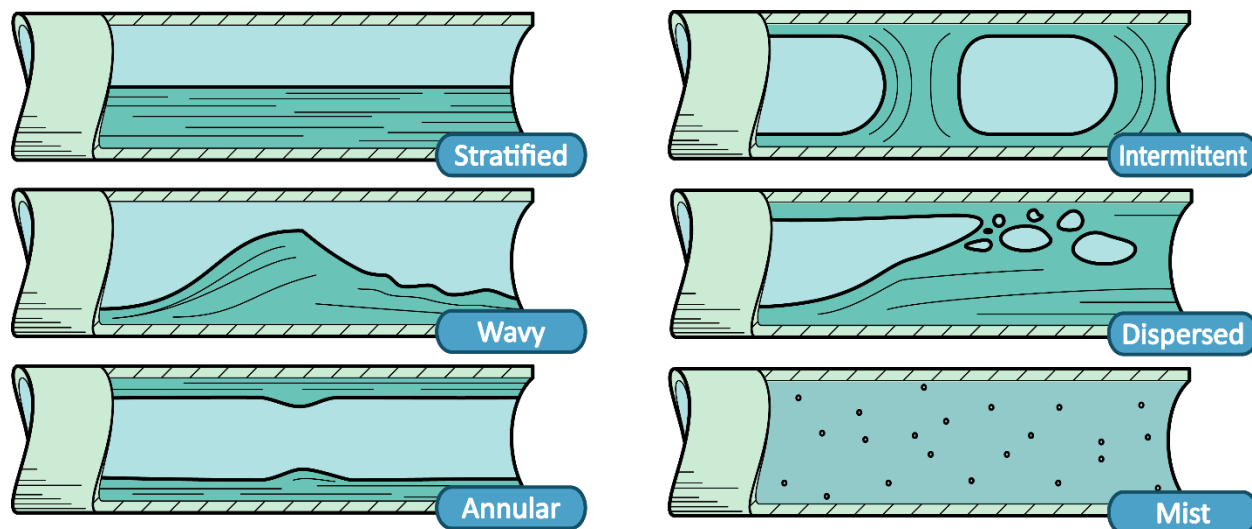


Figure 1.1 - Flow regimes recognized in this study

1.2 APPLICATIONS OF LOW MASS-FLUX SYSTEMS

Until more recently, the primary focus of microscale multiphase flow research was on relatively high mass fluxes of liquid and vapor, useful in designing high heat-load thermal management devices for electronics cooling applications. As the manufacturability of microchannels has increased and systems trend towards higher efficiency, focuses have shifted towards microchannel applications in much larger heat exchangers. To maintain a reasonable pressure drop, this requires investigation of the low mass-flux flow space, with a variety of new applications.

One application of interest is in the aerospace sector. As space-faring crafts become more prevalent and various industries are finding it profitable to develop manned crafts for spaceflight, the design of robust and lightweight life-support systems is quickly becoming a priority. Unlike their terrestrial counterparts, systems designed for rejecting heat to space must not be dependent on gravity or any fluid medium surrounding the craft. Additionally, due to the immense cost per unit payload mass, these systems are required to be as light as possible. Capillary Pumped Loops (CPLs) address many of these design concerns without the drawback of using heavy pumps, making them appealing for use in both manned and unmanned spacecraft. The CPL operates passively through use of an evaporator, drawing fluid through the system using surface tension and two-phase heat transfer.

An investigative study presented by VanderPutten (2016) explored the use of fifteen different fluids for heat rejection on a small manned spacecraft. The fluids investigated ranged from refrigerants such as R-134a to common fuels such as propane or isobutane. It was found that for the fluids involved, system mass flux through the microchannel radiative condenser investigated was on the order of $5 < G < 80 \text{ kg m}^{-2} \text{ s}^{-1}$.

The conclusion of the investigation was that given the system requirements and the thin design margins associated with space-faring systems, additional research and more accurate models were required for the design of efficient two-phase microchannel flow and heat transfer at such low mass flow rates and available pressure differentials.

Another application area is in process intensification of the production of chemical products. There are significant efforts underway to decrease reactor size and efficiency and render large industrial chemical processing plants most commonly operated today an artifact of the past. Processes commonly conducted in large vats are now able to take advantage of the order of magnitude higher surface area to volume ratio in microscale reactors, cutting processing time down to a fraction of the reactor footprint and timescale previously required.

One of the drawbacks of such scaling processes is the relative imbalance of surface area to residence time when brought to the microscale. Reactions that were previously surface area limited are now an order of magnitude more limited by the residence time required in the now microscale reactor vessel. When scaling the decomposition of hydroxylammonium nitrate (HAN), an energetic ionic fluid useful as either a mono or bi-propellant rocket fuel, Chai et al (2016) investigated microscale manufacturing using electrode-infused wafers with $D_h = 0.33$ mm microchannels. The study found that the flowrate that produced the ideal residence time for full reaction of HAN decomposition lied in the range of $0.002 < G < 0.012$ kg m⁻² s⁻¹, scaling the time reactants are in the reactor to match that required to fully react.

Similarly, Mas & Günther (2003) investigated the fluorination of toluene, a process previously near impossible to perform due to the extremely exothermic reaction, using a microchannel reactor. On the microscale, the heat produced by the exothermic reaction is more easily mitigated due to the increased surface area per volume of the heat exchanger, as well as the relatively small amount of energy produced by the reaction when confined to $D_h = 0.23$ mm channels. Interested in increasing the residence time in order to most efficiently react the system charge, the study investigated mass fluxes on the order of $0.5 < G < 5$ kg m⁻² s⁻¹, with the hope of identifying flow regimes and providing a novel process for the direct fluorination of aromatics.

The attractiveness of microchannel systems, both in single and multi-phase flow lies in the relative gains in effective surface area per unit volume. The downside of these systems is that with the increase in effective surface area comes an increase in flow friction as well, bringing about a substantial parasitic pressure drop in high mass-flux applications. To better understand the operation of low mass-flux systems a more detailed understanding of the flow regime physics – specifically the interaction of microscale and low mass flux on flow regimes – is required at these flow conditions. The present study seeks to evaluate commonly accepted

flow regime models at microchannel and low mass flux conditions against empirically collected data in order to inform the validity of the models in such an application.

2 LITERATURE REVIEW

In this chapter, a review of prior work on adiabatic and diabatic two-phase flow regime studies and flow regime map development is presented to illustrate the theoretical basis and provide motivation for the present work. Table 2.2, at the end of this chapter summarizes the studies presented and the experimental variables investigated in each study. Due to the extensive study of multi-phase flow through different disciplines, a wide variety of labels have been used to describe the same flow regimes by different authors. To facilitate the discussion of the works below, all reviews of flow regimes will be transcribed from the original works to follow the regime descriptions in the the flow diagram presented above in Figure 1.1. In the present study it is expected that the transitions between annular and intermittent flows are most significant due to the relative impact of those flows on condensation heat transfer and pressure drop in microchannels.

2.1 TWO-PHASE FLOW REGIME STUDIES

Among the first flow regime studies, adiabatic gas-liquid mixtures (commonly air and water mixtures) were originally popular due to the ease of conducting experiments with readily available fluids at atmospheric pressure. The section below details some of the work done to gain a principle understanding of flow physics, and the development of the first flow maps.

2.1.1 EARLY FLOW REGIME MAPS

Gas-oil studies by Baker (1954) resulted in one of the very first flow maps. He plotted the transitions between stratified, wavy, intermittent, annular, and dispersed flow on axes of gas mass flux, and mass flux ratio between liquid and gas. The map was developed to be applicable to flow in oil pipelines, and was built from flow data from large diameter tubes ($150 < D_h < 200$ mm). His map did not explicitly include tube diameter effects in the transition criteria.

A decade later, Griffith & Lee (1964) published flow regime data on air water flows in much smaller diameter tubes ($D_h = 1$ mm, similar to those in the present study). Significantly, they found that their data did not match the trends found in Baker's first works developed for much larger tubes. They proposed that surface tension forces in annular flows pull wave troughs to the center of the tube, forcing a liquid slug to bridge the diameter of the tube and form an intermittent flow. Building off of the discrepancy between the findings of two wildly different sizes of tubes, research by Mandhane et al. (1974a) built off of the work by

Govier and Aziz (1972) to suggest transition lines that shift with tube diameter plotted on the axes of superficial gas and liquid velocity (j_v and j_l), calculated as the artificial flow velocity were that phase the only one occupying the entire cross-sectional flow area.

Taitel & Dukler (1976) developed a theoretically-based flow map with transitions defined by a set of five dimensionless parameters, taking into account diameter, buoyancy effects, and wave stability – but neglected the effects of fluid surface tension. The theoretical model describes the transition from stratified to wavy to dispersed flow through the interaction of pressure and gravity on the wave trough. The map found good agreement with the Mandhane et al. (1974a) flow map and empirical air-water data in pipes ($13 < D_h < 50$ mm). Due to its theoretical origin, many modern maps make use of the parameters developed in this study as a foundation.

Working to better define the role of surface tension forces in two-phase flow physics, Barnea et al. (1983) proposed that for small diameter tubes the transition from annular to intermittent flow can be modeled by comparing the relative magnitude of body and surface tension forces. They proposed a modification to the original function to predict equilibrium (stratified) vapor layer thickness proposed by Taitel & Dukler (1976) to include a balance between body and surface tension forces. The modified approach agreed well with empirical results of air-water in smaller diameter tubes ($4 < D_h < 12$ mm), showing that at the smaller diameters surface tension forces will determine the stratified-intermittent transition, while in large diameters the Kelvin-Helmholtz instability factor dominates.

Upon investigating even smaller diameter tubes ($1 < D_h < 5$ mm), other authors observed only annular, intermittent, and dispersed bubble flows (Damianides and Westwater 1988; Fukano, Kariyasaki, and Kagawa 1989). Stratified or wavy flows were absent in the study findings, and flows transitioned from annular directly to intermittent flows. Damianides & Westwater (1988) concluded that surface tension plays a much larger role in small diameter tubes, but made no distinction of where the micro to macro transition boundary may lie.

The physical effects of surface tension in establishing flow regime can be seen in Figure 2.1 below, demonstrating how surface tension can act to draw wave crests together. The surface tension can be described as the affinity of the fluid to form the least amount of surface area possible, or in the case of an enclosed tube, to knit together any wave troughs into a continuous liquid slug. With an increase in surface tension, the affinity to form slugs or solid lengths of un-broken liquid increases. The same can be said for a decrease in tube diameter with a constant surface tension – as the magnitude of surface tension forces increases with decreasing length scale, the force required to close the liquid bridge decreases.

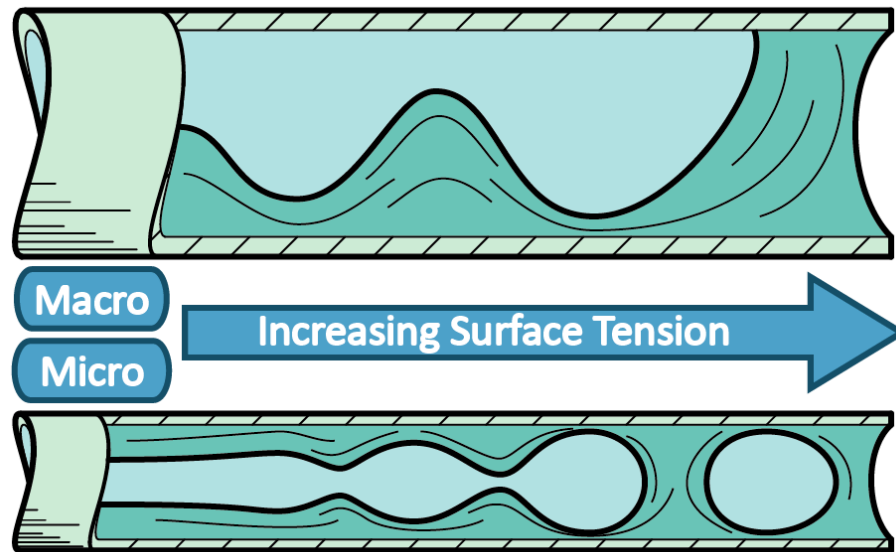


Figure 2.1 - Figure demonstrating the effect of growing surface tension on flow regime

2.1.2 MACROSCALE AND MICROSCALE FLOW TRANSITION

The available research in adiabatic two-phase mixtures had shown that there was a clear difference between maps developed in larger diameter tubes, and those developed in smaller diameters. With the knowledge that surface tension plays an important role in the flow regimes of smaller tubes, research moved to quantify this shift and establish a transition boundary along which the body force of gravity diminished in importance relative to inertial and surface tension forces.

Many studies first looked to the Bond number to establish the size boundary at which surface tension forces become relevant. The Bond number is a relation of the magnitude of surface and body forces on a fluid – with values less than unity indicating the prevalence of surface tension forces. Table 2.1 below shows three differing studies that sought to define the Bond number at which the microscale forces became significant. The table shows what each study found that Bond number to be, how it was found, and what that number means in terms of a tube diameter for both refrigerant ($T_{\text{sat}} = 40^{\circ}\text{C}$) and air-water flows.

Table 2.1 - Studies showing the critical bond number under which surface tension forces begin to gain significance

Study	Bo_{crit}	Methodology	$D_{\text{AIR-H}_2\text{O}}$	$D_{\text{R-134a}}$
F.P.Bretherton (1961)	0.84	Size of capillary tube in which Taylor bubbles no longer freely rise in a vertical water-filled tube	2.50 mm	0.71 mm
Suo & Griffith (1964)	0.88	Point at which body forces cease influencing the flow in capillary tubes.	2.56 mm	0.73 mm
Brauner & Maron (1992)	$(2\pi)^2$	Analysis of the stability of stratified/non-stratified boundary transition for small tube sizes	17.13 mm	4.90 mm

Table 2.1 shows that by using the dimensionless Bond number as a transition criterion, the diameter at which “microscale” effects become important is strongly dependent on the fluid of interest. For low surface tension fluids like R-134a, the transition diameter is much smaller than for high surface tension air-water mixtures. In the present study, the hydraulic channel diameter is 0.84 mm, suggesting it is either near or below the critical Bond number limit, depending on the transition criteria considered.

In support of the investigation of transition between micro and macro scale flows, Coleman & Garimella (1999) studied the effect of aspect ratio ($0.725 < \alpha < 1$), and hydraulic diameter ($1.3 < D_h < 5.5$ mm) on air and water flows in circular and rectangular tubes. The study showed that when comparing flows in small tubes (Damianides and Westwater 1988; Fukano, Kariyasaki, and Kagawa 1989) and large tubes (Weisman et al. 1979; Taitel and Dukler 1976), maps developed for small tubes showed significant discrepancies when compared to the maps developed for the larger ones. The study found that for air-water mixtures, surface tension and hydraulic diameter begin to play a significant role in regime transitions when $D_h < 10$ mm. The trend was observed that for decreasing tube diameters, the transition to dispersed flow shifts to higher superficial liquid velocities due to an increase in surface tension effects. They also showed that at similar hydraulic diameters rectangular and round tubes will have different transition characteristics as liquid is drawn into sharp channel corners, concluding that channel geometry becomes significant as the relative strength of surface tension forces increases.

At the same time, Triplett & Ghiaasiaan (1999) studied air water flow regime transitions in circular and triangular single-channel test sections ($1.09 < D_h < 1.49$ mm) with experimental flow regime results in good agreements with similar studies (Damianides and Westwater 1988; Fukano, Kariyasaki, and Kagawa 1989). The results were compared with poor agreement to the models proposed by Mandhane et al. (1974b) and Suo & Griffith (1964), and with only some agreement to those proposed by Taitel & Dukler (1976) and (Barnea et al. (1983). The experiment confirmed, along with many others, that no stratified flow was observed at those channel diameters and that existing models were incapable of accurately predicting the expected flow regimes.

2.1.3 VARYING FLUID STUDIES

The studies in the previous sections show a heightened importance of surface tension forces in small channels. Thus, it becomes clear that for microscale geometry flows, the system geometric variables and fluid properties become important for predicting two-phase flow regimes. Furthermore, Table 2.1 shows that the transition to “microscale” is highly dependent on the specific fluid. Thus, some of the results of air-water experiments would not be expected to scale to low surface tension refrigerant systems.

Investigating the applicability of air-water flow regime studies to those using refrigerants, Coleman & Garimella conducted some of the first flow visualization experiments with condensing flows of R-134a in circular and rectangular ($1.0 < D_h < 4.9$ mm, $0.5 < \alpha < 2$) tubes (Coleman and Garimella 1999; Coleman and Garimella 2000; Coleman and Garimella 2003). The authors found that for small tubes, channel geometry seems to have less effect than hydraulic diameter, but that their results using R-134a (Coleman and Garimella 2000) are not well predicted using transition lines developed in studies using air-water mixtures (Coleman and Garimella 1999). To quantify this relation, the authors made use of the Froude number, comparing inertial and gravity forces, with values over unity indicating the dominance of the inertial-driven forces. The authors proposed that because many studies have concluded that the wavy-annular transition occurs at a constant Froude number, the transition would shift from fluid to fluid as the inertial effects would differ at similar flow conditions.

Similarly, Yang & Shieh (2001) studied the difference in flow regime patterns between air-water mixtures and condensing flows of refrigerant R-134a in horizontal tubes ($1.3 < D_h < 5.5$ mm). Supporting the findings of Coleman & Garimella (2000), the results showed a dramatic shift in both the annular-intermittent and intermittent-dispersed transitions (described as *slug to annular* and *bubble to plug and slug* respectively). The authors concluded that not only body forces and turbulent fluctuations, but fluid surface tension must play a role in predicting flow regime transitions in small diameter tubes.

Ong & Thome (2010) studied micro and macro scale transition using a series of three tubes and three different refrigerants. They measured top and bottom liquid film thicknesses during horizontal annular flow, and were able to define a transition region from macro to micro scale flow with decreasing hydraulic diameter. By observing the annular flow thickness, they defined a transition in terms of the Confinement number, comparing the top and bottom channel film thickness observed during bubbling and annular flow in uniform and non-uniform cases. The study defined $Co = 0.3 - 0.4$ as the absolute lowest end of macroscale effects, with an upper micro-scale effect limit of $Co \approx 1.0$. For an air-water mixture, this relates to a hydraulic diameter of approximately 2.7 mm. The overlapping middle range is referred to as the mesoscale, and transitions through the effects from both scales until the Co number reaches unity.

Investigating more specifically the heat transfer and pressure drop in systems, Agarwal & Garimella (2010) performed experiments measuring the heat duty and pressure loss in air-water mixtures in an array of ($0.100 < D_h < 0.200$ mm, $\alpha = 0.5$) laser etched copper microchannels at a variety of mass fluxes ($200 < G < 800$ kg m⁻² s⁻¹). It was shown that both pressure drop and heat transfer coefficients increased with increasing vapor quality, increasing mass flux, and decreasing saturation temperature. Results from the study showed poor agreement with popular heat transfer and pressure drop models, citing that most were developed for adiabatic air-water flows in larger tubes or test sections with aspect ratios closer to unity.

Looking at the effect of system geometry using flows representative of those present in microreactors, Waelchli & Rudolf von Rohr (2006) studied gas-liquid flows through square channels in silicon wafers ($0.187 < D_h < 0.218$ mm). Flow regimes were observed using optical visualization through micro-resolution particle image velocimetry. The study showed good agreement with maps developed using triangular or square channels (Triplett and Ghiaasiaan 1999; Zhao and Bi 2001; Coleman and Garimella 1999), but poor agreement with maps developed using round channels (Kawahara, Chung, and Kawaji 2002; Coleman and Garimella 1999). The authors conclude that at microscale lengths and smaller, the fluid and channel geometry effects far outweigh those of channel hydraulic diameter, showing that results from channels over 25 times larger are still able to predict the study results.

The studies above show a clear discrepancy between studies focusing on air-water mixtures, and those focusing on the lower surface tension refrigerants. It was made clear by these studies that the fluid under investigation, specifically the properties such as surface tension and relative phase density differential, played a major role in experimental results.

2.2 FLOW REGIME MAPS

Reviewing available literature, it can be seen that there is still a discrepancy between the prediction of the available models, and the empirical results. While the methods employed in one study might find good agreement in some of the available data, they commonly fall short when compared with the results of a separate study. Previous heat transfer and pressure drop studies have shown that with microchannel flows at decreasing mass fluxes (below approximately $200 \text{ kg m}^{-2} \text{ s}^{-1}$), the discrepancy between model and data grows even wider, especially at lower qualities (Baird, Fletcher, and Haynes 2003; Matkovic et al. 2009; Koyama, Kuwara, and Nakashita 2003). With so few studies investigating flow in the lower mass flux areas of operation, it is difficult to know even what flow regime can be expected for a set of known flow parameters. The investigation into developing accurate flow maps is the driving force behind progressing the accuracy of associated mass and heat transfer models. The current study seeks to evaluate the accuracy of some of these predictive flow regime models, in order to evaluate their use on low mass flux microchannel flows.

2.2.1 QUANTITATIVE AND QUALITATIVE OBSERVATION

In the development of existing flow maps, the data reduction has primarily been performed by manually inspecting frames and images. This is both time consuming and introduces subjectivity in differentiating one flow regime type from another. Due to the difficulty in accurately representing the collected data and often finely divided elements of flow regimes, many have pointed to this subjective cataloging process as a source of uncertainty in the available body of data that is unable to be quantified (Doretto et al. 2013).

Development of the first flow maps were based on relatively simple classifications, such as those shown in Figure 1.1. As maps such as that proposed by Taitel & Dukler (1976) were further refined, by Breber et al. (1980) for example, additional criteria were proposed to further continue the sub-division of flow regimes. Later, research by Dobson & Chato (1998) proposed limiting the number of flow regimes considered to those for which different condensation transport models could be developed. In their investigation, they developed transitions from annular to stratified-wavy, which are particularly important for condensation in large horizontal tubes. Since then, many researchers have been investigating methods of defining flow regimes objectively, allowing them to develop continuums upon which transitional maps could be developed.

A novel method for flow regime classification, developed by Canière et al. (2007), makes use of a capacitance based sensor and analysis of time and frequency domain signals to estimate the given flow regime. A concave pair of capacitance sensors were used to sense differences in permittivity between air and water, and were tuned using geometric flow regime simulants. The method was able to show statistically significant results between observations of four different flow regimes, but still requires the development of a suite of statistical analysis tools to differentiate between flow regimes distinctly. The method's accuracy also hinges on a thin wall thickness within the test vessel, originally developed using atmospheric pressure air-water mixtures.

Seeking a method of more objectively classifying flows, a probabilistic model was developed by (Kawahara et al. (2002), using video footage and analyzing the time averaged flow regime observed at each condition in $D_h = 1$ mm tubes. While the flow regimes were still classified by hand, data points exhibiting multiple flow regimes were weighted based on the frequency of regime occurrence, opposed to being classified as a single dominant flow regime. The results showed similar agreement ($\pm 10\%$) to separate models for both single phase and two-phase friction factor analysis of pressure drop.

Pursuing a similar approach to probabilistic modeling, Jassim et al. developed an approach to probabilistic flow regime mapping, looking at the time fraction each flow regime was present in a condensing tube at each data point (Jassim, Newell, and Chato 2006; Jassim, Newell, and Chato 2007). Pressure drop and heat transfer data for condensing R-134a in a 8.915 mm diameter tube was recorded at mass fluxes between $100 < G < 800$ kg m⁻² s⁻¹, and added to data collected in other studies (Dobson 1994; Sacks 1975). Using a time averaged manual analysis of regime frequency at each data point, probabilistic transition criteria was developed to provide transitions in similar models. Predicted data agreed well with the models presented by Dobson & Chato (1998) and El Hajal et al. (2003) to within a mean absolute deviation of 6%. The authors then proposed a probabilistic heat transfer map that estimated the effect of varying conditions based on the weighted flow regime probability at those conditions. Using the generalized time fraction probability

flow regime map developed in Jassim et al. (2007), with annular flow components developed in Dobson & Chato (1998) and El Hajal et al. (2003), the study predicted condensation heat transfer with a mean absolute deviation of 13%. The development of a probabilistic approach to flow regimes allows for flow regimes to be statistically blurred together based on empirical estimations. While this method does not account for the physics that are causing flow transition, it does allow researchers to develop semi-accurate models informed by data captured from specific experimentation.

Seeking to avoid the subjectivity of manual flow regime classification, Keinath (2012) developed a method of digitally analyzing high speed video and capturing the instantaneous flow regime, void fraction, slug frequency, and vapor velocity in a wide range of tube diameters and mass fluxes ($0.5 < D_h < 3.0$ mm, $200 < G < 800$ kg m⁻² s⁻¹). Use of this data to produce heat transfer and pressure drop models yielded improved models found to agree with condensation data from both carbon dioxide and ammonia. However, the visualization method is useful only for flow regimes with well-defined visual boundaries, such as the intermittent and annular regime flow.

A study by Doretto et al. (2013) investigated visualization and heat transfer of three different condensing refrigerants (R-236ea, R-134a, and R-410A) in a 8.0 mm diameter tube ($85 < G < 902$ kg m⁻² s⁻¹, $0.01 < x < 0.78$). The study found mixed agreement comparing their data to both classic and contemporary flow mapping from a variety of sources (Breber, Palen, and Taborek 1980; Taitel and Dukler 1976; Tandon, Varma, and Gupta 1982; El Hajal, Thome, and Cavallini 2003; Alberto Cavallini et al. 2002), and concluded that while the subject matter has been extensively studied over the last century, there remains a scattering of the data. It was found however that for the size of tube studied, the non-dimensionalized coordinate systems (X_{it} , j_v , etc.) developed for similar sized tubes (Breber, Palen, and Taborek 1980; Tandon, Varma, and Gupta 1982) well predicted the flow regimes observed.

The studies above show that while objective flow regime determination is likely possible, especially in the case of annular and intermittent flows, additional research must be performed to qualify the methods employed, and make them useful to a wider range of flow regimes and system geometries. Additionally, further investigation is required into the applicability of the available classic and contemporary maps when applied to the lower mass fluxes and micro-scale geometry investigated in this body of research.

2.2.2 AVAILABLE FLOW REGIME MAPS AND TRANSITION CRITERIA

One of the objectives of the present study is to evaluate the predictive capability of existing flow regime maps and transition criteria for refrigerants in small channels at low mass fluxes. Some of the more popular flow regime models are presented below. The specific details of each flow map and equations for subdivision of flow regimes will be discussed further as they are compared to the available data in Chapter 4.

As one of the first studies to develop flow maps specifically based on flow physics and dimensionless parameters, the research presented by Taitel & Dukler (1976) is still commonly used today as the basis for many contemporary flow maps. The work looked specifically at the fundamental physics involved in flow regime stability, and proposed conditions for which each regime might remain stable or transition. As mentioned previously, the model neglects the effects of fluid surface tension, not originally pertinent for the sizes of tubes studied, but proposes a set of transitions based on dimensionless parameters F , T , K , and X - the Martinelli parameter (elaborated upon further in Section 4.3.2.1). The values of the various parameters were plotted against X to describe the transitions in flow regimes, as shown in Figure 2.2. The regimes identified were annular-dispersed, stratified-wavy, stratified-smooth, dispersed bubble, and intermittent.

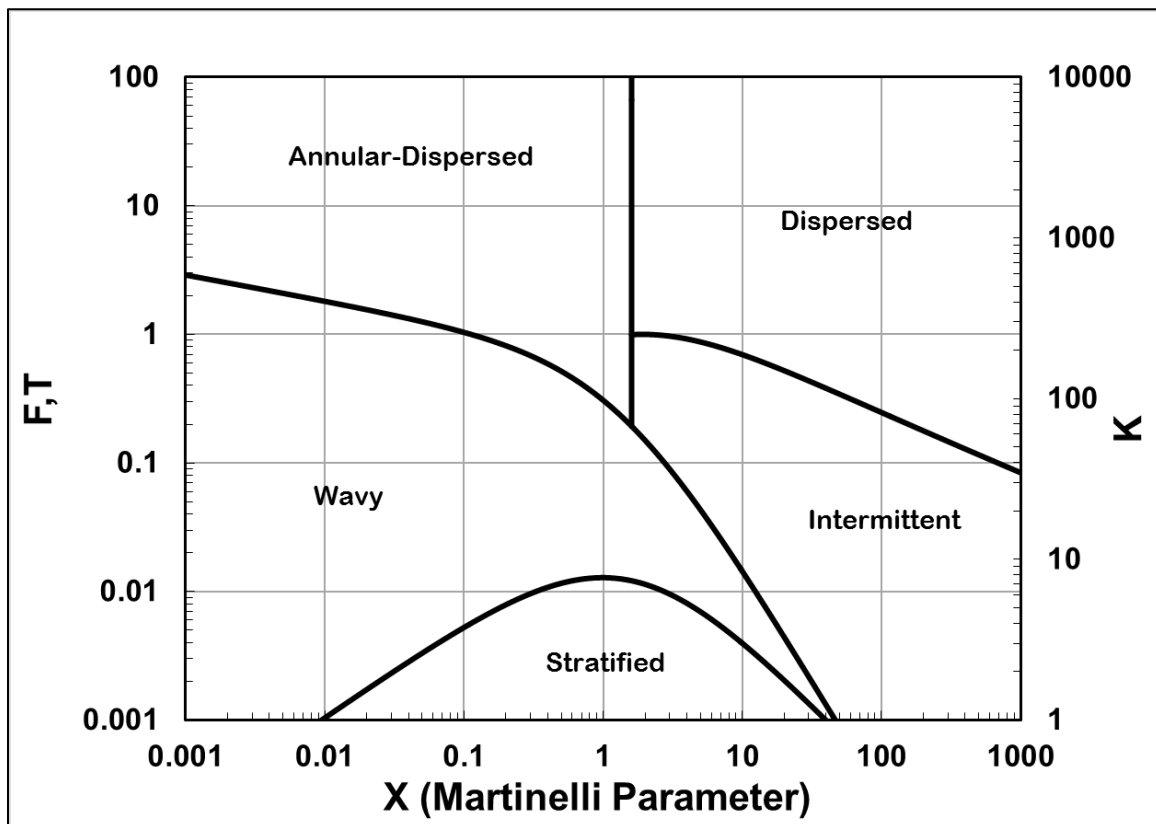


Figure 2.2 - Flow regime map proposed by Taitel & Dukler (1976)

Cavallini et al. (2002) developed a flow map based on a database of flow visualization and heat transfer data of condensing refrigerants. They concluded that there exists a dimensionless vapor velocity (j_v^*), defined below in Equation (2.1), above which all flow will be annular and below which transition to either stratified, intermittent, or stratified annular will be determined by a constant turbulent-turbulent Martinelli parameter (X_{tt}). The flow map developed in their study was combined with a heat transfer model to predict

local condensation heat transfer coefficient. It was tuned using over 600 data points and compared with a 10.4% mean absolute deviation to a total of 1,778 data points from a variety of sources. The model is estimated to be accurate for tubes with diameters from 3.0 to 21.0 mm, reduced pressures less than 0.75, and liquid/vapor density ratios over 4. The research presented in Cavallini et al. (2006) expands on the flow transition model for use in a heat transfer analysis, dividing flow regimes into only ΔT -dependent (e.g. stratified/wavy) and ΔT -independent (e.g. annular) flows.

$$j_v^* = \frac{Gx}{(gD_h\rho_v[\rho_l - \rho_v])^{0.5}} \quad (2.1)$$

Drawing on a flow boiling two-phase transition map originally proposed by Kattan et al. (1998), a study presented by El Hajal et al. (2003) proposed a new flow map for condensation in horizontal tubes. The work sought to develop a model based on the fluid void fraction, as applied to the condensation database developed in Cavallini et al. (2001). A database of 425 data points comprising six different refrigerants and a variety of test conditions ($D = 8$ mm, $0.12 < x < 0.88$, $65 < G < 750$ kg m⁻² s⁻¹) was statistically fit to the flow transition model proposed in earlier works for boiling flows. For an estimation of void fraction, the author draws upon both the homogeneous model for high reduced pressures, shown in Equation (2.2), and the drift flux void fraction model, shown below in Equation (2.3) and developed by (Steiner 1993) for low to medium reduced pressures.

$$\varepsilon_h = \left[1 + \left(\frac{1-x}{x} \right) \left(\frac{\rho_v}{\rho_l} \right) \right]^{-1} \quad (2.2)$$

$$\varepsilon_{ra} = \frac{x}{\rho_v} \left(\left[1 + 0.12(1-x) \right] \left[\frac{x}{\rho_v} + \frac{1-x}{\rho_v} \right] + \frac{1.18(1-x) \left[g\sigma(\rho_l - \rho_v) \right]^{0.25}}{G\rho_l^{0.5}} \right)^{-1} \quad (2.3)$$

The two equations were then combined using a log-mean average across the reduced pressure to estimate a void fraction and occupied area (A) applicable to a full range of reduced pressures, shown in Equation (2.4)

$$\varepsilon_{LM} = \frac{\varepsilon_h - \varepsilon_{ra}}{\ln\left(\frac{\varepsilon_h}{\varepsilon_{ra}}\right)}; A_l = A(1 - \varepsilon_{LM}); A_v = A\varepsilon_{LM} \quad (2.4)$$

The flow regime model developed by El Hajal et al. (2003) uses the above void fraction model to develop transitions between stratified, wavy, intermittent, annular, mist, and dispersed flow (originally presented as *fully-stratified, stratified-wavy, intermittent, annular, mist, and bubbly*).

The map developed was shown to compare well to other similar maps that were also in development, with both qualitative and quantitative comparison. The proposed flow map was also shown in Part II of the study (Thome, El Hajal, and Cavallini 2003), which made use of the map to predict condensation heat transfer, to be able to well predict the heat transfer in data produced by nine independent laboratories. It is reported to be accurate within a wide range of conditions ($3.14 < D_h < 21.4$ mm, $16 < G < 1532$ kg m⁻² s⁻¹, $0.02 < Pr < 0.8$, $76 < (We/Fr)_l < 884$).

Kim & Mudawar (Kim and Mudawar 2013; Kim and Mudawar 2012) proposed a flow regime transition model between annular and intermittent flows in small channels based on a database of 4,045 data points spanning 28 different sources. The database was used to evaluate heat transfer models developed for both micro and macro channels, and found that only two of those developed for macrochannels (Akers and Rosson 1960; Moser, Webb, and Na 1998) came close to accurately predicting the data collected, with mean absolute error (MAE) values of 27.3% and 27.7% respectively. The new model proposed by Kim & Mudawar (2013) was able to predict the collected data within an MAE of 16.0%.

The proposed model, presented in Kim & Mudawar (2013), made use of transition criteria based on the Weber and modified Martinelli parameter. The flow regimes were fit to specific heat transfer characteristics used to predict heat transfer in that regime. The method developed was based on a wide variety of flow conditions ($0.42 < D_h < 6.22$ mm, $53 < G < 1403$ kg m⁻² s⁻¹, $0 < x < 1$), but was not compared to any data points outside of those used to develop the method.

Nema et al. (2014) developed new dimensionless transition criteria using parameters similar to those developed by Taitel & Dukler (1976), who drew primarily from physical characteristics of flow. However, the study also drew from an extensive R-134a database ($1 < D_h < 4.91$ mm, $150 < G < 750$ kg m⁻² s⁻¹) and transition criteria originally proposed by Coleman & Garimella (2003) to develop the proposed transition criteria.

The flow map proposed by Nema et. al. (2014), makes use of the Martinelli parameter, Bond number, Weber number, and dimensionless variable T proposed by Taitel & Dukler (1976) to predict flow regimes in micro and macro channels. The map makes use of the critical Bond number to determine a transition criteria from large to small tubes, where surface effects begin to play a role in the observed flow regimes. The prediction of the model scales with the flow geometry to include the relative effects of shear and body

forces on the flow. The microscale regimes predicted below the critical Bond number are dispersed, annular, intermittent, and mist (originally presented as *dispersed*, *annular-film*, *intermittent annular film*, and *mist*).

2.3 GOALS OF CURRENT RESEARCH

While the literature has been saturated with the study of heat transfer and pressure drop in condensing flows in recent years, studies continue to underrepresent microscale flows at low vapor qualities and mass fluxes, as shown in Figure 2.3 below. While the channel geometry of interest continues to grow smaller and smaller, research is struggling to maintain applicability within the expanding microchannel regime. Many studies show the highest deviation from modeled flow at lower vapor qualities, which gain importance when designing for efficient fully condensing systems. As the manufacturability of microchannel structures increases, so does the need for research investigating the related flow structures.

The majority of work thus far has focused on the transition from annular to stratified or intermittent flow at relatively high mass fluxes. These studies have captured some of the most prevalent effects in heat transfer and condensation, but have neglected to capture regimes in low mass flux applications. The present study seeks to understand the applicability of current tools and methods for predicting two-phase flow regimes of low surface tension refrigerants in small channels and at low mass fluxes.

2.3.1 AVAILABLE RESEARCH

In the pursuit of supporting engineering development of low mass flux microchannel systems, research must first strike a path by supplying data and models to describe the operational environment. To identify microchannel fluid flow visualization currently studied, the literature review above has been condensed into a table demonstrating the design landscape currently supported by available studies. Table 2.2 below summarizes all studies focused on flow visualization presented above.

Table 2.2 - Review of available flow visualization literature

Source	Study Type	Fluid	D _h Studied [mm]		G Studied [kg m ⁻² s ⁻¹]		Geometry
Weisman et al. (1979)	Refrigerant	Freon 113	12	50	--	--	Round
Dobson & Chato (1998)	Refrigerant	R12, R22, R134a, R32/R125	3.14	7.04	75	800	Round
Coleman & Garimella (2000)	Refrigerant	R134a	1.0	4.0	150	750	Round, Rectangular
Coleman & Garimella (2003)	Refrigerant	R134a	2.6	4.91	150	750	Round, Square, Rectangular
Jassim et al. (2006)	Refrigerant	R134a, R410A	1.7	8.0	100	600	Round
Keinath (2012)	Refrigerant	R404a	0.51	3.1	200	800	Round
El Achkar et al. (2013)	Refrigerant	n-pentane	0.55	0.55	3	15	Square
Doretti et al. (2013)	Refrigerant	R236ea, R134a, R410A	7.69	7.69	85	902	Round, Microfinned
Milkie et al. (2016)	Refrigerant	R134a	1	1.6	300	800	Rectangular
Suo & Griffith (1964)	Gas-Liquid	Heptane, H ₂ O, Octane, N ₂ , H ₂	0.05	0.08	--	--	Round
Barnea et al. (1983)	Gas-Liquid	Air/Water	4.0	12	--	--	Round
Damianides & Westwater (1988)	Gas-Liquid	Air/Water	1.0	5.0	--	--	Round, Microfinned
Mishima & Hibiki (1995)	Gas-Liquid	Air/Water	1.0	4.0	--	--	Round
Coleman & Garimella (1999)	Gas-Liquid	Air/Water	1.0	5.0	--	--	Round, Rectangular
Triplett & Ghiaasiaan (1999)	Gas-Liquid	Air/Water	1.09	1.49	--	--	Round, triangular
Kawahara et al. (2002)	Gas-Liquid	H ₂ O/N ₂	0.1	0.1	--	--	Round
Kawahara et al. (2002)	Gas-Liquid	Air/Water	1.0	1.0	--	--	Round
Waelchli & Rudolf von Rohr (2006)	Gas-Liquid	Water, Ethanol, Glycerin, N ₂	0.15	0.4	--	--	Rectangular
Barreto et al. (2015)	Gas-Liquid	Air/Water	1.2	1.2	50	300	Round
Kingston et al. (2015)	Gas-Liquid	Air/Water	0.3	0.3	--	--	Square
Yang & Shieh (2001)	Both	Air/Water, R134a	1.0	3.0	300	1600	Round

For reference, the above table has been collected into a graph of the currently available flow visualization landscape, showing those areas supported by multiple studies and models, and those unsupported by the current literature, below in Figure 2.3. The graph shows only studies reporting both parameters included in the graph – several studies from Table 2.2 are not shown.

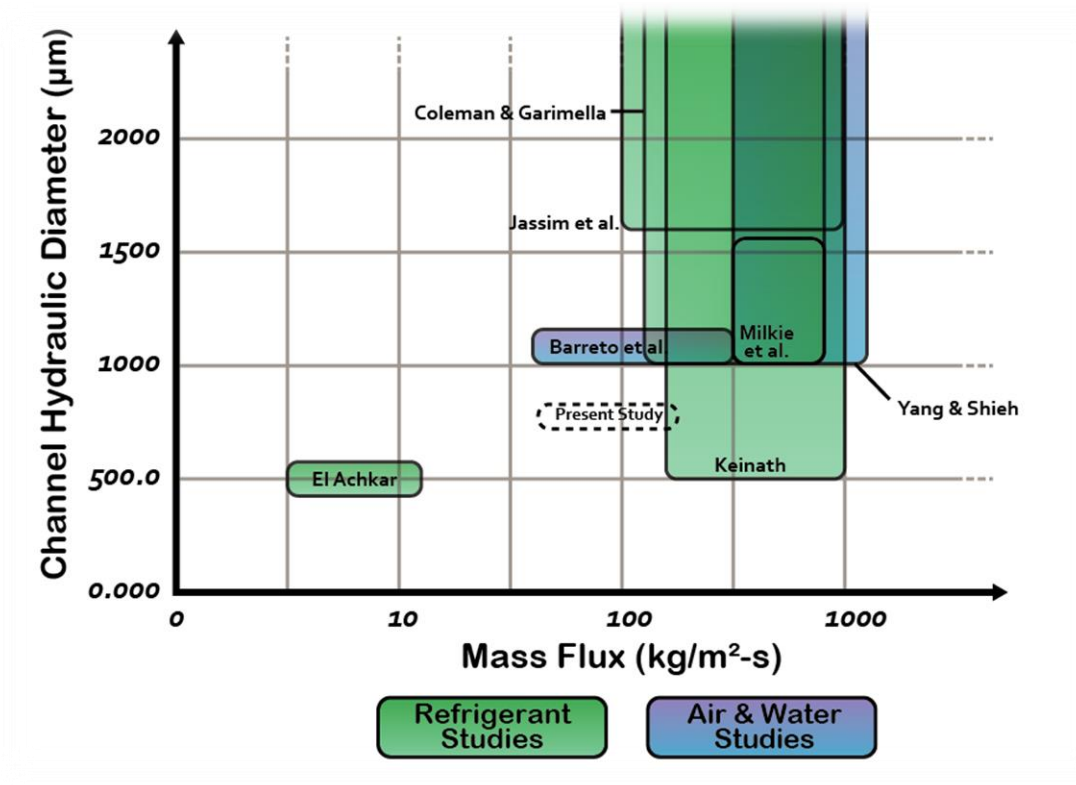


Figure 2.3 - Map of currently available microscale flow visualization studies

Looking into the areas that are still under-represented in flow regime research, it can be seen from Figure 2.3 above that microscale flow below $G = 100 \text{ kg m}^{-2} \text{ s}^{-1}$ remains relatively unsupported. The low mass-flux microchannel visualization data targeted by the present study is highlighted.

2.3.2 RESEARCH OBJECTIVES

While it has been shown that some microscale multi-phase research has been performed in the recent years, focusing on flow regime mapping for the purposes of pressure drop and heat transfer, it can also be seen that there are clear knowledge gaps in the available literature for low mass flux conditions in the microscale. It has also been shown that there exists a practical need for research in this area for the purpose of developing efficiently engineered and robust systems to operate in that design space. It is therefore the goal of this study to provide flow visualization data to support the investigation of low mass flux flow regime studies, as well as an evaluation of the above maps and models commonly used to predict flow regimes in that design space.

The specific goals of this study are outlined below:

- Develop a microscale system capable of visualizing adiabatic multi-phase flow at a variety of saturation temperatures, quality, and mass fluxes
- Compare the results found to regime predictions from the available flow maps and models, and evaluate the validity of those models at the given conditions
- Suggest targeted areas of further study to advance the design space of microscale multi-phase flow.

3 EXPERIMENTAL DESIGN & INSTRUMENTATION

To achieve the stated research goals, a flow system was required capable of producing and measuring low mass flux, two-phase flows of low surface tension fluids at varying thermodynamic quality with a maximum pressure of 2070 kPa (300 psia). The designed system consists of a test section (Section 3.1), working fluid loop (Section 3.2), cooling fluid loop (Section 3.3) and the requisite instrumentation (Section 3.4). A schematic of the complete facility is shown in Figure 3.1 and a photograph of the uninsulated system in Figure 3.2. Each of the constituent subsystems are discussed in detail below.

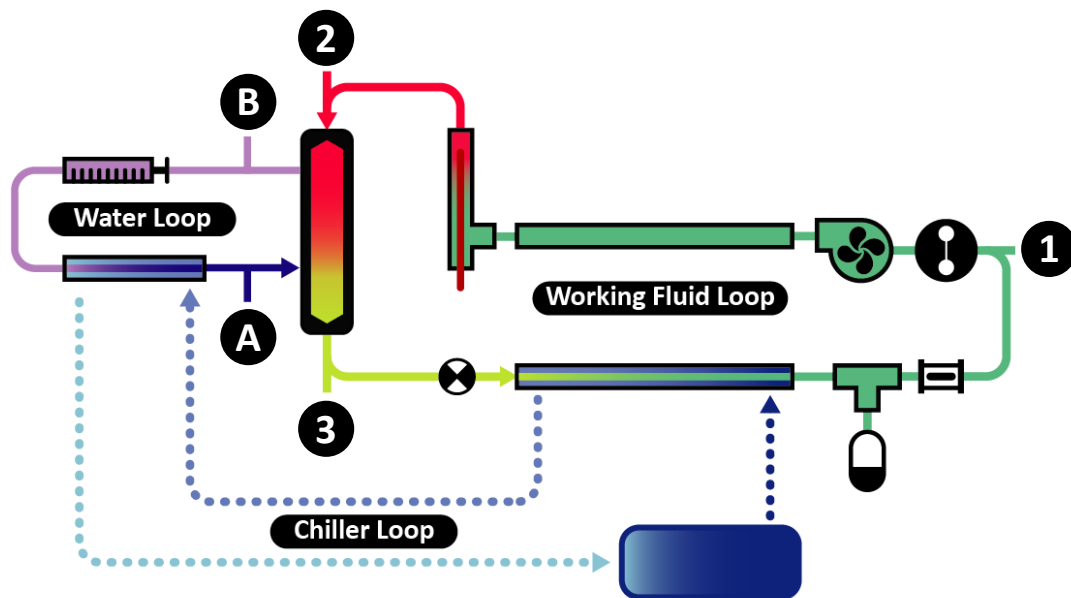


Figure 3.1 - Schematic of experimental system with important state points labeled

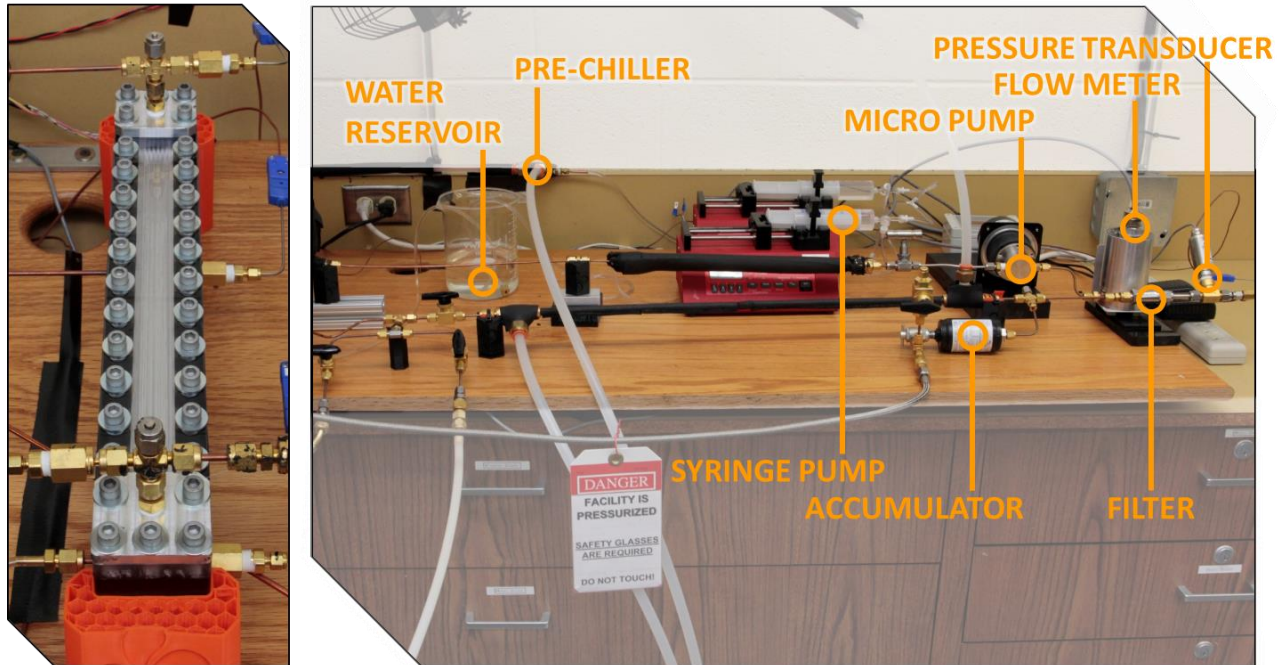


Figure 3.2 - Fully assembled flow loop as run for experimental data (test section photographed before being insulated). Test section pictured to the left, downstream components pictured at right.

3.1 TEST SECTION DESIGN

The purpose of the test section (conceptual design shown in Figure 3.3) was to condense superheated vapor to a specified thermodynamic quality, and then allow optical access to the flow of saturated liquid and vapor mixture. Calculations were performed for an array of multiple channels to ensure that the total mass flow rate and condensation heat duty was large enough to measure with acceptable accuracy (and are detailed below). To mitigate the risk of maldistribution, fluid enters the test section as superheated vapor, is distributed to the multiple parallel channels, and then condensed to the desired quality in the pre-condensing length of the flow channels. Unlike many other multi-phase visualization studies (Niño, Hrnjak, and Newell 2003; Kawahara, Chung, and Kawaji 2002; Coleman and Garimella 1999) where flow enters the test section as a two-phase mixture, superheating the inlet fluid enables a more uniform distribution.

By knowing the inlet pressure, temperature, and mass flow rate of both the working and cooling fluids, as well as the change in temperature on the cooling side, the outlet flow quality can be calculated through an energy balance. Precisely knowing the microchannel dimensions also allows for the calculation of the flow mass flux. The test section for this experiment is designed to allow for these measurements with reasonable certainty. Figure 3.3 shows the test section design concept used in the present investigation.

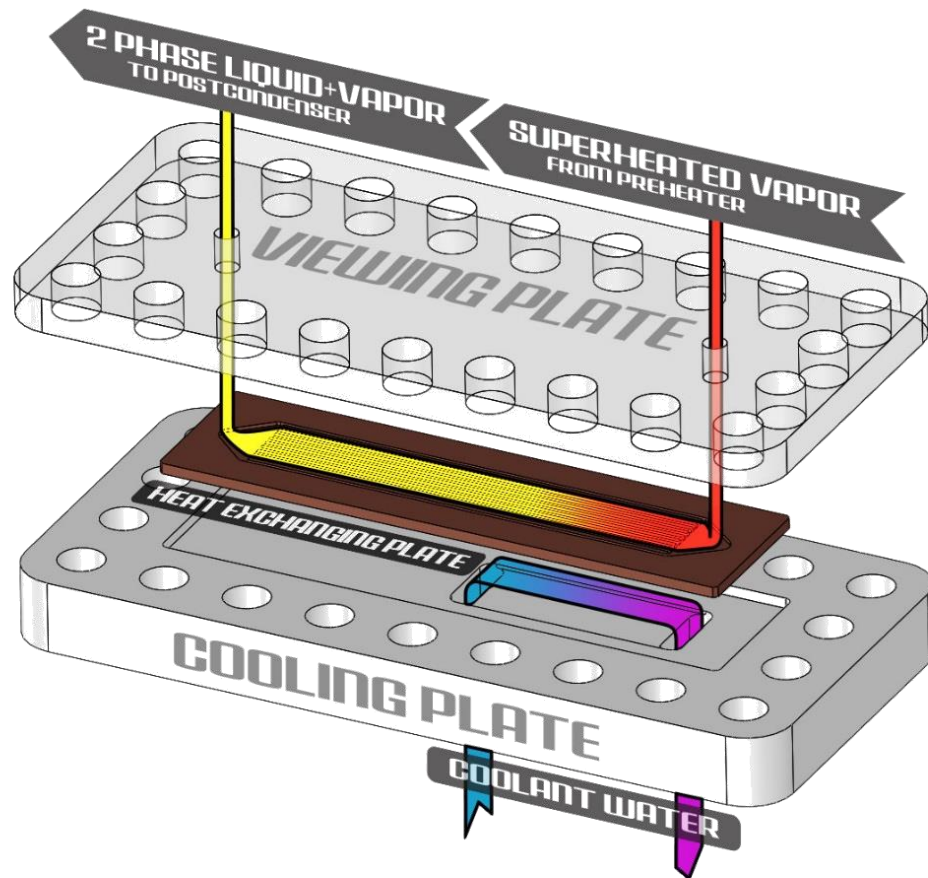


Figure 3.3 - Test section concept design

3.1.1 DESIGN METHODOLOGY

In designing the test section for the visualization study, the driving goal was to produce a test vessel capable of providing an adiabatic visualization of partially condensed flow while maintaining reasonable levels of uncertainty (less than $\pm 15\%$) in the final calculated quality and mass flux. Because this test section was to be the first developed in a series of low mass-flux studies, permanently bonded joints were avoided in favor of bolted or threaded connections. This design allows new channel geometries to be easily swapped in and out.

As shown above in Figure 3.3, the test section design involves a counterflow heat exchanger to condense superheated fluid into a saturated mixture of liquid and vapor. Because the outlet of the test section is a saturated mixture, the quality in the visualization length must be estimated using an energy balance on the cooling fluid side. With quality as a function of the water-side temperature difference, it was determined via preliminary uncertainty analysis that the water-side temperature difference must be maintained above

10°C to achieve reasonable levels of uncertainty. Full details of the data analysis and uncertainty calculations in the actual experiments are presented in Section 4.2.

To design for flows in the microscale regime, where flow dynamics are strongly dependent on surface tension forces opposed to body forces, the channel dimensions were sized according to the expected Bond number. As mentioned in the review of literature previously, studies by Sou & Griffith (1964), Bretherton (1961), and Brauner & Maron (1992) suggest surface tension forces dominate the flow dynamics for Bond numbers less than 0.84. In flows of refrigerant R-134a ($T_{\text{sat}} = 50^{\circ}\text{C}$), A Bond number of 0.84 relates to a channel hydraulic diameter of 0.71 mm.

A square microchannel cross section ($\alpha = 1$) was selected to allow comparison with prior studies performed at higher mass fluxes. A hydraulic diameter of under 1.0 mm was desired to maintain a Bond number near the microscale transition predicted by the literature. Because the test section was to be machined by CNC to maintain precision, a nominal channel width of 0.794 mm was selected, which can be more easily produced using a 1/32 inch end mill making a single pass.

One of the primary challenges of the present study was to accurately measure and control very low fluid flow rates corresponding to relatively low mass fluxes in the microchannels. It was found that to operate within the capabilities of readily available commercial pumping systems, the volumetric flow rate should be at least 10 mL min⁻¹. The minimum number of channels required in the test section was then estimated via Equation (3.1), varying the desired mass flux, expected density of the subcooled liquid, and the hydraulic diameter. This analysis revealed that the test section should have at least five channels to achieve the low mass fluxes desired in the experiment.

$$\dot{V} = \frac{G(NWH)}{\rho_l} \quad (3.1)$$

Because flow enters the pre-condensing length of the test section as superheated vapor, it must be condensed to the desired quality before entering the viewing length. A counter flow of cooling water was used to achieve the desired flow quality entering the viewing section. The cooling fluid channel spans the entire width of the flow channels, and runs along the base of the pre-condensing length, as show above in Figure 3.3.

The pre-condenser heat exchanger was sized using the UA-LMTD method to determine the minimum length required to condense a flow to a desired quality over the range of expected experimental conditions. The uncertainty in the calculated quality for each of the calculated lengths was estimated and a final design

length of pre-condenser was selected that allowed for the widest range of data to be obtained with reasonable uncertainty. To guide the discussion of the pre-condenser design methodology, results from a representative case of $G = 15 \text{ kg m}^{-2} \text{ s}^{-1}$, $T_{\text{sat}} = 55^\circ\text{C}$, 5°C of superheat and a desired quality of 0.5 are presented below in Table 3.1.

Table 3.1 - Representative numbers used in calculations below for $G = 15 \text{ kg m}^{-2} \text{ s}^{-1}$ and $x = 0.5$

Variable		Value	Unit
Area Required	A_{req}	5.20E-04	m ²
Avg. Working Fluid Quality	x	7.50E-01	--
Conductivity, Wall	K_{wall}	1.67E+02	W m ⁻¹ K ⁻¹
Conductivity, Working Fluid	K_{wf}	6.76E-02	W m ⁻¹ K ⁻¹
Heat Transfer Rate	\dot{Q}	3.74E+00	W
Heat Transfer Units	UA	2.38E-01	W K ⁻¹
Hydraulic Diameter	D_h	7.94E-04	m
Length Required	L	1.31E-01	m
Log-mean Temperature Diff.	--	1.57E+01	K
Mass Flow Cooling Fluid	\dot{m}_{cf}	1.41E-05	kg s ⁻¹
Mass Flow Working Fluid	\dot{m}_{wf}	4.73E-05	kg s ⁻¹
Number of Channels	N	5.00E+00	--
Nusselt Cooling Fluid	Nu	5.33E+00	--
Nusselt Working Fluid	Nu	6.06E+00	--
Overall Heat Transfer Coeff.	U	4.58E+02	W m ⁻² K ⁻¹
Prandtl Number, Liquid	Pr	3.15E+00	--
Pressure, Crit. Working Fluid	P_{crit}	4.06E+03	kPa
Pressure, Sat. Working Fluid	P_{sat}	1.49E+03	kPa
Reynolds Number, Liquid	Re_L	8.99E+01	--
Sp. Enthalpy, Cooling Fluid	h_{cf}	3.45E+03	W m ⁻² K ⁻¹
Sp. Enthalpy, Working Fluid	h_{wf}	5.16E+02	W m ⁻² K ⁻¹
Sp. Heat, Cooling Fluid	cp	4.18E+03	J kg ⁻¹ K ⁻¹
Temp. Inlet Cooling Fluid	$T_{i,cf}$	1.00E+01	°C
Temp. Inlet Working Fluid	$T_{i,wf}$	6.00E+01	°C
Temp. Outlet Cooling Fluid	$T_{o,cf}$	7.36E+01	°C
Temp. Outlet Working Fluid	$T_{o,wf}$	5.50E+01	°C
Wall Thickness	t	1.00E-03	m

In determining heat exchanger length via the UA-LMTD method, the convective and conductive thermal resistances were determined to solve for the overall heat transfer coefficient, U . Equation (3.2) below shows the relationship between the combined heat transfer coefficient, the heat transfer rate, and heat exchanger area. The log-mean-temperature difference for a counterflow heat exchanger can be determined as a function of inlet and outlet temperatures, as shown in Equation (3.3). The overall heat transfer coefficient

was found using Equation (3.4). Equation (3.5) relates the known mass flow rate of working fluid to the heat transfer rate and cooling fluid mass flow rate.

$$A_{required} = \frac{\dot{Q}}{U \times LMTD \times N} \quad (3.2)$$

$$LMTD = \frac{(T_{i,f} - T_{o,w}) - (T_{o,f} - T_{i,w})}{\ln\left(\frac{T_{i,f} - T_{o,w}}{T_{o,f} - T_{i,w}}\right)} \quad (3.3)$$

$$\frac{1}{U} = \frac{1}{h_f} + \frac{t}{k_{wall}} + \frac{1}{h_w} \quad (3.4)$$

$$\dot{Q} = \dot{m}_f (h_{i,f} - h_{o,f}) = \dot{m}_w C_{p,w} (T_{o,w} - T_{i,w}) \quad (3.5)$$

The convective heat transfer coefficient of the cooling fluid (h_{cf}) was determined assuming laminar, fully developed flow (Reynolds number varied from 5 to 65 for the range of flow possible) in a rectangular duct with $\alpha = 4.0$ ($Nu = 3.66$). The Nusselt number for a condensing flow is less simple to determine, and is still the target of multiphase flow studies. However, for a rough estimation of the expected Nusselt number, the Shah (1979) correlation was used, given the liquid only Reynolds number, liquid Prandtl number, and average quality, as shown in Equation (3.6). While the Shah correlation is limited to vapor velocities and Reynolds numbers far above those expected, it was used to provide a first estimate of the condensing heat transfer coefficient. In fact, the cooling fluid thermal resistance dominated the transport, so accurate prediction of the condensing coefficient was less important in estimating the test section size.

$$Nu_{cond} = \frac{D_h \bar{h}_f}{k_f} = 0.023 Re_{lo}^{0.8} Pr_l^{0.4} \left[(1 - \bar{x})^{0.8} + \frac{3.8 \bar{x}^{0.76} (1 - \bar{x})^{0.04}}{(P_{sat} / P_{crit})^{0.38}} \right] \quad (3.6)$$

The conductivity of the test section material is known through material selection. To limit machining time and the amount of time required for the experiment to reach steady state, Aluminum 6061 was selected as the microchannel test section material. Aluminum has high thermal conductivity ($k_{wall} = 167 \text{ W m}^{-1} \text{ K}^{-1}$), is far easier to machine than copper or steel, and is commonly used in microchannel heat exchanger applications.

With knowledge of the log mean temperature difference, heat transfer rate, and combined heat transfer coefficient, the required heat exchanger area was calculated via Equation (3.7). With the cross-sectional dimensions already determined by design, the required area was then related to a required length. By

varying inlet temperatures and flow rates, the minimum required length of pre-condenser that would satisfy the collection of all desired data points was determined. After the minimum length was determined, the same process was used with a known length to then determine the required mass flow rate and temperature rise of cooling water that would be used to collect each data point. The final design pre-condenser length was 200 mm.

$$A_{required} = \frac{UA_{required}}{U} \quad (3.7)$$

With the length of pre-condenser determined, an adiabatic length of test section was added to serve as the viewing section. A length of 90 mm was added to the test section to allow for a substantial length-to-width ratio in the visually observable channel flow. Headers were included at the beginning and end of the flow channels to allow fluid an inlet and outlet location on the plate. The final design of the heat exchanger plate can be seen below in Figure 3.4.



Figure 3.4 - Heat exchanging plate and flow channels

Because of the pressure differential between the pressurized working fluid and roughly atmospheric pressure cooling fluid beneath the heat exchange plate, channel deflection was a concern. Simple beam bending calculations were performed to estimate the channel deflection in widthwise and lengthwise orientation. Equation (3.8) for a beam fixed at both ends with uniform loading describes the expected maximum deflection for the given pressure differential (Engineers Edge 2016). For the materials and geometries studied, the estimated deflections were on the order of 0.5% of the channel height, and were considered to be negligible.

$$\delta_{max} = \frac{WL^3}{384EI} \quad (3.8)$$

As shown in Figure 3.3 above, a base and viewing section were needed to contain the aluminum plate and flow channels. An impact resistant polycarbonate was selected for the viewing section material to allow for ease of machining but maintain non-energetic failure in the event of over pressurization. The material was also reported to be compatible with R-134a (DuPont 2016) for the range of temperatures expected. With a reported thermal conductivity of $0.19 \text{ W m}^{-1} \text{ K}^{-1}$, the 9.5 mm thick polycarbonate sheet has orders of magnitude more thermal resistance than the 1.0 mm thick aluminum heat exchanging plate, mitigating the

risk of substantial heat loss from the test section. For similar reasons, Delrin® (Polyoxymethylene) was selected for the base plate material, which houses the cooling fluid channel and supports the heat exchange plate. A neoprene O-ring cord was used to seal the heat exchange plate against the base plate to contain the cooling fluid.

Lastly, in order to incorporate NPT ports for the inlet and outlet of the working fluid, a 12.7 mm (0.5 inch) thick plate was added at either end of the test section to integrate the flow inlet and exit NPT fittings. A 0.5 inch diameter O-ring was used to seal the face of the NPT blocks to the viewing section. The blocks were machined from aluminum for ease of tapping the NPT ports and maintaining a face seal near the O-ring.

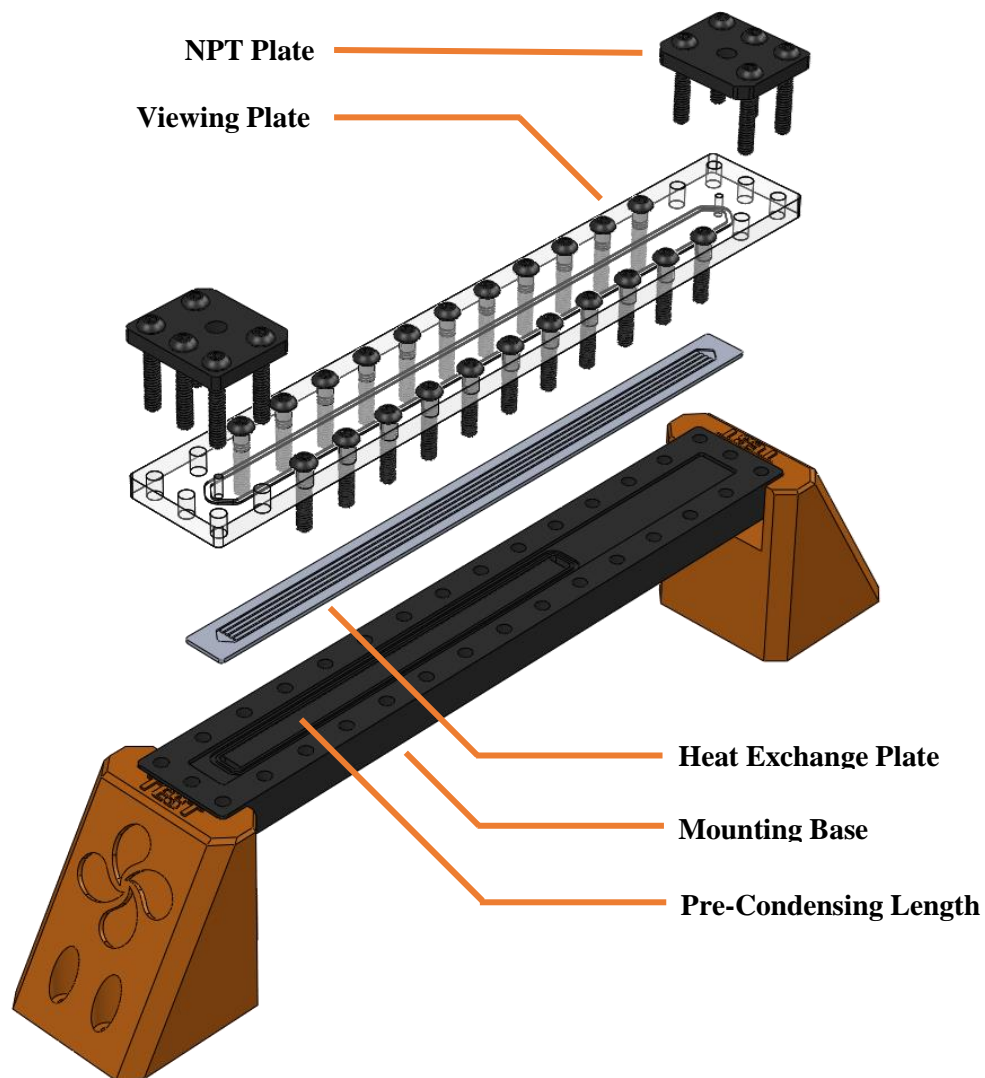


Figure 3.5 - Model of the experimental test section

The final design for the test section can be seen above in Figure 3.5. Detailed final design dimensions of the test section are provided in Table 3.2

Table 3.2 - Relevant nominal test section dimensions

Dimension	Value	Unit
NPT Port Size	0.125	in
Viewing Plate Thickness	9.5	mm
O-Ring Thickness	0.063	in
Heat Exchange Thickness	1.000	mm
Nominal Channel Width	0.794	mm
Nominal Channel Depth	0.794	mm
Channel Spacing	1.830	mm
Pre-Conditioning Length	200.0	mm
Viewing Length	90.00	mm
Cooling Channel Width	11.300	mm

3.1.2 IMPLEMENTATION

All components of the test section were fabricated using CNC milling to maintain the precise tolerances required in the channel dimensions. Models were produced for the parts and assembly using SOLIDWORKS (2014). A Numeric Control (NC) code was written in EdgeCAM (2014) to produce each component, and stock was purchased from McMaster-Carr. A full list of the stock used in machining the various test section components is included below in Table 3.3 for reference.

Table 3.3 - Stock used in machining the test section

Stock Description	Used for	Part Number
Impact-Resistant Polycarbonate, 3/8" Thick, 3" Wide	Viewing Plate	1749K539
Round-Profile Neoprene O-Ring Cord Stock, 1/16 Width	O-Ring	1430K51
Black Delrin® Acetal Resin Rectangular Bar, 2 ft. Length	Base	8662K64
Multipurpose 6061 Aluminum, Sheet, .080" Thick, 2" x 24"	Test Section	89015K191
Foam Rubber Insulation, 1/8" Thick, 2" Wide	Insulation	5541K11

All components were machined on a Fadal VMC15 vertical milling center in the OSU Product Realization and Manufacturing Lab. The as-machined dimensions of the channels in the heat exchange plate were verified after machining using a ZeScope™ optical profiler, provided by the Microproducts Breakthrough Institute (MBI). The ZeScope™ measures surfaces using vertical scanning interference microscopy, which enables it to resolve three-dimensional features as small as 2 μm. The width and depth of each channel was measured using this technique, ensuring that the features were all machined as intended. The as machined dimensions of each channel are included below in Table 3.4.

Table 3.4 - As-machined dimensions of microchannel heat exchanger

Channel	Depth [μm]	Width [μm]	Area [m^2]	D_h [μm]	Aspect Ratio	
Left	1	897.93	809.89	7.3E-07	851.64	0.902
	2	844.45	810.39	6.8E-07	827.07	0.960
	3	866.76	810.87	7.0E-07	837.88	0.936
	4	880.94	810.76	7.1E-07	844.39	0.920
Right	5	898.51	809.05	7.3E-07	851.44	0.900

The average measured channel hydraulic diameter was $842.49 \mu\text{m}$, with a standard deviation of 1.1%. Figure 3.6 below shows a sample measurement taken by the ZeScope™, showing a measurement of channel depth in channel 2.

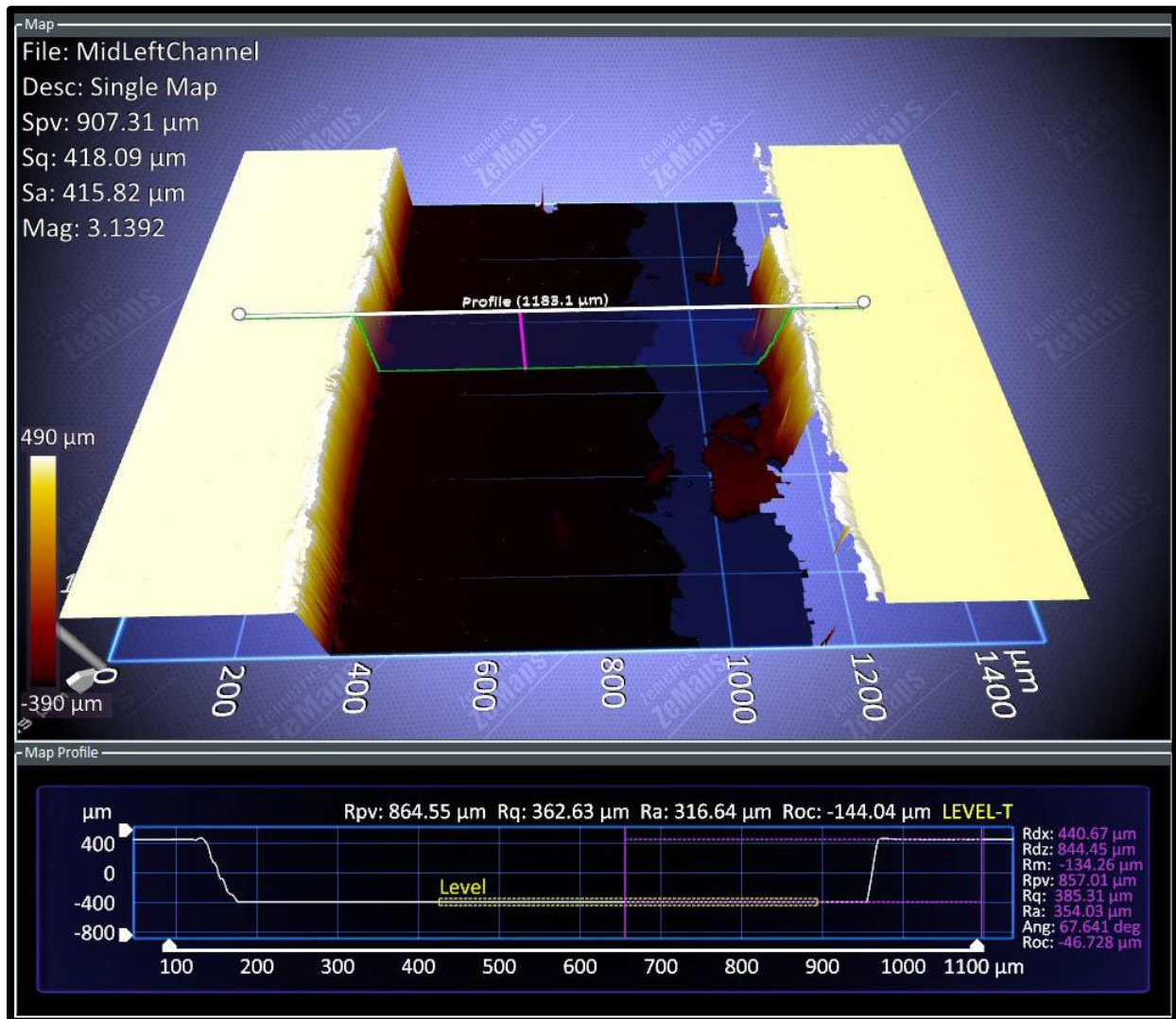


Figure 3.6 - Sample channel depth measurement (axes not displayed to scale)

After verification, the test section components were assembled and bolted together using 1/4 - 20 1.5 inch socket headed cap screws. Care was taken in assembly to ensure that all bolts received equal torque and that all O-rings were properly sealed. The system was insulated wherever optical access to the flow was not required, and testing was performed to ensure a minimal amount of heat loss during flow. A full description of the heat-loss testing is included in Chapter 4.

3.2 WORKING FLUID LOOP

The refrigerant loop was designed as a closed system operating at approximately constant pressure. This configuration allowed for extended continuous operation while achieving steady-state conditions. Operating saturation temperatures of 40°C and 55°C were selected to compare the effects of varying saturation temperature on the observed flow regimes. The final design for the working fluid loop is shown below in Figure 3.7.

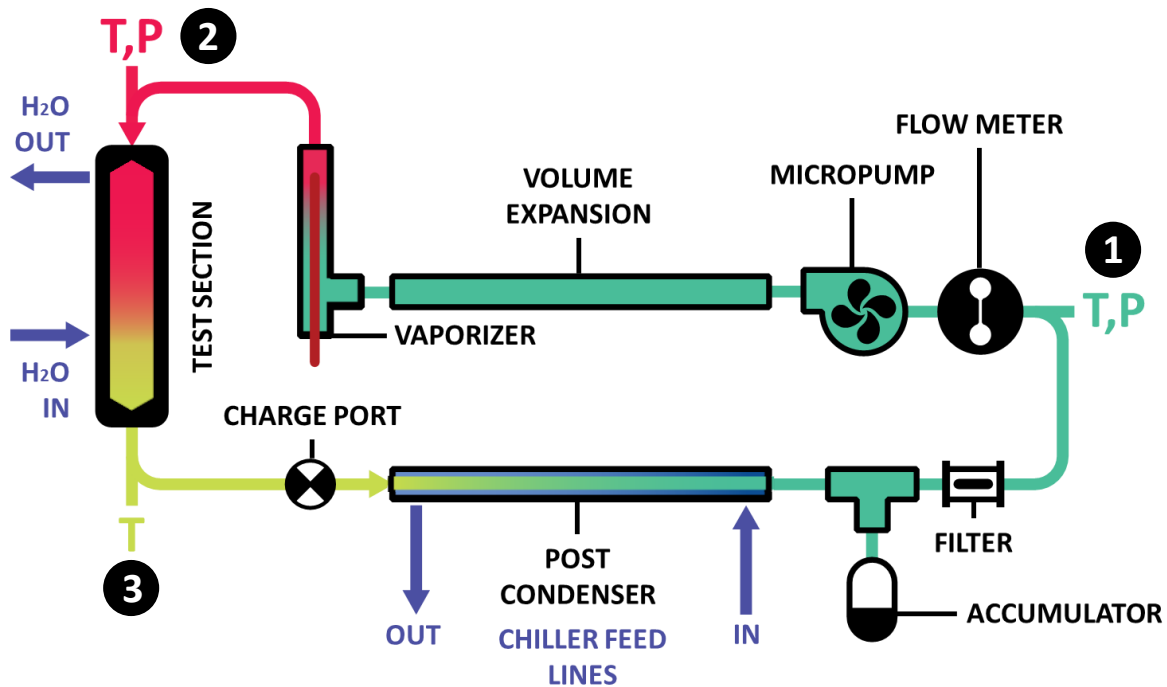


Figure 3.7 - Schematic of working fluid loop with labeled state points

The multiphase visualization apparatus developed in this study was the first flow loop to be fabricated by members of the TEST Lab group. A high level of modularity was desired to allow various configurations of the system to be easily investigated by future students. All connections required to hold pressure are either NPT, compression, or AN fittings, which can all be pressure fit and then disassembled many times with ease. As the saturation pressure of R-134a at 55°C is 1490 kPa (216 psia), all working fluid loop

components were required to have a maximum operating pressure of at least 2070 kPa (300 psia). System tubing was either 0.125, 0.25, 0.375, or 0.5 inch copper tubing, with burst pressures exceeding 10,000 kPa (1450 psia). Depending on the connection type, fittings were either brass or stainless steel, with a minimum burst pressure of 5,500 kPa (800 psia).

Copper tubing was used to join several different components arranged in series (Figure 8). The majority of these components were sized using an EES code that estimated the amount of energy required to move from one state point to another. With estimates on the required energy transfer, components such as condensers or heaters were designed and sized. The sizing of components used is described below by state point. All flow components used to develop the refrigerant loop are summarized below in Table 3.5.

At state point one, the temperature and pressure of the fluid are known, and can be used to determine the fluid density entering the flowmeter. To achieve mass fluxes in the range of $100 \text{ kg m}^{-2} \text{ s}^{-1}$ through the five channels of the test section, the required flow rate of liquid R-134a at the pump and flowmeter is roughly 14 mL min^{-1} . This can be determined by Equation (3.9) below, which relates the fluid density, volumetric flow rate, and cross-sectional flow area to a mass flux of saturated liquid and vapor mixture in the test section.

$$\dot{V} = \frac{\dot{m}_l}{\rho_l} = \frac{GA_x}{\bar{\rho}_{sat}} \quad (3.9)$$

A positive displacement gear pump system manufactured by Micropump was purchased to pump fluid through the system. The pump head is designed such that no lubricating grease or oil comes into contact with any internal flow components, which are driven via magnet. Because of the replaceable gearing in the system, a wide range of low mass flow rates are achievable, even with such low viscosity fluid. The pump operates by continuously drawing fluid into the pump head using a set of graphite gears and a pressure foot. The charge then exits the head via the outlet due to the pressure differential as more fluid is drawn in behind it. The micro gear pump can theoretically pump flows from $8\text{-}500 \text{ mL min}^{-1}$ at operating pressures of up to 34,000 kPa (5,000 psia). The max pressure differential (pump head) is 100 kPa (15 psid). The pump is driven via magnetic coupling by a brushless 20-30 V motor that is controlled by a 0-5 V signal. Both the supply and signal voltages are provided by a variable voltage supply unit capable of 0.01 V variations.

From the pump, fluid enters an expansion of system volume. The volume expansion was added to the system to dampen out any fluctuations associated with a very small system volume. Fluid then enters the vaporizer. An energy balance, similar to that used in Equation (3.5), was performed to size the heating element for the vaporizer. At a flow rate corresponding to a test section mass flux of $150 \text{ kg m}^{-2} \text{ s}^{-1}$ (maximum expected) the energy required to superheat the 10°C refrigerant by 5°C is almost 80 W. Thus,

a 250 W cartridge heater was specified to supply the heat load required to vaporize the flow. The heater, which was 0.25 inches in diameter, was ordered with a male NPT fitting welded to the base and one inch of unheated length. The “no-heat” length on the heater allowed it to integrate into the vaporizer tubing via the NPT fitting without significantly heating the surrounding fittings during operation, as shown below in Figure 3.8.

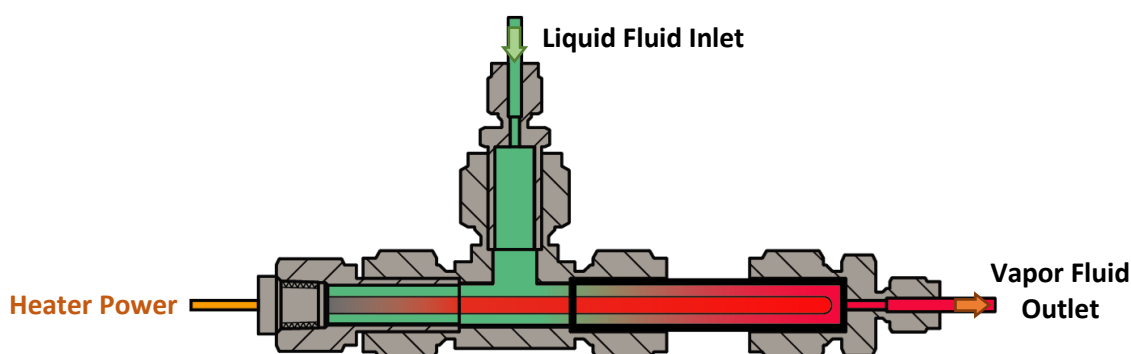


Figure 3.8 - Diagram of vaporizer operation

Originally, the heater was controlled using a Watlow PID control unit. The controller monitored the flow temperature and sought to match a set system temperature by opening or closing a solid state relay. It was found through visual inspection of the flow in the test section that this method of control contributed to flow instabilities as the heater was cycled on and off. To avoid this, the heater was instead powered using a Variac variable voltage controller. A K-type thermocouple was included in the heater tip because overheating of the heating element was a concern. The thermocouple was able to provide a measurement of the heater internal temperature during operation. It was found through testing that the required heat loading to vaporize the necessary flows did not trip a 250°C alarm wired into the controller. The maximum operating temperature of the heater was specified as 760°C. Operation without the monitoring alarm was deemed acceptable.

After being partially condensed in the test section, the two-phase mixture exited at state point three and was then fully condensed in the post-condenser to state point one. The post-condensing section of the loop consisted of a counterflow tube-in-tube heat exchanger assembled from copper tube and compression fittings as shown in Figure 3.9.

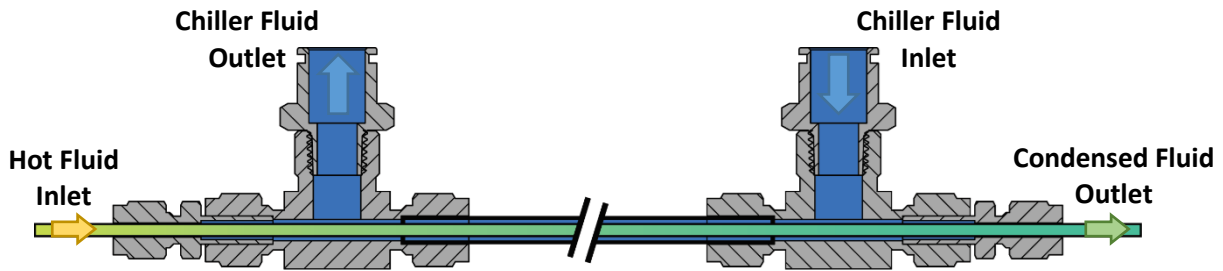


Figure 3.9 - Tube-in-tube heat exchanger used for the post-condenser

The length of post condenser required to fully condense the flow was calculated similarly to the heat exchanging plate in the test section. The required surface area was established using the UA-LMTD method.

A piston accumulator was included in the system to keep the charge at the desired saturation pressure, and is oriented downwards to collect liquid instead of vapor in the accumulation section during charging. The accumulator volume is 20 mL, and uses a piston-actuated volume to compress fluid to the desired system pressure. A tank of nitrogen and 600 psi regulator were used to provide accumulator back pressure. In sizing the accumulator, a volume was selected that was larger than the approximate volume difference between liquid and vapor during phase transition in the test section. Sizing the accumulator accordingly allows the system to run continuously through a range of flow qualities without changing the mass of charge in the system.

Lastly, a 15 micron sintered-metal inline filter was included in the loop to filter any particulates out of the flow before entering the flowmeter and pump. The filter pore size was selected based on recommendations in the pump and flowmeter manuals. The smallest available filter size recommended was selected for use in the system. Table 3.5 below summarizes the various components used in assembling the loop and the associated part numbers and manufacturers.

Table 3.5 - Elements used in fluid loop assembly

Element	Manufacturer	Part/Model Number
Nutating Flowmeter	DEA Engineering	FMTD4
Gear Pump	Micropump	L22653
Pump Motor	Micropump	DB380A
Heating Element	Watlow	E5A-12716
Accumulator	Motion and Flow Control Products Inc.	ACP04AA002R1KTB
Filter	Swagelok	SS-4F-15

3.3 COOLING FLUID LOOP

There were two cooling fluids used in this experiment; deionized water to be used for pre-condensing flow in the test section, and a mixture of equal parts ethylene-glycol and water used for bulk heat removal. The deionized water was used in the test section because precise knowledge of the fluid specific heat capacity was required for use in Equation (3.5). For all other heat removal applications, a chiller was used to supply a flow of chilled ethylene-glycol and water mixture (equal parts by volume) at 5°C. A schematic of the cooling fluid loop is shown below in Figure 3.10. The design and operation of this system is discussed below, with Table 3.6 below detailing the components used.

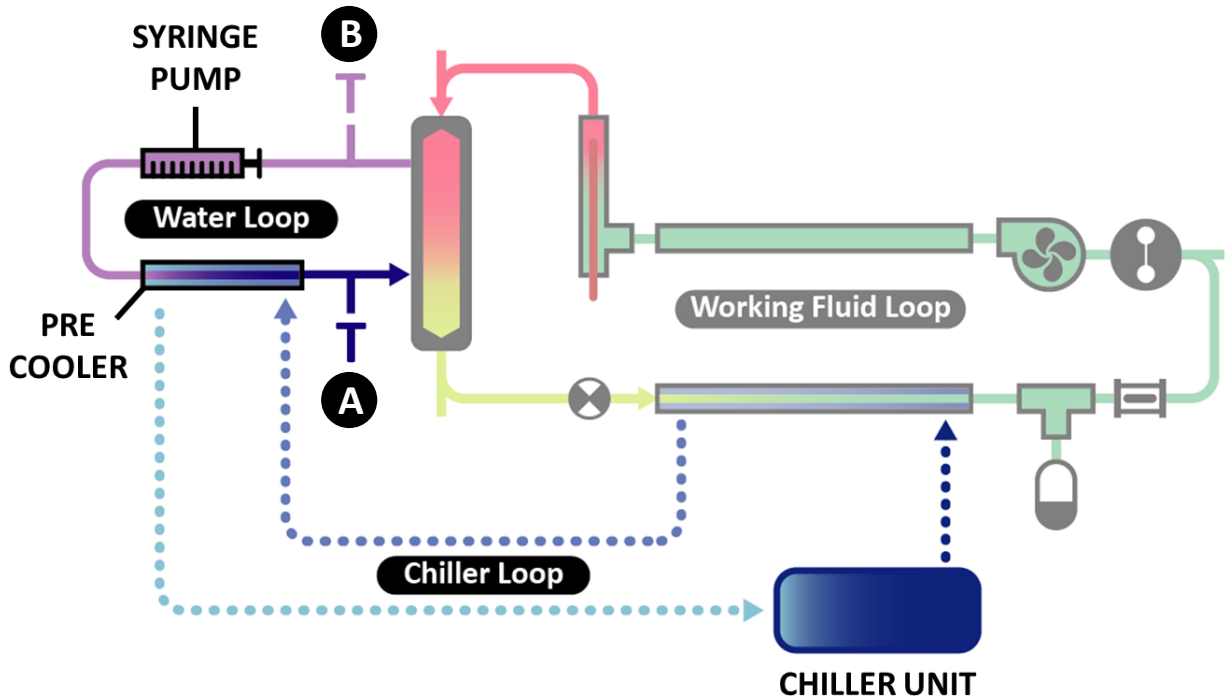


Figure 3.10 - Cooling fluid loop configuration. Water shown as a solid line, ethylene-glycol as a dashed line. State points are shown as circumscribed letters

The various cooling systems were designed as closed systems to allow for continuous operation during long periods of testing. Preliminary cooling systems used for shake-down testing required refilling of liquid or ice in order to operate and demanded constant observation to achieve steady state conditions. The cooling loop designs for both fluids are described below.

The two important variables as identified by the energy balance in Equation (3.5) are the mass flow rate and temperature difference from state points A to B. Because the thermocouples used to measure the flow temperature are accurate to within 0.5°C, a large temperature difference is required on the water-side to keep uncertainty low in the energy balance. To maintain high water-side temperature difference a combination of low water flow rate and low inlet temperature was required. The inlet temperatures and mass flow rates were varied parametrically in the EES model and it was found that flows as low as 0.1 mL min⁻¹ could be required to capture the desired data. Additionally, for flow in such conditions, inlet temperatures as low as 10°C would be required.

To provide the desired flow rates, a set of NE-1010 New Era Pump Systems syringe pumps were purchased. The two syringe pumps are able to communicate with each other and can operate in continuous flow mode with one pump filling as the other discharges. The two 50 mL syringes were connected to a water reservoir by a set of one way valves, and then fed into the water-side pre-chiller.

The flow of cooling water was then pre-chilled in a tube-in-tube heat exchanger similar to that shown in Figure 3.9. A Thermo NESLAB M75 chiller was used to supply a parallel flow of ethylene-glycol and water mixture to cool the inlet flow of deionized water. The water then flowed into the test section, cooled the flow of working fluid, and exited to return to the reservoir. The same chiller fluid was also routed to the working fluid post-condenser in a counterflow orientation as shown in Figure 3.9.

A cooling fluid trim heater was included on the water side, and was designed and constructed similarly to the vaporizing section shown in Figure 3.8. The trim heater was used to heat the flow when performing heat-loss studies, and was not used during regular operation. The various elements used in the cooling fluid operations are shown below in Table 3.6.

Table 3.6 - Elements used in cooling-fluid loop assembly

Element	Manufacturer	Part/Model Number
Chiller	Thermo NESLAB	M75
Syringe Pumps	New Era Pumping Systems	DUAL-NE-1010-US
Dual Pump Plumbing	New Era Pumping Systems	P-DKIT

3.4 INSTRUMENTATION

The system was fully instrumented to determine a variety of state points as fluid moved throughout the system. System state points are shown above in Figure 3.1 and were instrumented to provide knowledge of the temperature, pressure, and flow rate of fluid at that point. With system state points determined, the energy loss (and therefore flow quality) can be determined in the viewing section. Additionally, the viewing section was instrumented to allow for flow visualization. The measurement systems used for recording the necessary data for these measurements are discussed below.

3.4.1 TEMPERATURE

Where temperature measurements were necessary, thermocouples were inserted parallel to the flow via compression fittings as shown in Figure 3.11 to. The thermocouple tip was placed as close as possible to the desired measurement location without obstructing flow, and the fitting was fully insulated.

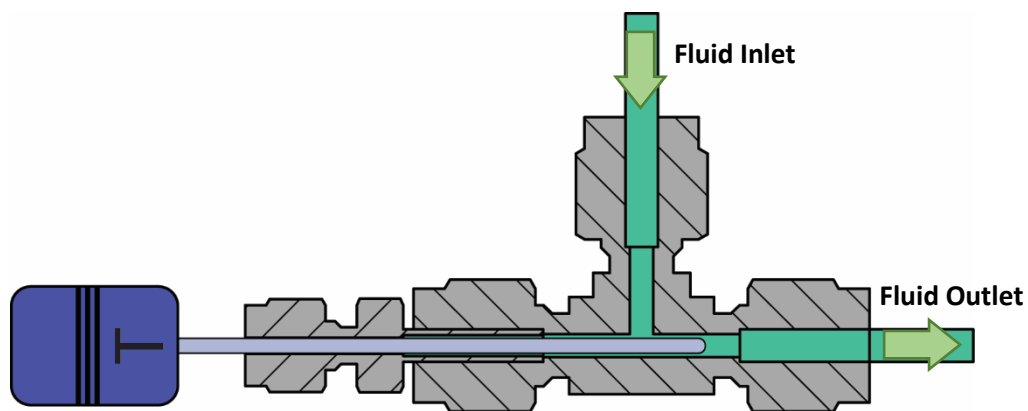


Figure 3.11 - Thermocouple incorporated into compression fitting for measuring flow temperature

The thermocouples were calibrated in a heated drywell and ice bath against a high accuracy Fluke platinum resistance thermistor. The calibration thermistor was read by a Fluke 1502A thermometer readout, while the thermocouples were read to 0.05°C display accuracy using an NI thermocouple reader. The precision in temperature measurement of the Fluke calibration device was reported as ± 0.1 mK, and the thermocouples were read to a display accuracy of $\pm 0.025^\circ\text{C}$. Because the Fluke drywell was not able to maintain temperatures below 50°C , only three relevant temperatures were able to be used in the calibration. Due to the limited number of calibration points, the experimental uncertainty of $\pm 0.5^\circ\text{C}$ was used for the temperature readings, which was the accuracy reported by the manufacturer. The calibration points for the thermocouples are included in Table 3.7 for reference.

Table 3.7 - Thermocouple calibration results

Thermocouples		RTD and TC Readings at Various Set Points in °C					
Number	TC Location	RTD 50	TC 50	RTD 60	TC 60	RTD Ice	TC Ice
1	Water Inlet	50.206	50.2	60.209	60.1	0.256	0.3
2	Water Outlet	50.196	50.0	60.216	60.1	0.294	0.5
3	Fluid Inlet	50.211	50.3	60.205	60.2	0.282	0.5
4	Fluid Outlet	50.208	50.3	60.192	60.1	0.281	0.4
5	Fluid Pump	50.164	49.9	60.192	60.0	0.280	0.3

3.4.2 PRESSURE

For pressure measurements, a pair of Omega PX209-300A1 pressure transducers were used at the pump and test section inlet (state points one and two). The transducers used have a measurable range of 0-2070 kPa (0-300 psia) and output in the form of a 4-20 mA current signal, which is less susceptible to noise than a voltage-based signal. The data from the current signal is read as voltage drop across a 250 Ohm resistor during data acquisition. The acquisition of data and uncertainty in measurement will be discussed further in Section 4.2

3.4.3 FLOW RATE

Because R-134a is a low viscosity, low surface-tension fluid it is challenging to pump and meter at low flow rates. To measure flow rates in the 7-18 mL min⁻¹ range, a nutating flowmeter was purchased from DEA Engineering. The flowmeter operates as shown below in Figure 3.12, with a dual chamber system that allows liquid to pass through only by displacing the nutating metering element. The nutating flowmeter is capable of measuring low-viscosity flows from 1-250 mL min⁻¹ and has a rated max operating pressure of 20.7 MPa (3,000 psia).

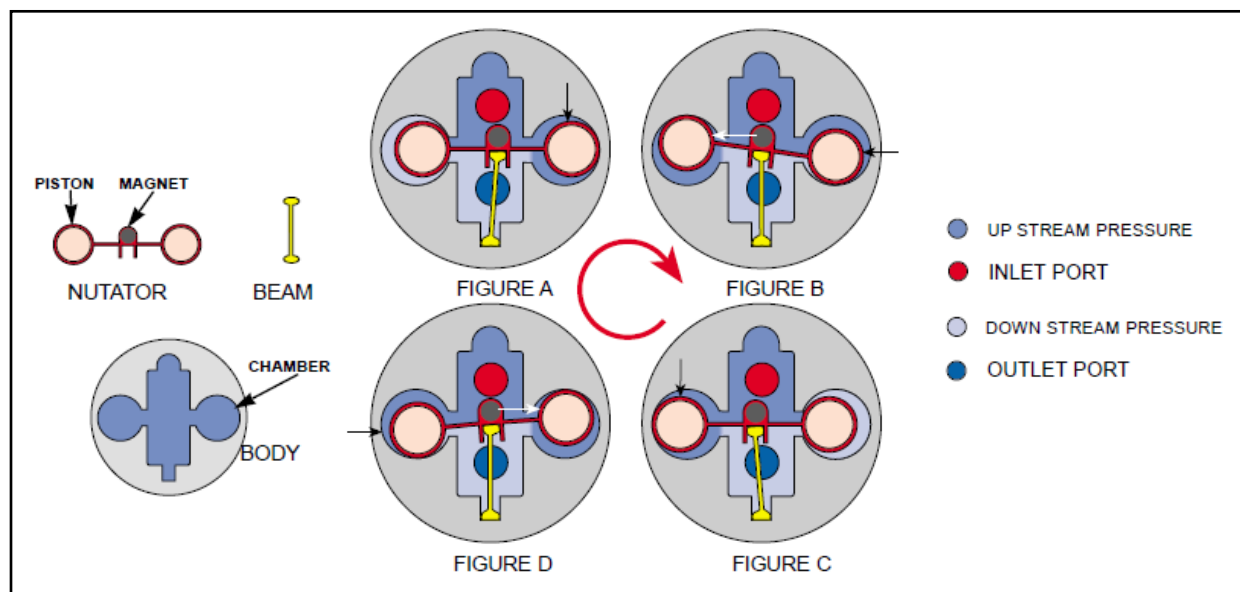


Figure 3.12 - Operation of DEA Nutating flowmeter (DEA 2016)

The flowmeter signal output is in the form of a 0-5 V square wave, which is triggered twice every cycle of the nutating flowmeter element. The square wave is read by a Cortex XEF-12 data logger, which then outputs a visual reading of the flow and a 4-20 mA signal based on the upper and lower bounds of the flowmeter (0-250 mL min⁻¹). To convert the square frequency signal to a volumetric flow rate, the data logger uses the k-factor provided by the flowmeter manufacturer, which is reported to within 1% of the flowmeter reading. The k-factor reported by the Bell Flow Systems calibration report is 46.22 pulses per cubic centimeter.

3.4.4 VISUALIZATION

A Phantom V310 high speed camera was used to capture optical images of the flow. Because frames were captured at 2400 fps with a $415.96 \mu\text{s}$ exposure time, a large amount of system light was required. Two 500 W Lowell OMNI™ lights were used to bathe the test section channels in light from angles high and to the right, and low and to the left as shown in Figure 3.13 below. A 500 W Halogen light was also used to the right of the system to eliminate shadows in the channels. In order to diffuse light into the test section from additional angles, a white sheet of diffusion paper was used behind the camera lens to reflect additional light into the test section viewing port. A 60mm Nikon AF Micro Nikkor™ lens was used to capture a 1280 x 800 pixel resolution image of the viewing section.



Figure 3.13 - Visualization set up used for data capture during experiment

4 DATA COLLECTION AND ANALYSIS

This chapter details the processes of data collection and analysis employed in the present study. The chapter first details the data collected through the experimentation portion of the study (Section 4.1), and then reviews the uncertainty analysis performed to validate the data (Section 4.2). Section 4.3 is an analysis of the data, and investigates the significance of the data collected.

4.1 DATA COLLECTION

Data was collected both in the form of high speed fluid flow visualization, as well as thermodynamic data used to describe the mass flux, saturation pressure, and thermodynamic quality of the data. The collection, post processing, and review of the data collected in this study is presented below.

4.1.1 DATA COLLECTION PROCESS

The data of interest in the present study were high-speed videos of two-phase flow of R-134a at different mass flux and thermodynamic quality. Temperature, pressure, and fluid flow rate measurements were collected using a LabVIEW (National Instruments 2016) program developed to receive information from the DAQ system. Data was collected a rate of 4 Hz. These measurements were used to make live estimations of the test section quality and mass flux at any given data point. To develop this tool, a LabVIEW Virtual Instrument (VI) was created capable of interacting with the NIST REFPROP (NIST 2013) library. The tool used measured sensor readings to determine and return thermodynamic properties of the R-134a to the VI. While use of this tool allowed for live verification that fluid at the pump was fully liquid, and that fluid in the test section was a two-phase mixture at the desired saturation temperature, these parameters were verified in post-processing, as discussed below.

High-speed video was obtained with a Phantom v310 high speed camera, described in a previous chapter. Operation of the high-speed visualization system was performed manually, using a switch on the power distributor for the lighting and a collection on/off button for the camera. The Phantom PCC software provided with the Phantom camera was used to collect the visualization footage. Because the collective 1500W of lighting power was focused on the test section, the lights were powered only for a brief moment when capturing video to prevent excessive heat gain in the test section. A test case was run and found that for long duration exposure ($t > 10$ s), a noticeable fluid temperature climb occurs with full light impingement on the test section. Additional short duration tests confirmed that there was no noticeable effect on the data while lighting the test section for less than 5 seconds.

To capture each data point, the refrigerant and cooling water pump flow rates were adjusted until the desired state point was approximately reached. After steady state occurred, when fluctuations in data were such that the uncertainty due to variation was acceptable, the data point was captured. Due to the reciprocating nature of the water-side coolant pumps, a truly steady state could not be reached as the temperature would spike occasionally when the pumps transitioned from infusion to refilling. A steady state condition was defined as condition in which the mean reading between temperature spikes varied no more than the known sensor noise, which was verified visually on a graph of live readings. This approach allows for the introduction of uncertainty, as it leaves room for human error in the determination of steady state. During post processing, the data was checked to ensure that the readings were stable during capture and well within the expected levels of variation uncertainty. In future studies, a digitally determined running average will be employed to determine steady state, comparing the local average over the past seconds to the running average over the past five minutes within a determined tolerance range.

During the process of data capture, the LabVIEW VI was first set to begin data collection. Then, the lighting was turned on, a set of high-speed images were captured by the camera, and then the lighting was turned off (in the timespan of approximately 2 seconds). Data collection was then turned off, on average about 9 seconds after having begun. The data collected during this time was averaged to produce a single data point and standard deviation over the duration of the visible frames captured. The actual timespan accounted for in each full video (approximately 3 GB of data) was roughly 0.4 seconds.

To post-process the data, data captured during operation was averaged and the average values and associated uncertainties (discussed further in Section 4.2) were analyzed using *Engineering Equation Solver* (EES) (F-Chart Software 2016) to determine the nominal quality and mass flux of the data point, as well as the statistical variation. Additionally, the EES code made use of a polynomial estimation of system heat loss (developed in Section 4.2.4 below) to account for energy leaving the system not captured by the data. Images and video of each data point were exported from the .cine raw files into more manageable video and image files for comparison. The data collected in this study is summarized below.

4.1.2 DATA PROCESSING

After collection, the data was time averaged and post processed using EES to determine the nominal quality and mass flux of the dataset. The calculations performed to determine quality and mass flux from measurements of temperature, pressure, and flow rate are outlined below. A model data point will be used as an example in this outline to demonstrate the process ($T_{\text{sat}} = 55^{\circ}\text{C}$, $G = 104.8 \text{ kg m}^{-2} \text{ s}^{-1}$, $x = 0.17$).

Using the measurements of pressure and temperature at the system pump and pre-condenser entry, state points could be established to evaluate fluid density and enthalpy. Similarly, knowing fluid temperature for

the coolant water inlet and outlet with an assumed pressure of atmospheric, the fluid density could be evaluated as a function of temperature. With the fluid properties known at the various points of interest, the mass flux is calculated using the measured volumetric flowrate at the pump, and the known fluid density per Equation (4.1). For the data point in question, these values are shown below in Table 4.1, calculated from the measured values. Then enthalpy of vapor entering the test section is determined as a function of inlet temperature and pressure.

$$\dot{m} = \dot{V}_l \rho_l \quad (4.1)$$

Table 4.1 - Measured and calculated values at fluid pump and test section inlet

State Point	T [°C]	P [psi]	ρ [kg/m ³]	\dot{V} [m ³ /s]	\dot{m} [kg/s]	h [J/kg]
At pump	12.35	220.6	1074	2.9E-07	3.7E-04	--
At inlet	62.24	220.6	77.83	--	3.7E-04	285,469

The mass flux through the test section, which has a constant cross-sectional flow area, can then be calculated via Equation (4.2) below, where A represents the total cross-sectional flow area of all five channels. Following the example data point, which was solved to have a mass flow rate of 0.000372 kg s⁻¹, the mass flux can be shown to be 104.8 kg m⁻² s⁻¹ through each of the test section channels.

$$G = \dot{m}/A \quad (4.2)$$

To calculate the thermodynamic quality of the flow, which cannot be calculated simply using a measured temperature and pressure, the amount of energy removed from the flow during pre-condensing had to be calculated. To calculate the amount of energy *leaving* the working fluid, a sum was made of the energy *gain* by the cooling water, as well as the estimates of energy lost to the surroundings by both the working fluid and the cooling water. The energy balance is shown below in Equation (4.3), with heat loss to the surroundings (Q_{hx}) modeled as heat flow from the fluids. The method for estimating the heat loss from the system is elaborated on further in Section 4.2.4. The control volume is summarized by Figure 4.1.

$$\dot{m}_f (h_{f,out} - h_{f,in}) = \dot{m}_w C_{p,w} (T_{w,in} - T_{w,out}) - Q_{hx,w,out} - Q_{hx,f,out} \quad (4.3)$$

The flowrate and temperature gain of the working fluid is used as the primary measure of heat removed from the system. As shown in Equation (4.3), the energy transferred to the cooling fluid is a function of mass flowrate, specific heat, and temperature change. For the sample data point, the energy gain is calculated as shown below. The heat loss or gain from the surroundings is determined using the method developed in Section 4.2.4, below.

$$\dot{m}_w C_{p,w} (T_{w,in} - T_{w,out}) = \left(0.00024 \frac{\text{kg}}{\text{s}} \right) \left(4183 \frac{\text{J}}{\text{kg} \cdot \text{C}} \right) (10.8^\circ \text{C} - 55.7^\circ \text{C}) = -45\text{W}$$

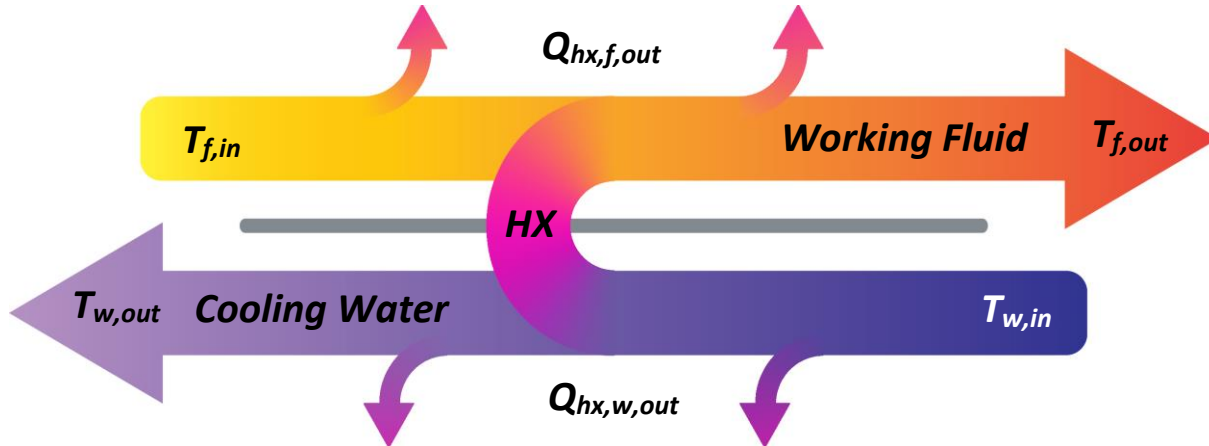


Figure 4.1 - Control volume analyzed for heat transfer.

Solving for the enthalpy exiting the pre-condenser, and assuming an adiabatic test section, the thermodynamic quality can be calculated by evaluating the state point using enthalpy and exit temperature (which is at the saturation temperature). The equation below shows the final determination of exit enthalpy, which can be combined with the saturation temperature to solve the function for thermodynamic quality.

$$\left(0.00037 \frac{\text{kg}}{\text{s}} \right) \left(h_{f,out} - 285,469 \frac{\text{J}}{\text{kg}} \right) = -45\text{W} + 0.91\text{W} + 3.68\text{W}$$

$$h_{f,out} = 164,132 \quad x_{out} = f(h_{f,out}, T_{sat}) = 0.17$$

4.1.3 DATA COLLECTED

During data collection, 23 data points (12 $T_{\text{sat}} = 55^\circ \text{C}$, 10 $T_{\text{sat}} = 40^\circ \text{C}$) were obtained to compare the effects of mass flux, quality, and saturation temperature on the observed flow regime. A summary of the data points collected are shown in Figure 4.2 and Table 4.2. A full table of all relevant measured and calculated values for each data point is available in the Appendix.

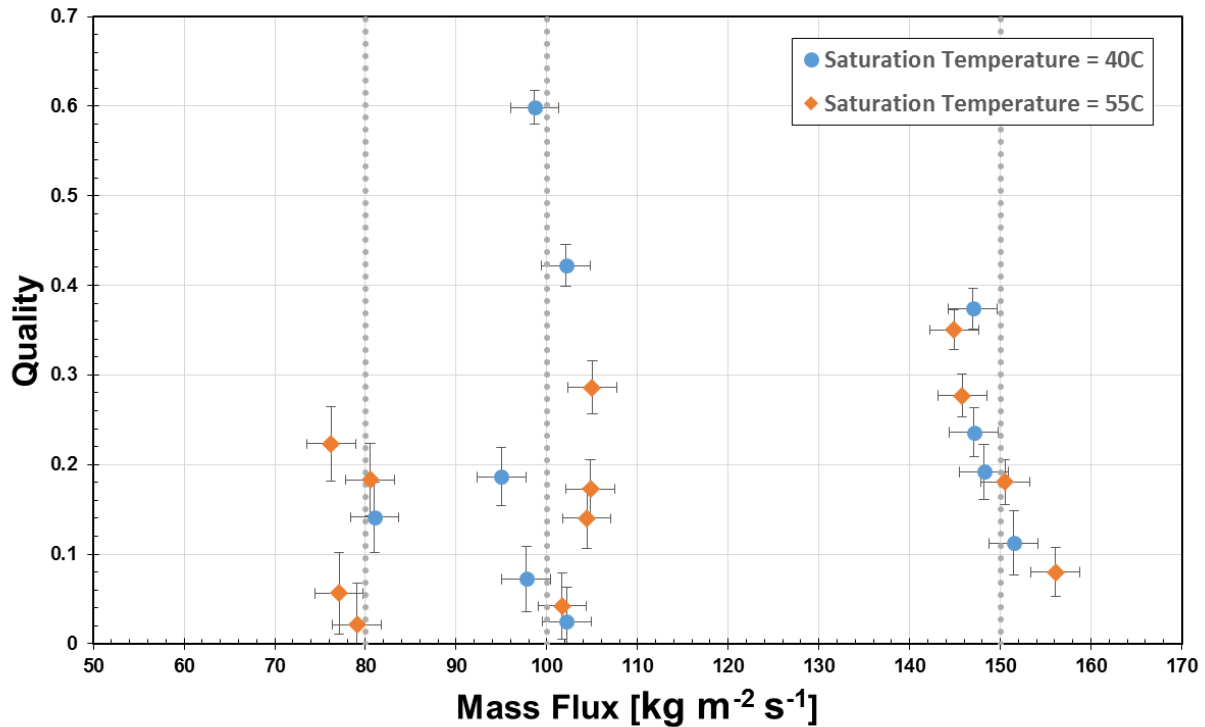


Figure 4.2 - Collected data from both saturation temperatures, heat loss estimations and uncertainty incorporated into mass flux and quality estimations

Table 4.2 - Collected data from both saturation temperatures, heat loss estimations and uncertainty incorporated into mass flux and quality estimations

Saturation Temperature [C]	Mass Flux [kg/s-m ²]	Viewing Section Quality	Vapor Velocity [m/s]	Liquid Velocity [m/s]	Test Section Pressure [PSI]	Working Fluid Pump Inlet [C]	Working Fluid Pump [ml/min]	Working Fluid Inlet [C]	Working Fluid Outlet [C]	Cooling Fluid Pump [ml/min]	Coolant Inlet [C]	Coolant Outlet [C]
40	98.66 ± 2.7	0.60 ± 0.02	8.39E-07	2.45E-08	149.7	12.1	16.72	46.8	39.9	10.00	11.33	42.1
40	102.10 ± 2.7	0.42 ± 0.02	6.08E-07	3.65E-08	150.9	12.12	17.3	47.7	40.2	15.00	10.06	41.3
40	81.00 ± 2.7	0.14 ± 0.04	1.58E-07	4.32E-08	153.5	12.16	13.73	54.8	40.8	17.00	10.13	42.8
40	94.97 ± 2.7	0.19 ± 0.03	2.46E-07	4.80E-08	153.3	12.02	16.09	47.5	40.6	20.00	10.08	40.6
40	97.74 ± 2.7	0.07 ± 0.04	9.93E-08	5.62E-08	151.5	11.9	16.56	47.1	40.2	25.00	10.42	39.5
40	102.20 ± 2.7	0.02 ± 0.04	3.66E-08	6.15E-08	147.2	11.84	17.3	47.5	39.2	30.00	10.71	37.9
40	147.00 ± 2.7	0.37 ± 0.02	8.19E-07	5.66E-08	150.7	11.67	17.58	43.2	40.0	35.00	11.43	37.3
40	147.10 ± 2.7	0.24 ± 0.03	4.98E-07	6.94E-08	144.2	11.19	24.86	50.7	38.2	29.50	10.96	38.2
40	148.20 ± 2.7	0.19 ± 0.03	4.09E-07	7.40E-08	149.4	10.87	24.84	49.8	39.6	37.00	11.84	37.5
40	151.50 ± 2.7	0.11 ± 0.04	2.47E-07	8.30E-08	148.7	10.77	25.02	51.3	39.4	43.00	12.69	36.5
55	156.10 ± 2.7	0.08 ± 0.03	5.76E-07	4.73E-07	218.3	11.06	26.33	63.9	54.7	27.00	11.12	52.9
55	150.50 ± 2.7	0.18 ± 0.03	1.25E-06	4.06E-07	218.3	11.27	25.4	64.6	54.6	22.50	10.43	54.1
55	145.80 ± 2.7	0.28 ± 0.02	1.88E-06	3.47E-07	217.1	11.45	24.63	65.5	54.4	19.00	10.55	56.1
55	144.90 ± 2.7	0.35 ± 0.02	2.31E-06	3.11E-07	220.7	11.39	24.46	64.6	55.1	16.50	10.34	56.5
55	101.70 ± 2.7	0.04 ± 0.04	1.95E-07	3.22E-07	221.3	12.19	17.2	65.3	55.2	17.00	10.28	55.5
55	104.40 ± 2.7	0.14 ± 0.03	6.81E-07	2.96E-07	216.2	12.35	17.68	63.3	54.3	15.50	10.71	55.4
55	104.80 ± 2.7	0.17 ± 0.03	8.25E-07	2.86E-07	220.6	12.35	17.74	62.2	55.2	14.50	10.79	55.7
55	105.00 ± 2.7	0.29 ± 0.03	1.39E-06	2.47E-07	217.4	12.33	17.78	63.2	54.5	13.00	10.78	55.3
55	76.20 ± 2.7	0.22 ± 0.04	7.71E-07	1.96E-07	221.7	12.54	12.91	63.5	55.4	10.00	12.11	57.1
55	80.51 ± 2.7	0.18 ± 0.04	6.69E-07	2.17E-07	221.1	12.49	13.64	63.2	55.2	11.00	11.75	57.0
55	77.09 ± 2.7	0.06 ± 0.05	1.96E-07	2.41E-07	222.4	12.4	13.05	62.5	55.5	12.00	11.53	56.4
55	79.08 ± 2.7	0.02 ± 0.05	7.72E-08	2.56E-07	220.6	12.38	13.39	63.5	55.0	13.00	11.37	56.4

Somewhat surprisingly, little variability was found in the flow regime observed over the range of quality ($0.02 < x_{\text{avg}} < 0.60$), saturation temperature, and mass flux investigated here. That is, there was no clear transition from annular/wavy flow to intermittent flow. A preliminary assessment of the experimental matrix using the Nema et al. (2014) flow map predicted a transition directly from annular to intermittent flow would be observed. This flow regime would be expected to be visually identifiable in both vertical and horizontal view angles (see for example, Figure 4.3, the present test section imaged from above). Furthermore, it was predicted by the Nema et al. (2014) map and suggested by flow visualization by Coleman & Garimella (2000) that there would not be any stratified/wavy regime at these small diameters. However, neither of these studies considered mass fluxes as low as those in the present study.

Visualization of Intermittent Flow

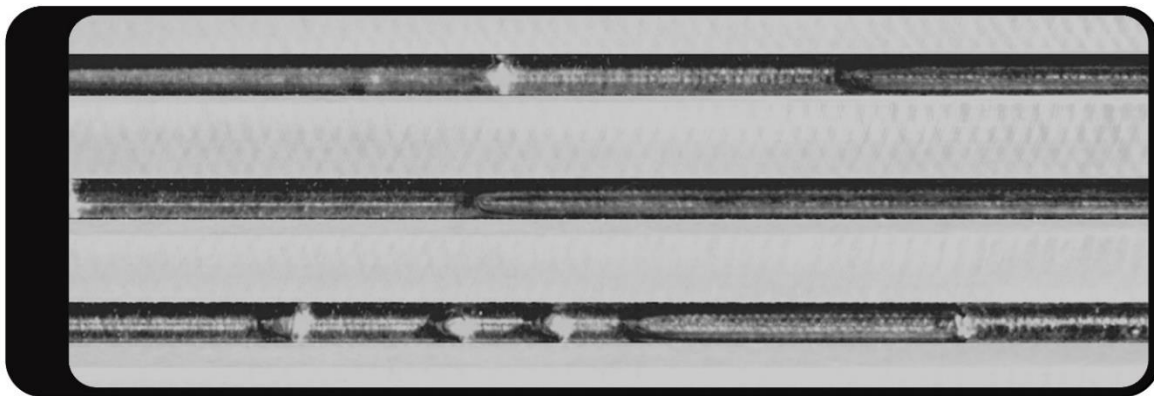


Figure 4.3 - Visualization of intermittent flow, as captured during initial experimentation heater testing

Due to the fact that visualization data was captured from above the flow, flow regimes of wavy and wavy-annular would appear visually the same in the present experimental setup. Since intermittent flow was not observed, the only flow regime observed was either a stratified-wavy or annular-wavy flow regime. While it was not possible to discern between stratified and annular flow, the fact that the expected intermittent flow was not observed is a significant result.

Still images from the high-speed video are presented below. As the variation of the flow is difficult to see in still frames, the video footage used to produce the images is made available at the open source hosting location: <https://figshare.com/s/8a2c9e9d1bb60e67ee40>

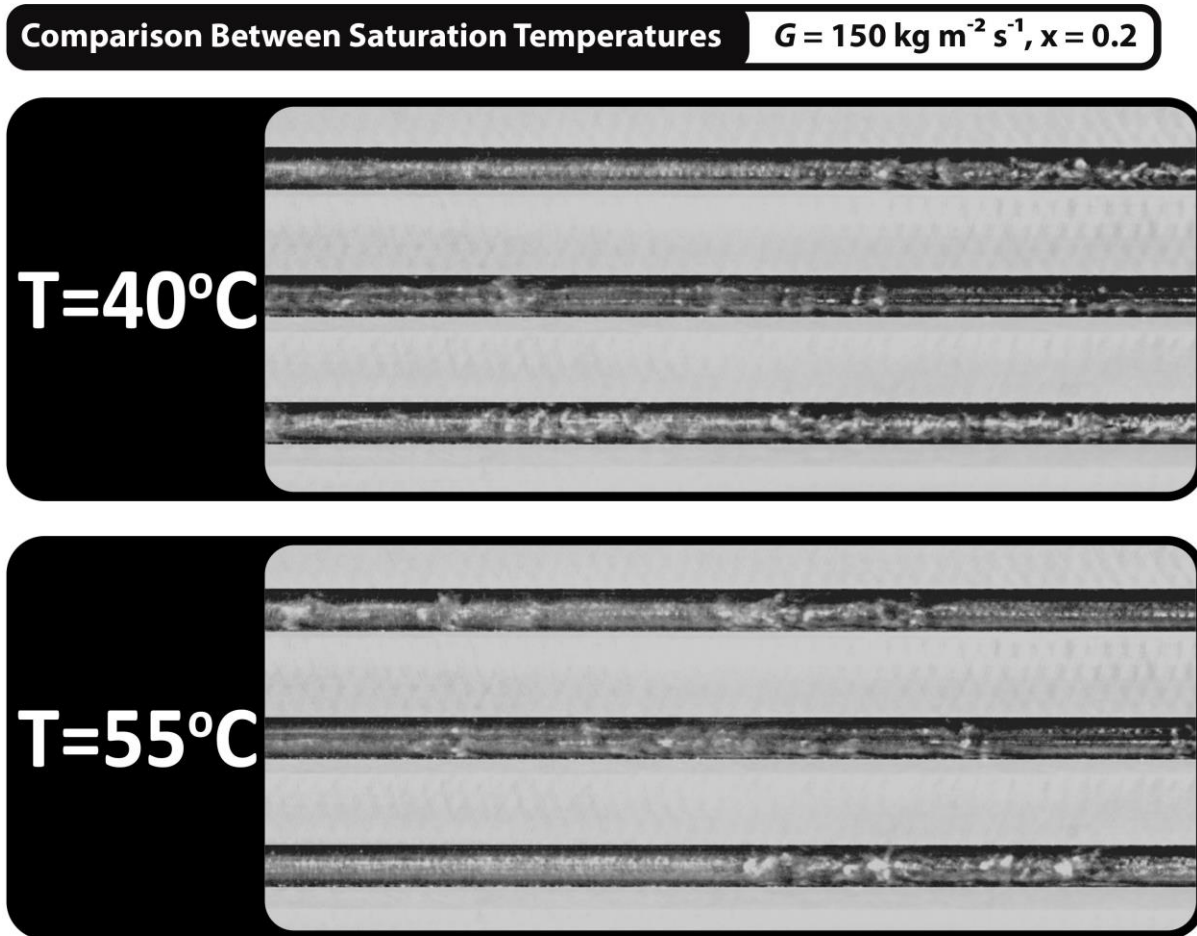


Figure 4.4 - Comparing visualization results while varying saturation temperature

At the two saturation temperatures tested, fluid properties that affect the flow dynamics differ significantly. Moving from $T_{\text{sat}} = 40^\circ\text{C}$ to 50°C , the liquid viscosity decreases 18%, and the vapor density increases 52%. The vapor viscosity and liquid density stay relatively the same, with changes under 8%. Figure 4.4 above compares the effect of differing saturation temperature between two data points at the same nominal average quality ($x = 0.2$) and mass flux ($G = 150 \text{ kg m}^{-2} \text{ s}^{-1}$). This comparison shows that there is very little visual difference between the flow regimes for both saturation temperatures at the same quality and mass flux.

Figure 4.5 shows images obtained at different thermodynamic qualities, maintaining the same mass flux and saturation temperature. The figure shows that varying quality changes the relative amount of vapor and liquid visible in the flow, but the observed flow regime, with wavy liquid-vapor interfaces, does not change. When the videos are viewed, one can observe larger lengths of smooth, or fully liquid flow, with shrinking and less frequent wavy vapor packets as quality decreases and the volume of liquid increases.

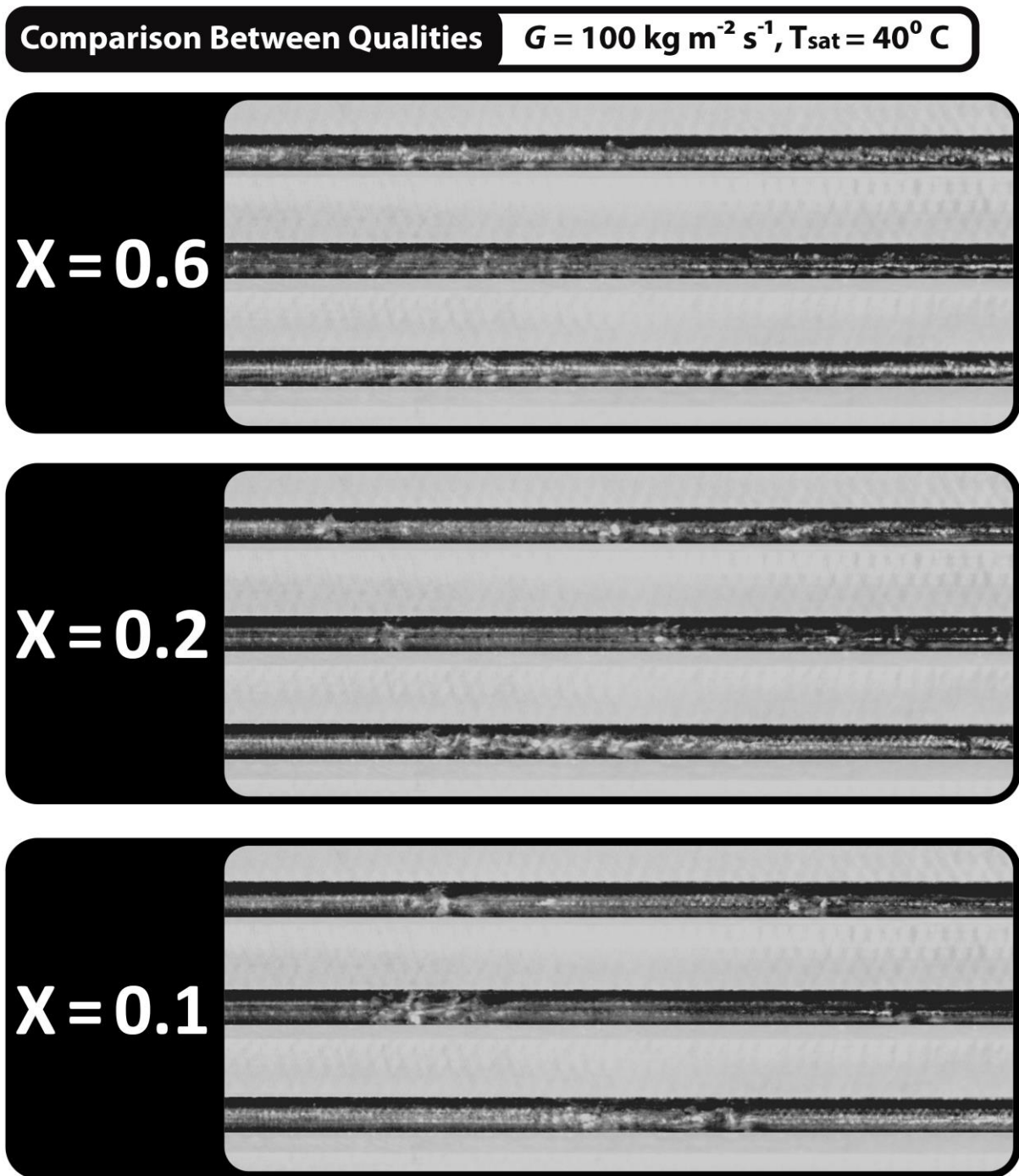


Figure 4.5 - Comparing visualization results while varying flow quality

Figure 4.6 shows results for varying mass fluxes along similar qualities ($0.3 < x < 0.4$) and saturation temperature, the same flow regime of wavy vapor-liquid interfaces is visible. With increasing mass flux, an increase in flow turbulence is also visible, with fewer and shorter lengths of stable flow visible between wave troughs.

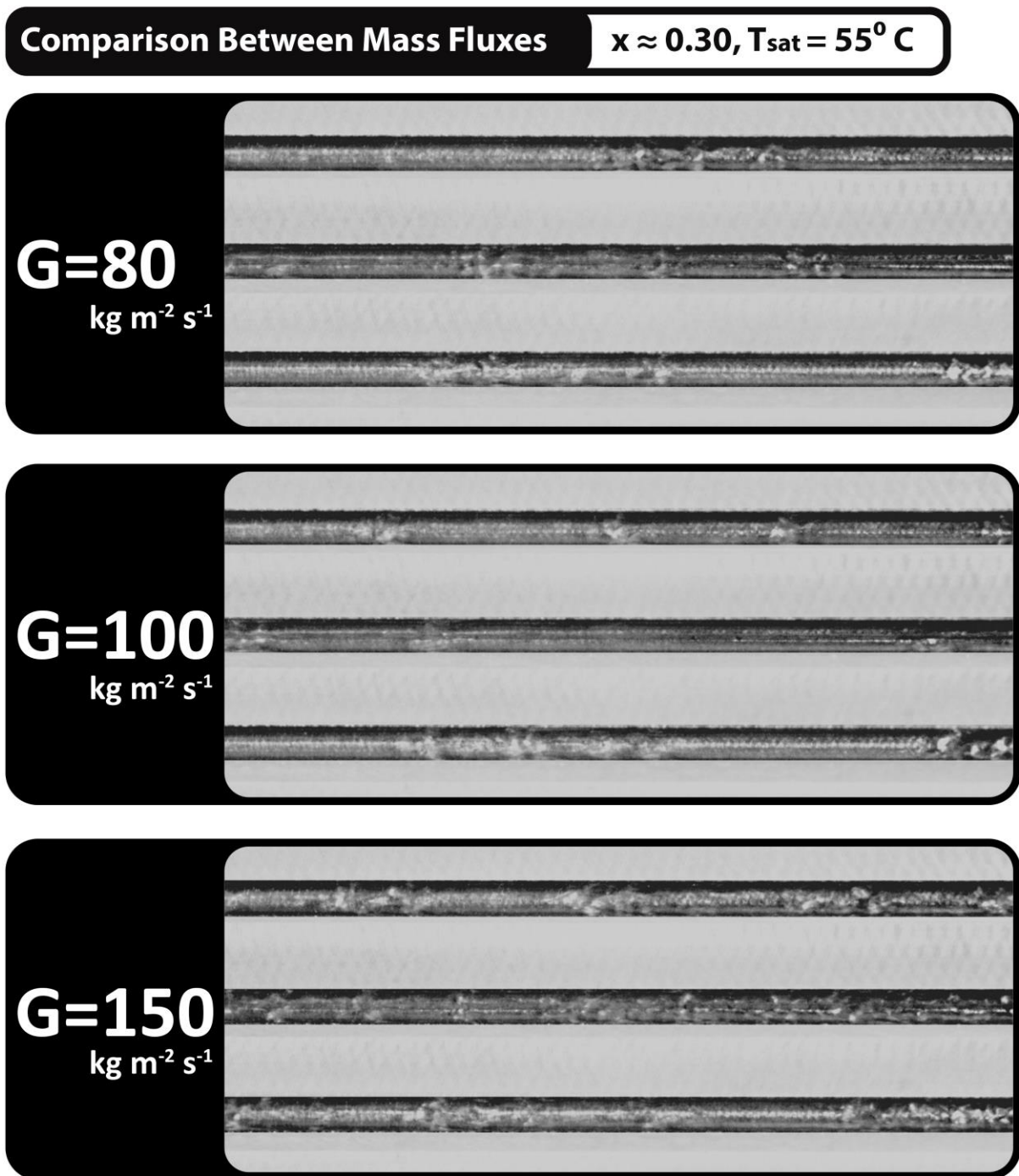


Figure 4.6 - Comparing visualization results while varying mass flux

Visually identifying the differences between flows as quality lowers (as seen in Figure 4.5) from high to low, it can be seen that longer and longer sections of the flow appear as smooth sections of fluid without perturbation. As more liquid is present in the channels, wave troughs would more frequently top out into liquid-only segments of channel length. Knowing that at lower qualities more liquid would be present than

vapor, these long lengths of smooth flow can be identified as fully liquid. Due to this, the observed flow regime is believed to be a wavy-stratified flow.

If the flows were wavy-annular, the smooth sections would represent annular areas without waves, either primarily composed of vapor or liquid. If the smooth segments of flow were vapor, the opposite trend of increasing length of smooth sections with increasing quality would be expected. If the smooth segments were liquid in an annular flow, a more clear transition from liquid to annular sheets of liquid and vapor would be visible, similar to the intermittent flow shown above in Figure 4.3.

It cannot be stated with complete certainty that the flow regime observed in the present data is a stratified-wavy or simply wavy flow without further investigation. Further experiments will seek to further investigate these data points, with visualization of flow from the side in vertically configured channels to confirm flow regime.

4.2 ANALYSIS OF UNCERTAINTY

To best compare the data collected to modeled expectations, a high level of data certainty was desired. To support data collection with uncertainties less than 15%, a detailed analysis was performed in both the design and data collection stages. The section below details the analysis performed on system and data uncertainty, and provides examples using collected data to support the analysis. For reference, a diagram of the DAQ stages of data collection from various system sensors is shown below in Figure 4.7.

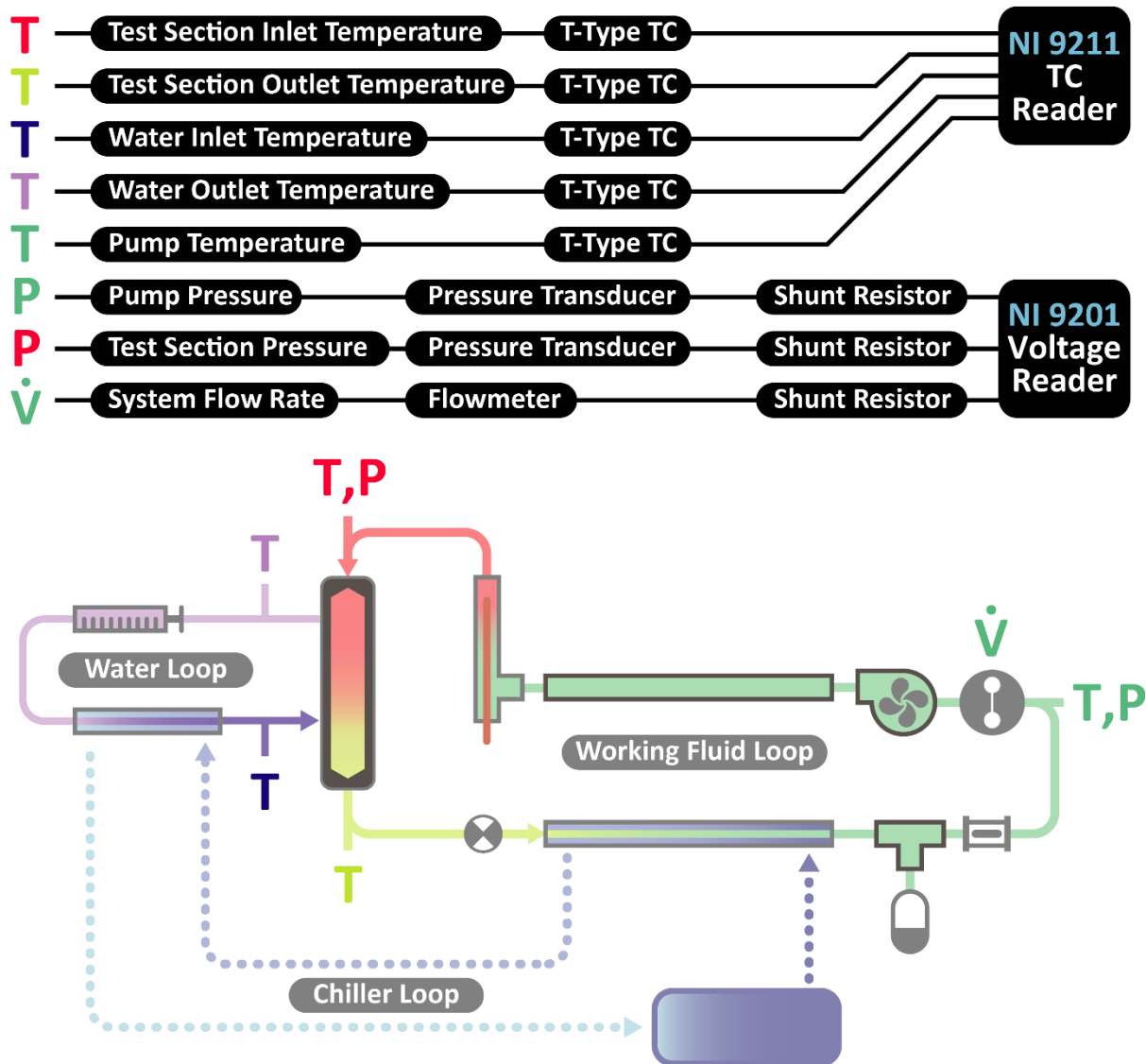


Figure 4.7 - DAQ systems diagram

4.2.1 INSTRUMENT UNCERTAINTY

As a first pass at the system variable uncertainty, the instrument uncertainty (U_0) encompasses a large majority of the uncertainty that can be expected in the system. The instrument, or design level uncertainty, is estimated using the known sensor uncertainties as reported by the manufacturer or established through calibration. This level of uncertainty was used to aid in the design process when selecting component sizes and designing the test section, and represents the researcher's best guess at system performance before a physical system exists. The uncertainties of each sensor element are listed below for reference in Table 4.3. Some uncertainties below are listed absolutely as uncertainties which do not change with reading, and some are represented variably as percentages of the sensor reading, based on manufacturer reported values.

Table 4.3 - Instrument level uncertainty as reported by the manufacturer

	Reading	Sensor	Scale Range	Units	U_0
U_0	Pressure	Omega PX209-300Ai	0.00 – 300	PSI	0.3750
	Temperature	Omega T-type Thermocouples	-270 – 400	°C	0.5000
	R-134a Flowrate	DEA Nutating Flowmeter FMTD4	1.00 – 250	ml/min	1.000%
	Water Flowrate	New Era NE-1010 Syringe Pump	0 – 125	ml/min	1.000%

The thermocouples, calibrated as discussed in Section 3.4, with a high-accuracy thermistor, were assigned the default accuracy of $\pm 0.5^\circ\text{C}$ (as reported by the manufacturer) due to the limited number of calibration points used in the calibration.

4.2.2 MEASUREMENT UNCERTAINTY

The measurement level uncertainty (U_1) is a measurement of the physical reading capabilities of the data acquisition (DAQ) system as it reads the analog signals from the sensors via collection of digitized bits of information. Because the water-side syringe pumps are read by the researcher and recorded at a steady value, the measurement uncertainty inherent with the reading is taken as half the least significant digit not able to be displayed by the readout. For the four digit display on the NE-1010 Syringe Pump, this related to an expected error of 0.0005 ml/min.

For the thermocouples, readings were made from a NI 9211 DAQ Module, which is reported by the manufacturers to have at most a 0.07°C reading error for T-type thermocouples. This error incorporates errors from gain, offset, differential and integral nonlinearity, quantization, noise, and isothermal errors.

In order to limit power losses in the sensor lines, and therefore introduce additional measurement error, the pressure transducers and flow meter readings were transmitted using a 4-20 mA signal. The signal was

modified using a 250 Ohm shunt resistor, wired in series with the 4-20 mA signal, which produced a 0-5 V excitation voltage that could be read using a voltage reader. Data acquisition uncertainties from the pressure transducers and the flow meter come from reading the voltage across the resistor (with associated uncertainties) and a $\pm 10V$ NI 9201 voltage reading DAQ Module with 12 bit accuracy.

To determine the associated measurement uncertainty, the uncertainty of the resistor value must be taken into account along with the resolution error of the DAQ module. The resolution of the DAQ reader is multiplied by the full scale reading to estimate the smallest increment able to be read, shown in Equation (4.4) below:

$$\left(\frac{FRR}{2^N}\right) \times \left(\frac{FSR}{V_{\max}}\right) \quad (4.4)$$

The full reading range (FRR) of the DAQ is divided by 2^N (where N is the number of bits in the reader) to establish the smallest physical voltage the card is capable of reading. The sensitivity, in volts, is converted to reading units by multiplying it by the full sensor range (FSR) in reading units over the maximum associated voltage that value would produce. Equation (4.5) below shows an example calculation for the pressure transducers used in this study:

$$\left(\frac{20V}{2^{12}}\right) \times \left(\frac{300psi}{5V_{\max}}\right) = 0.2930psi \quad (4.5)$$

The uncertainty of the 250 Ohm CMF resistors used in line to measure this voltage is reported as 0.1% by the manufacturer. To use this uncertainty to estimate the expected voltage error in the reading, it must be converted to a value in measured units. Because the conversion from current to voltage is a linear equation with resistance, this percentage uncertainty in resistance can be applied directly to the voltage reading, and converted into the same units as the reading via Equation (4.6) below. Using the example of the pressure transducers, this would correlate to an expected uncertainty of 0.3000 PSI.

$$\left(\frac{FSO}{5V_{\max}}\right) \times (5V_{\text{signal}} \times 0.1\%) = FSO \times 0.1\% \quad (4.6)$$

For a complete estimate of measurement level uncertainty, the uncertainties from both the DAQ reading and voltage across the resistor must be combined in a total estimate. Because it is not expected that the worst case of both uncertainties would be present at any given time, the values are combined using the root-mean-sum (RMS) method to estimate the total U_1 uncertainty. The uncertainty from data acquisition can be seen in Table 4.4 below. All uncertainties are listed in units of the signal reading.

Table 4.4 - Data acquisition level uncertainty

	Reading	Scale Range	Units	$U_{1,DAQ}$	$U_{1,Voltage}$	U_1
U_1	Pressure	0 – 300	PSI	0.2930	0.3000	0.4193
	Temperature	-270 – 400	°C	0.0350	Accounted for in DAQ reading	0.0350
	R-134a Flowrate	0 – 250	ml/min	0.2441	0.2500	0.3494
	Water Flowrate	0 – 125	ml/min	0.0005	0.0000	0.0005

4.2.3 VARIABILITY UNCERTAINTY

Because each measurement taken at each data point was composed of a series of readings during the data acquisition process, there is an uncertainty associated with the variability of sampled data. The variability uncertainty (U_2) can be estimated by measuring the difference between multiple measurements taken over the range of a single data point. During data collection, measurements of fluid conditions were taken at a rate of 4Hz, for approximately 9-10 seconds per data point. The variability in data collection over this time period adds an additional uncertainty to the time-averaged value used to plot a single point. The uncertainty in the sample mean can be estimated as a function of the sample number and standard deviation as shown below in Equation (4.7).

$$SE_{\bar{x}} = t_{\alpha,df} \times \left(\frac{s}{\sqrt{df}} \right) \quad (4.7)$$

Because the true signal standard deviation is not known, it is assumed that the error follows a Gaussian distribution along the data collected and that the signal standard deviation (σ) can be estimated using s , an estimate of the sample standard deviation. This assumption adds additional uncertainty, so the student- t distribution is used to estimate this additional uncertainty given the samples degrees of freedom ($n-1$) and a confidence level (α) of 95%. Data variability uncertainty, U_2 , was typically well under 1.0% of the sensor reading value.

The uncertainty from data variability was added to the inherent uncertainties (design and acquisition) in each measurement using the RMS method $\left(U_x = \sqrt{U_0^2 + U_1^2 + U_2^2} \right)$ to achieve a final measurement uncertainty in each data reading. To calculate the data uncertainty, the maximum uncertainty for each reading (across both saturation temperatures of data) was used, assuming a “worst case” data uncertainty. Typical final measurement uncertainties are provided below for a sample data point.

U_x	Variable	System Pressure	T Water In	T Fluid Out	T Water Out	T Fluid In	T At Pump	Flow Meter	Syringe Pumps
	Units	PSI	°C	°C	°C	°C	°C	ml/min	ml/min
	Average	220.59	10.79	55.17	55.67	62.24	12.35	17.74	14.50
	Uncertainty	0.61	0.5	0.5	0.5	0.5	0.5	0.45	0.27
	Percentage	0.3%	4.6%	0.9%	0.9%	0.8%	4.0%	2.5%	1.9%

4.2.4 ADDITIONAL SOURCES OF UNCERTAINTY

While the uncertainties in each measurement were able to be determined via RMS of known manufacturer's values, the operational heat losses in the system are not captured through direct measurement. Heat loss studies were run independently on the water and working fluid sides at a variety of fluid temperatures and flow rates. Trim heaters were used at the fluid inlet to produce variable and stable temperatures using a PID controlled feedback loop. The temperature drop from inlet to outlet, flowrate, and fluid properties were used to create a third order polynomial curve fit of energy lost to the surroundings as a function of average fluid temperature and mass flowrate for each fluid. Data was taken at steady state conditions using fully liquid flows.

Because the calibrated curve is used to estimate the energy loss from the system to the environment, an error is introduced that can be estimated through the sum of squared errors (*SSE*) and the degrees of freedom (*df*) in the curve fit function. The error introduced by the curve fit (*SE_Q*) is calculated using Equation (4.8) below, and can be used to estimate the percent error in the heat loss estimation.

$$SE_Q = \sqrt{\frac{\sum (Q_i - \hat{Q}_i)^2}{n_{data} - n_{coeff}}} = \sqrt{\frac{SSE}{df}} \quad (4.8)$$

An example of the heat map developed for the working fluid side is shown below in Figure 4.8, depicting the measurement of heat entering the system at a variety of flow rates and average fluid temperatures. Ideally, the heat map developed for estimating the heat loss from the system would have been compared to additional data points not incorporated in the map already as an evaluation of model's uncertainty. Unfortunately, due to seasonal lab and HVAC temperature and air circulation changes, the ambient room conditions changed significantly after heat loss mapping and flow data collection, limiting the model to data captured during the same ambient conditions.

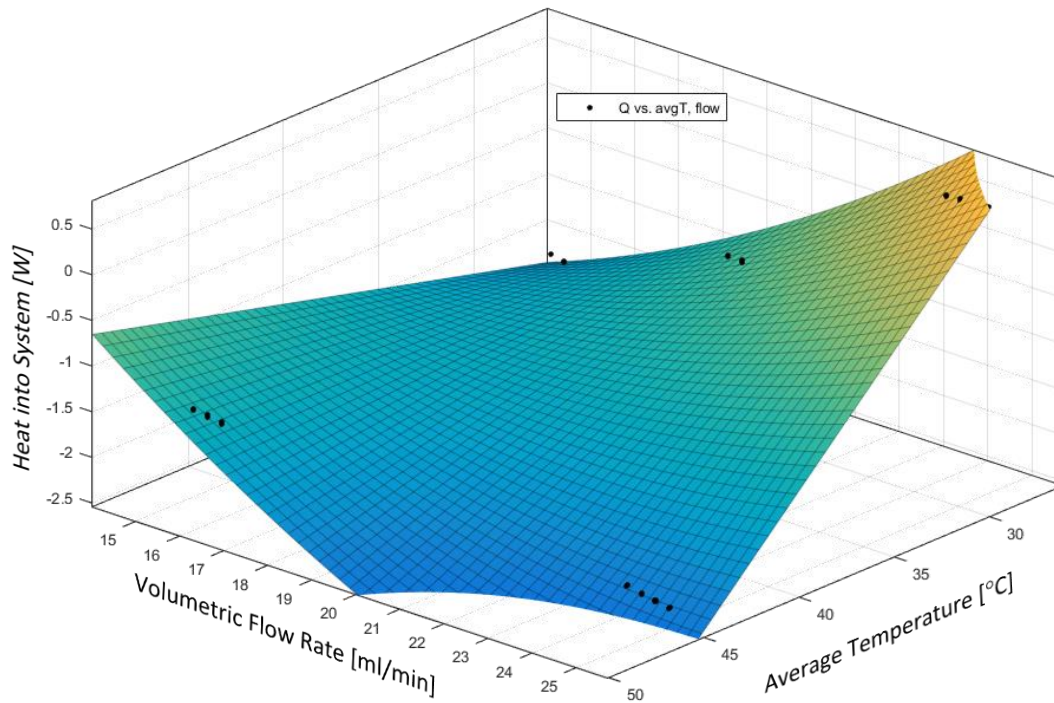


Figure 4.8 - Heat map developed for working fluid operation

Additionally, because the flow channel diameter is a measured variable used in calculating the fluid mass flux, it is necessary to develop a measurement uncertainty for the five channels observed during testing. By assuming through the model that all channels are the same dimension, a level of uncertainty is introduced in the calculations. As shown in Table 3.5 in Section 3.1.2, the channel dimensions did in fact differ.

The channel dimensions were measured with a Zygo Zescope optical 3D-profiler to achieve a measurement for channel width and depth. For the objective and magnification used, the Zescope has a reported optical resolution of 2.12 μm . This was used to take measurements of the dimensions of each channel as machined. The channel depths and heights were all collected to establish a hydraulic diameter for each channel. The variances in calculated hydraulic diameter were used to establish a standard error associated with the average hydraulic diameter, using the Equation (4.9) below for estimating the standard error in a known population.

$$SE_{D_h} = \left(\frac{\sigma}{\sqrt{n}} \right) \quad (4.9)$$

Because the five channels sampled represent the entire population of channels, the population standard deviation (σ) is known and can be used along with the actual population quantity (n). The accuracy of the

Zescope, along with the deviation in measured channel size was root-sum-squared to estimate a channel hydraulic diameter of $842.49 \pm 11.66 \mu\text{m}$.

4.2.5 ESTIMATED UNCERTAINTY OF CALCULATED PARAMETERS

For each data point collected, the quality and mass flux were determined using *Engineering Equation Solver* (F-Chart Software 2016), with uncertainties tabulated using the Kline-McClintock (1953) method. Uncertainties on each measurement were entered into the program, and a final uncertainty on the calculated value was determined by weighting each uncertainty in the total root-sum-squared error using partial differentials of the equation with respect to each variable uncertainty, as shown below in Equation (4.10).

$$U_G = \sqrt{\left(\frac{\partial G}{\partial x_1} U_1\right)^2 + \left(\frac{\partial G}{\partial x_2} U_2\right)^2 + \dots + \left(\frac{\partial G}{\partial x_n} U_n\right)^2} \quad (4.10)$$

The final uncertainties in mass flux and quality can be calculated through this method, and the constituent uncertainties from each variable can be displayed in the EES readout. A sample collection of final uncertainties (as a result of the sample baseline uncertainties shown above) can be seen below in Figure 4.9.

<u>G = 104.8±2.688 [kg/s-m²]</u>		
Flowmeter = 17.74±0.4543 [ml/min]	$\partial G / \partial \text{Flowmeter} = 5.907$	99.71 %
SyringePumps = 14.5±0.27 [ml/min]	$\partial G / \partial \text{SyringePumps} = 4.626\text{E-}16$	0.00 %
T _{f,in} = 62.24±0.5 [C]	$\partial G / \partial T_{f,in} = 0$	0.00 %
T _{f,out} = 55.17±0.5 [C]	$\partial G / \partial T_{f,out} = 0$	0.00 %
T _{pump} = 12.35±0.5 [C]	$\partial G / \partial T_{\text{pump}} = -0.2909$	0.29 %
T _{w,in} = 10.79±0.5 [C]	$\partial G / \partial T_{w,in} = 0$	0.00 %
T _{w,out} = 55.67±0.5 [C]	$\partial G / \partial T_{w,out} = 0$	0.00 %
TestPressure = 220.6±0.6128 [PSI]	$\partial G / \partial \text{TestPressure} = 0.002658$	0.00 %
U _{Qf} = 1±0.02568	$\partial G / \partial U_{Qf} = 0$	0.00 %
U _{Qw} = 1±0.3167	$\partial G / \partial U_{Qw} = 0$	0.00 %
<u>x_{out} = 0.1726±0.03222</u>		
Flowmeter = 17.74±0.4543 [ml/min]	$\partial x_{\text{out}} / \partial \text{Flowmeter} = 0.04992$	49.56 %
SyringePumps = 14.5±0.27 [ml/min]	$\partial x_{\text{out}} / \partial \text{SyringePumps} = -0.05753$	23.25 %
T _{f,in} = 62.24±0.5 [C]	$\partial x_{\text{out}} / \partial T_{f,in} = 0.01714$	7.08 %
T _{f,out} = 55.17±0.5 [C]	$\partial x_{\text{out}} / \partial T_{f,out} = -0.0007729$	0.01 %
T _{pump} = 12.35±0.5 [C]	$\partial x_{\text{out}} / \partial T_{\text{pump}} = -0.002458$	0.15 %
T _{w,in} = 10.79±0.5 [C]	$\partial x_{\text{out}} / \partial T_{w,in} = 0.01972$	9.36 %
T _{w,out} = 55.67±0.5 [C]	$\partial x_{\text{out}} / \partial T_{w,out} = -0.01747$	7.35 %
TestPressure = 220.6±0.6128 [PSI]	$\partial x_{\text{out}} / \partial \text{TestPressure} = -0.001064$	0.04 %
U _{Qf} = 1±0.02568	$\partial x_{\text{out}} / \partial U_{Qf} = 0.06803$	0.29 %
U _{Qw} = 1±0.3167	$\partial x_{\text{out}} / \partial U_{Qw} = -0.01731$	2.90 %

Figure 4.9 - Sample EES results from Kline-McClintock uncertainty analysis

The final tabulated data uncertainties for each data point are shown in Table 4.2 above. In general, uncertainties in the mass flux parameter were approximately 3%, on average. For the thermodynamic quality, which ranges from 0.00 to 1.00, the traditional percent uncertainty of reading results in a misleading result as data points closer to zero receive an inflated uncertainty - sometimes greater than 100%. When calculating the uncertainty as a percent of the full range, data uncertainty remains under 6% for all points measured, and is ± 0.03 on average.

4.3 ANALYSIS OF DATA

This section makes observations of flow regime trends found in the data, and establishes the trend found in the results. The results are then compared to the predictions made by the various flow maps investigated in Section 2.2.2.

4.3.1 FLOW REGIME OBSERVATIONS

As discussed above in Section 4.1, the flow regimes observed in the study are difficult to identify due to the orientation of the image with respect to the gravity and body forces. The observed flow regimes could be either a stratified-wavy flow, or an annular-wavy flow, making it difficult to determine with certainty if one or both are present.

However, it *can* be said with absolute certainty that what was observed was neither stratified, bubbly, intermittent, or mist flow, nor was it smooth annular flow. With this knowledge the observations can still be well compared to the expectations of the various flow maps summarized above, characterizing at the minimum which maps predicted incorrectly. The section below makes this comparison, developing the flow maps proposed by a variety of authors and plotting their predictions against the data observed.

4.3.2 COMPARISON TO POPULAR FLOW MAPS

The collected data was compared to the predictions made by the flow regime models reviewed in Section 2.2.2. The sections below provide an objective evaluation of the models presented. Observations are made of each flow map evaluating the accuracy of them when predicting the results presented.

4.3.2.1 Taitel & Dukler (1976)

The Taitel and Dukler (1976) flow map was developed based on a set of five dimensionless parameters to capture the relative effects of liquid-vapor mass flow rates, tube diameter and inclination, and fluid properties (neglecting surface tension). The parameters T , Y , F (the modified Froude number), K , and X (the Martinelli parameter) are defined below as they are in the original work in Equations (4.11) through (4.15). The parameters used to define these dimensionless constants are elaborated upon further in the original work.

$$T = \left[\frac{4C_L \left(\frac{u_L^s D}{\nu_L} \right)^{-n} \left(\frac{\rho_L u_L^s{}^2}{2} \right)}{g(\rho_L - \rho_G) \cos(\alpha)} \right]^{\frac{1}{2}} = \left[\frac{|(dP/dx)_L^s|}{g(\rho_L - \rho_G) \cos(\alpha)} \right]^{\frac{1}{2}} \quad (4.11)$$

$$Y = \left[\frac{g(\rho_L - \rho_G) \sin(\alpha)}{\frac{4C_G \left(\frac{u_G^s D}{\nu_G} \right)^{-m} \left(\frac{\rho_G (u_G^s)^2}{2} \right)}{D}} \right] = \left[\frac{g(\rho_L - \rho_G) \sin(\alpha)}{|(dP/dx)_G^s|} \right] \quad (4.12)$$

$$F = \sqrt{\frac{\rho_G}{(\rho_L - \rho_G)}} \left(\frac{u_G^s}{\sqrt{Dg \cos(\alpha)}} \right) \quad (4.13)$$

$$K = F \left[\text{Re}_L^s \right]^{\frac{1}{2}} \quad (4.14)$$

$$X = \left[\frac{4C_L \left(\frac{u_L^s D}{\nu_L} \right)^{-n} \left(\frac{\rho_L (u_L^s)^2}{2} \right)}{\frac{4C_G \left(\frac{u_G^s D}{\nu_G} \right)^{-m} \left(\frac{\rho_G (u_G^s)^2}{2} \right)}{D}} \right]^{\frac{1}{2}} = \frac{|(dP/dx)_L^s|}{|(dP/dx)_G^s|} \quad (4.15)$$

The model defined a specific set of dimensionless values that could be compared to lines of defined flow transition. The flow transition lines, defined by T_{tran} , F_{tran} , and K_{tran} , can be plotted against X to determine the bounds of each flow regime. The parameter Y is primarily used to capture changes in pipe inclination, and is not included as a transition boundary directly. The transition criteria are presented below, in Table

4.5. Equations (4.16) through (4.18). Definition of the various flow regimes for horizontal tubes only are summarized in Table 4.5 below.

$$F_{trans} = \sqrt{\frac{C_2^2 \tilde{A}_G}{\tilde{u}_G (d\tilde{A}_L/d\tilde{h}_L)}} \quad (4.16)$$

$$T_{trans} = \sqrt{\frac{8\tilde{A}_g}{\tilde{S}_l \tilde{u}_L^2 (\tilde{u}_L \tilde{D}_L)^{-n}}} \quad (4.17)$$

$$K_{trans} = \frac{2}{\sqrt{\tilde{u}_L \tilde{u}_G} \sqrt{s}} \quad (4.18)$$

Table 4.5 - Flow transition criteria for the Taitel and Dukler flow map

Flow Regime	As Published	Transition Criteria
Wavy	“Stratified Wavy”	$F < F_{trans}, K > K_{trans}$
Annular	“Annular-Dispersed”	$F > F_{trans}, X < 1.6$
Stratified	“Stratified Smooth”	$K < K_{trans}$
Dispersed	“Dispersed Bubble”	$X > 1.6, T > T_{trans}$
Intermittent	“Intermittent”	$X > 1.6, T < T_{trans}$

The collected data was plotted against the transition criteria shown in Table 4.5, shown below in Figure 4.10. Note that at the scale shown, error bars are not visible beneath the data points plotted.

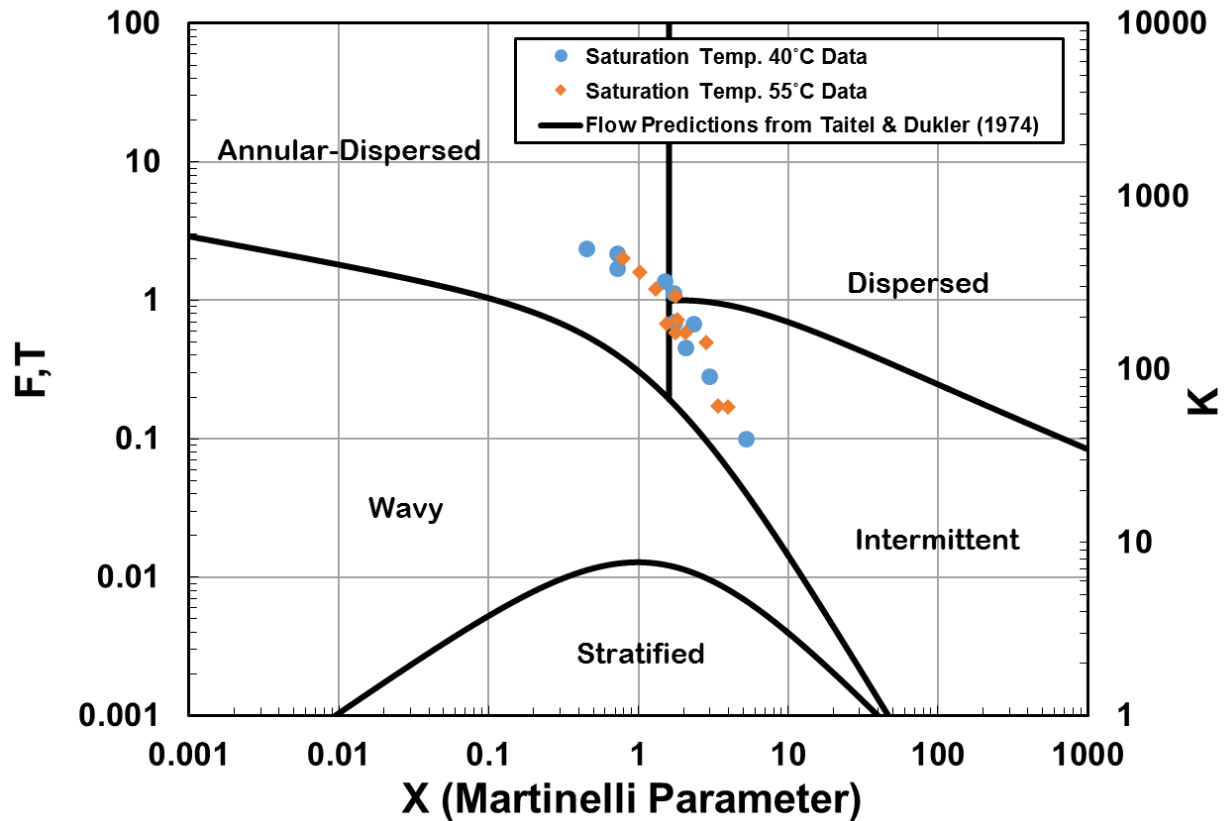


Figure 4.10 - Experimental data plotted against the Taitel and Dukler (1976) proposed map

Comparing the results of data visualization to the predictions made by the Taitel and Dukler (1976) model, it can be seen that there are discrepancies. While the data points collected were all either wavy or annular flow, predictions placed the points in the transition between annular and intermittent. While it is possible that the flows observed were annular flow, the model would still incorrectly predict 22% of the data points collected. It is interesting to note however that the trend closely follows the line defining the transition to wavy flow. It is possible that with small modifications to the transition parameters, the map would more accurately predict the trends observed.

4.3.2.2 Cavallini et al. (2002)

The flow regime prediction model proposed by Cavallini et al. (2002) makes use of the dimensionless vapor velocity, j_v^* , to determine a transition line above which all flow becomes annular. Additionally, the model relies on the modified Martinelli parameter X_{tt} , as well as the critical mass flux G_W , as defined by (Rabas and Arman 2000). The parameters used in the model are defined below.

$$j_v^* = \frac{Gx}{(gD\rho_G(\rho_L - \rho_G))^{0.5}} \quad (4.19)$$

$$X_{tt} = \left(\frac{\mu_L}{\mu_G}\right)^{0.1} \left(\frac{\rho_G}{\rho_L}\right)^{0.5} \left(\frac{1-x}{x}\right)^{0.9} \quad (4.20)$$

$$G_W = (\pi/4) Fr \sqrt{g \rho_L D_H^{1.5}} \quad (4.21)$$

The model was fit to specific values of these parameters as transition lines, which were used to define flow regimes bounded by the transitions. The flow regimes predicted by the Cavallini et al. (2002) model are shown below in Table 4.6.

Table 4.6 - Flow transition criteria for the Cavallini et al. (2002) flow model

Flow Regime	As Published	Transition Criteria
Annular	“Fully Developed Annular”	$j_v \geq 2.5, X_{tt} < 1.6$
Wavy	“Wavy-Stratified Flow”	$j_v < 2.5, X_{tt} < 1.6$
Intermittent	“Slug Flow”	$j_v < 2.5, X_{tt} > 1.6, G > G_W$
Stratified	“Stratified”	$j_v < 2.5, X_{tt} > 1.6, G < G_W$
Dispersed	“Bubbly”	Annular, $X_{tt} \gg 1.6$

Comparing the predictions of the Cavallini et al. (2002) model with the data observed, Figure 4.11 and Figure 4.12 below show how the observations at the two saturation temperatures studied align with the model. Note that at this scale, error bars along the vertical axis of mass flux are not visible beneath the data points plotted.

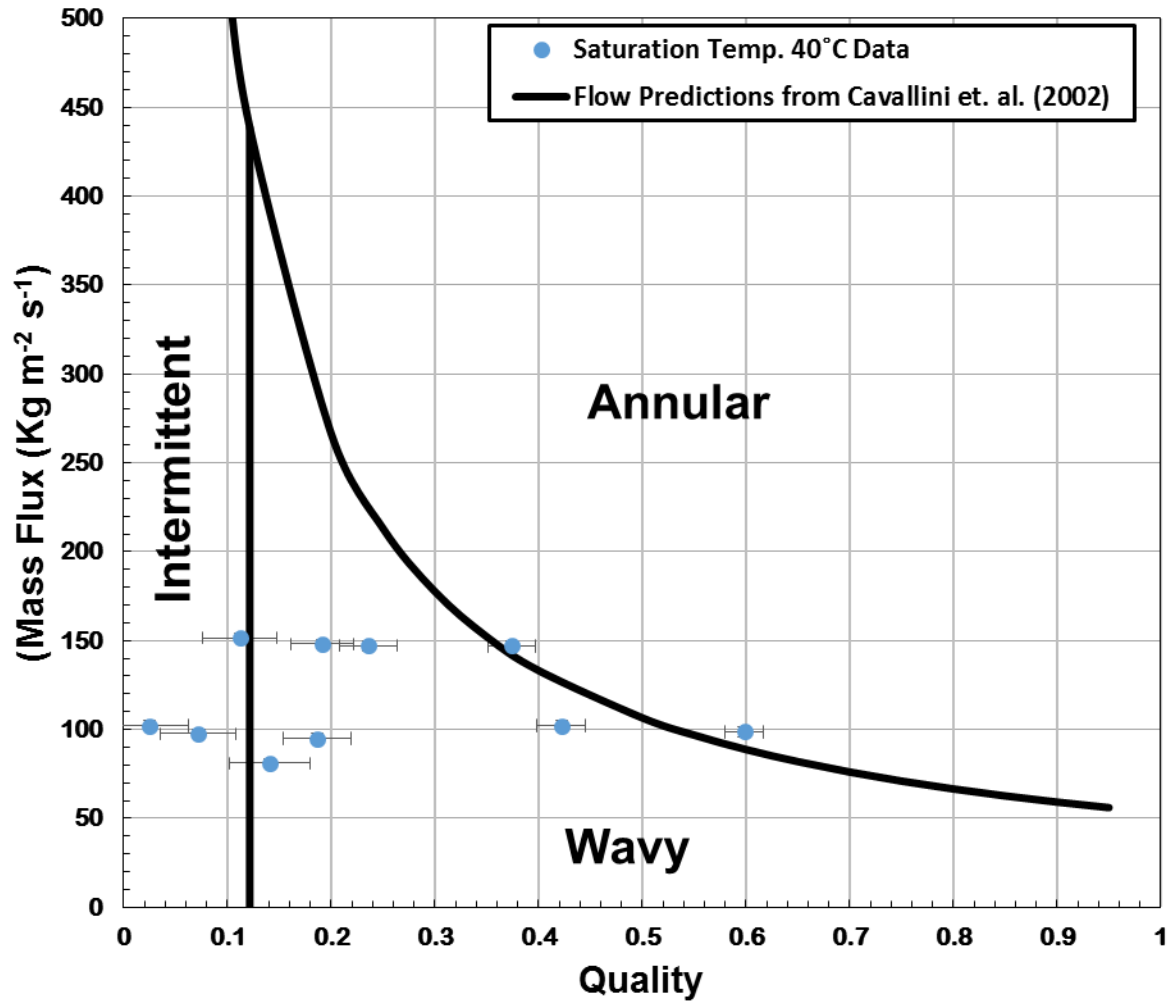


Figure 4.11 - Experimental data ($T_{sat} = 40^\circ\text{C}$) plotted against the Cavallini et al. (2002) proposed map at that temperature

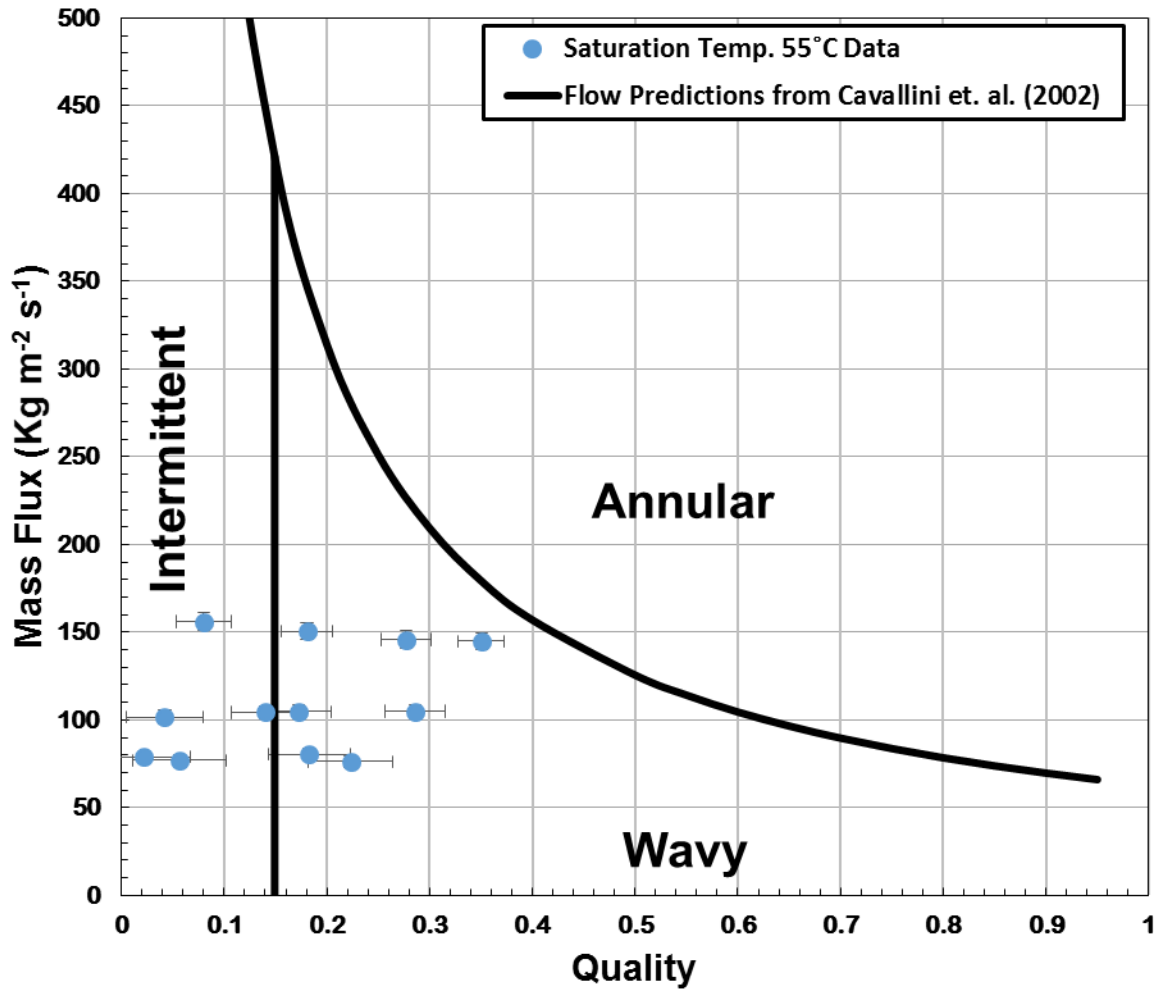


Figure 4.12 - Experimental data ($T_{sat} = 55^{\circ}\text{C}$) plotted against the Cavallini et al. (2002) proposed map at that temperature

Comparison with the model shows that the experimental data is likely well predicted by the Cavallini et al. (2002) map, placing the majority of the data points in the wavy flow regime. While some data points are predicted to be in either intermittent or annular in both saturation temperatures studied, these outliers are still relatively close to the transition lines as well. It cannot however be said with certainty that these predictions are definitely correct, as the data observed could have also been wavy-annular.

4.3.2.3 El Hajal et al. (2003)

The El Hajal et al. (2003) flow map, in contrast to those above, has developed direct correlations for the boundaries of flow regimes, specific to which values of quality and mass flux those transitions occur. The transition lines are presented as the transition mass flux as a function of (among many other parameters) the fluid quality x . Table 4.7 below details the flow regime areas defined by the transition lines of G_{wavy} , G_{mist} , G_{bubbly} , G_{strat} , and x_{IA} . The equations used to define these parameters are defined below in Equations (4.22) through (4.26).

Table 4.7 - Flow transition criteria for the El Hajal (2003) flow model

Flow Regime	As Published	Transition Criteria
Annular	“Annular”	$G > G_{wavy}$, $G < G_{mist}$, and $x > x_{IA}$
Wavy	“Stratified-Wavy Flow”	$G_{strat} < G < G_{wavy}$
Intermittent	“Intermittent”	$G > G_{wavy}$, $G < G_{mist}$ or $G < G_{bubbly}$, and $x < x_{IA}$
Stratified	“Fully Stratified”	$G < G_{strat}$
Mist	“Mist”	$G > G_{mist}$

The equations that define these transitions are presented below:

$$G_{wavy} = \left\{ \frac{16A_{vd}^3 g D_H \rho_l \rho_v}{x^2 \pi^2 [1 - (2h_{ld} - 1)^2]^{0.5}} \left[\frac{\pi^2}{25h_{ld}^2} \left(\frac{We}{Fr} \right)_l^{-1.023} + 1 \right] \right\}^{0.5} + 50 - 75 \exp \left[- (x^2 - 0.97)^2 / x(1-x) \right] \quad (4.22)$$

$$G_{strat} = \left\{ \frac{(226.3)^2 A_{Ld} A_{vd}^2 \rho_v (\rho_l - \rho_v) \mu g}{x^2 (1-x) \pi^3} \right\}^{1/3} + 20x \quad (4.23)$$

$$G_{mist} = \left\{ \frac{7680 A_{vd}^2 g D_H \rho_l \rho_v}{x^2 \pi^2 \left[1.138 + 2 \log \left(\frac{\pi}{1.5 A_{ld}} \right) \right]^{-2}} \left(\frac{Fr}{We} \right)_l \right\}^{0.5} \quad (4.24)$$

$$G_{bubbly} = \left\{ \frac{256 A_{vd} A_{ld}^2 D_H^{1.25} \rho_l (\rho_l - \rho_v) g}{0.3164 (1-x)^{1.75} \pi^2 P_{id} \mu_l^{0.25}} \right\} \quad (4.25)$$

$$x_{IA} = \left\{ \left[0.2914 \left(\frac{\rho_v}{\rho_l} \right)^{-1/1.75} \left(\frac{\mu_l}{\mu_v} \right)^{-1/7} \right] + 1 \right\}^{-1} \quad (4.26)$$

Figure 4.13 and Figure 4.14 below show the comparison between the data collected and modeled expectations as predicted by El Hajal et al. (2003).

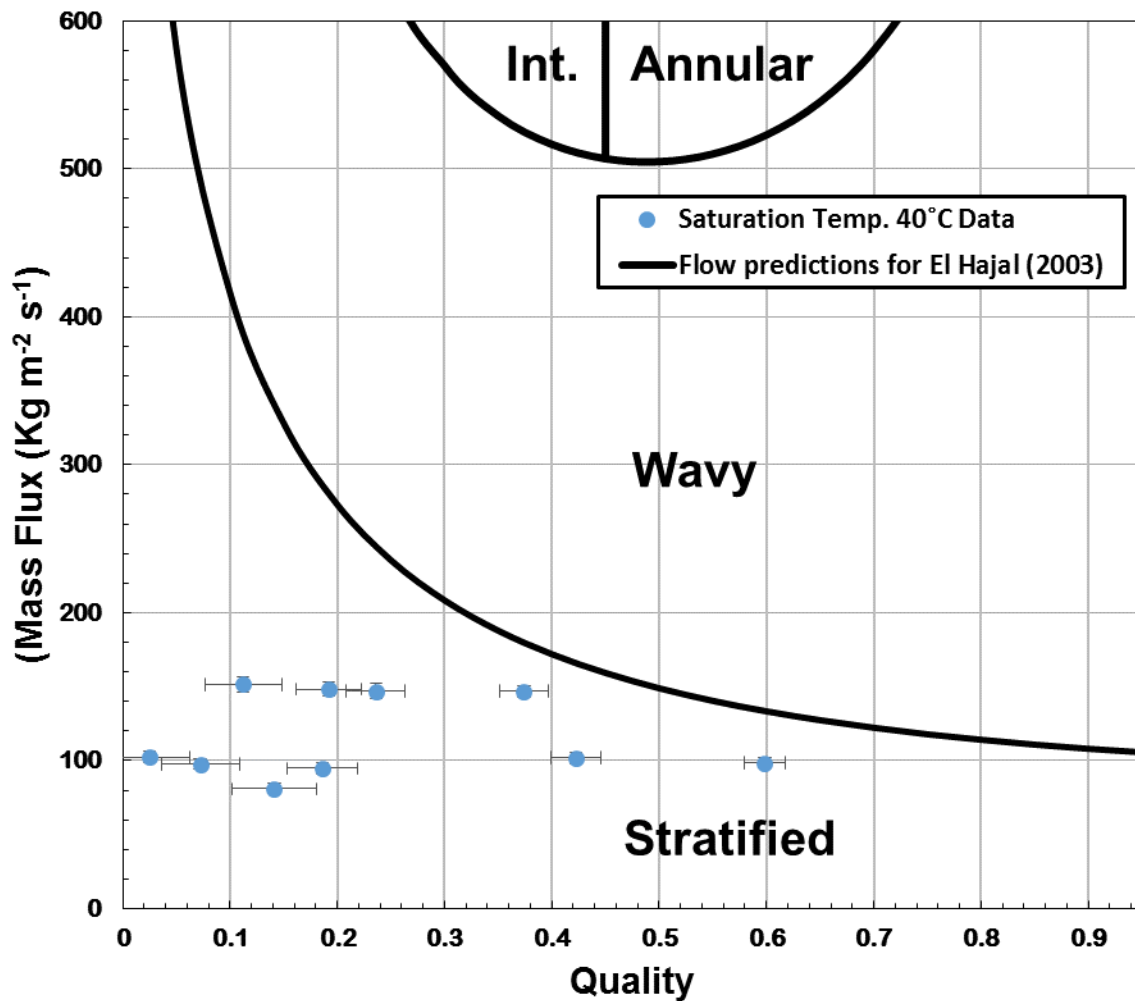


Figure 4.13 - Experimental data ($T_{sat} = 40^\circ\text{C}$) plotted against the El Hajal et al. (2003) proposed map at that temperature

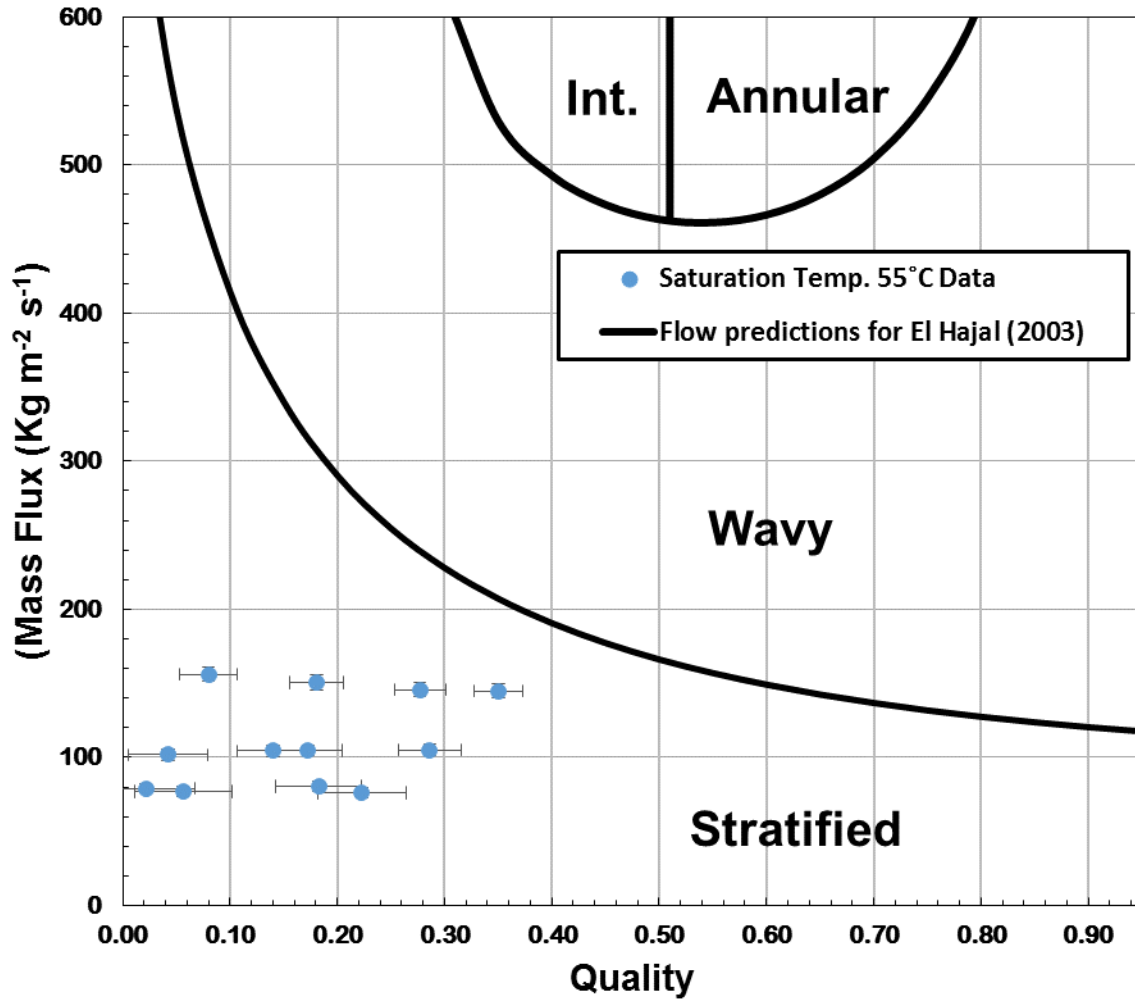


Figure 4.14 - Experimental data ($T_{sat} = 55^{\circ}\text{C}$) plotted against the El Hajal et al. (2003) proposed map at that temperature

The El Hajal et al. (2003) flow map predicts all data points observed in this study to be within the stratified flow regime. While it cannot be confirmed that the flows observed were either stratified-wavy or annular-wavy flows, it was visually apparent that the flows were clearly not smooth, stratified flows. The flow map presented by El Hajal et al. (2003) does not accurately predict the experimental dataset collected.

4.3.2.4 Kim & Mudawar (2012)

The flow model proposed by Kim & Mudawar (2012) makes use of a modified Weber number and Lockhart-Martinelli parameter to fit dimensionless curves to a wide range of data. The modified Weber number used in the model is included below in Equation (4.27). The transition criteria outlined by the publication is presented in Table 4.8.

$$We^* = \begin{cases} 2.45 \frac{Re_v^{0.64}}{Su_{vo}^{0.3} (1 + 1.09 X_{tt}^{0.039})^{0.4}} & \text{for } Re_l \leq 1250 \\ 0.85 \frac{Re_v^{0.79} X_{tt}^{0.157}}{Su_{vo}^{0.3} (1 + 1.09 X_{tt}^{0.039})^{0.4}} \left[\left(\frac{\mu_v}{\mu_l} \right)^2 \left(\frac{\rho_l}{\rho_v} \right) \right]^{0.084} & \text{for } Re_l > 1250 \end{cases} \quad (4.27)$$

Table 4.8 - Flow transition criteria for the Kim & Mudawar flow model

Flow Regime	As Published	Transition Criteria
Annular	“Smooth/Annular”	$We > 90X_{tt}^{0.5}$
Wavy-Annular	“Wavy/Annular”	$24X_{tt}^{0.41} < We < 90X_{tt}^{0.5}$
Transition (A-I)	“Transition”	$7X_{tt}^{0.2} < We < 24X_{tt}^{0.41}$
Intermittent	“Slug”	$We < 7X_{tt}^{0.2}$

The comparison between experimental data and the predictions made by the Kim & Mudawar (2012) model can be seen below in Figure 4.15 and Figure 4.16. Note that due to the bounds of the graphs, the annular region of the model is not visible.

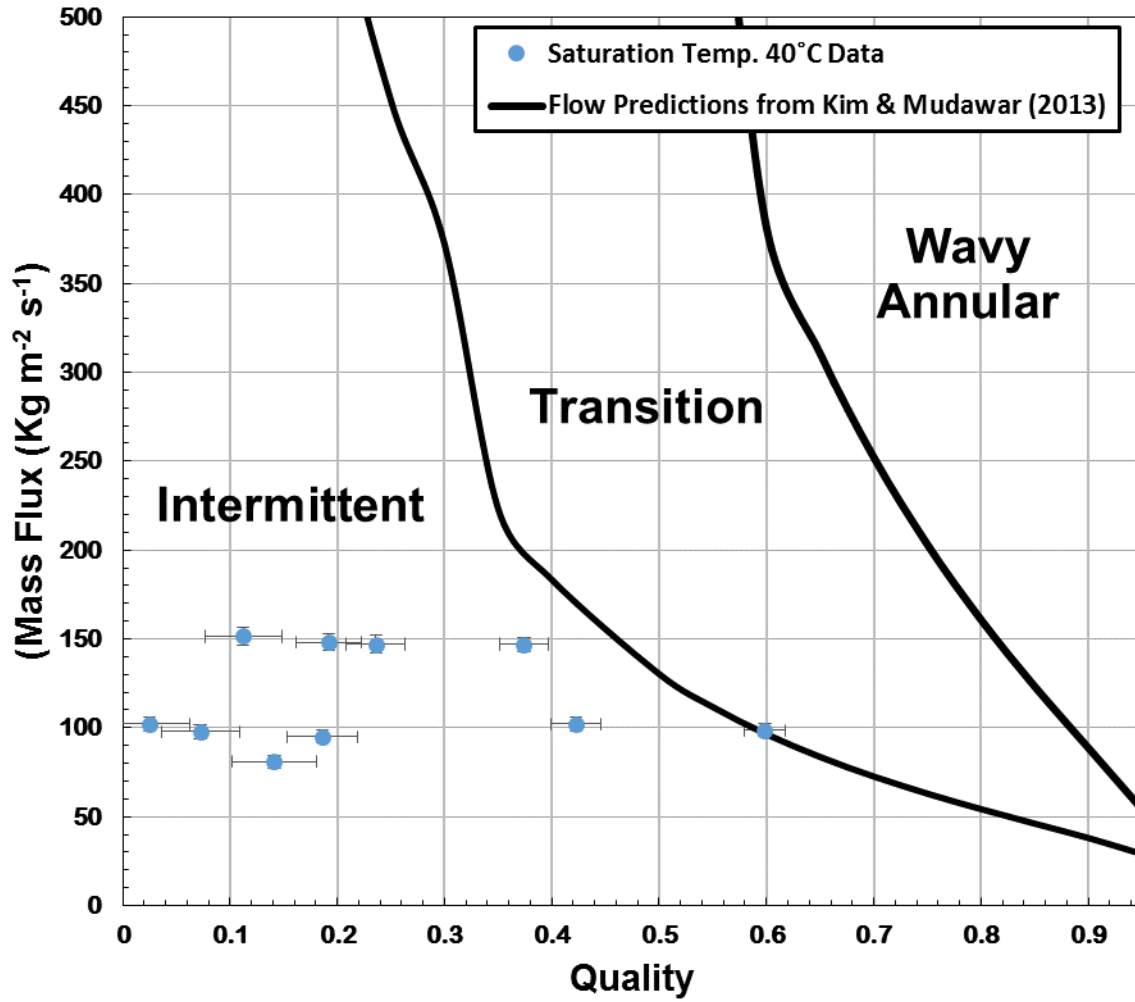


Figure 4.15 - Experimental data ($T_{sat} = 40^\circ\text{C}$) plotted against the Kim & Mudawar (2012) proposed map at that temperature

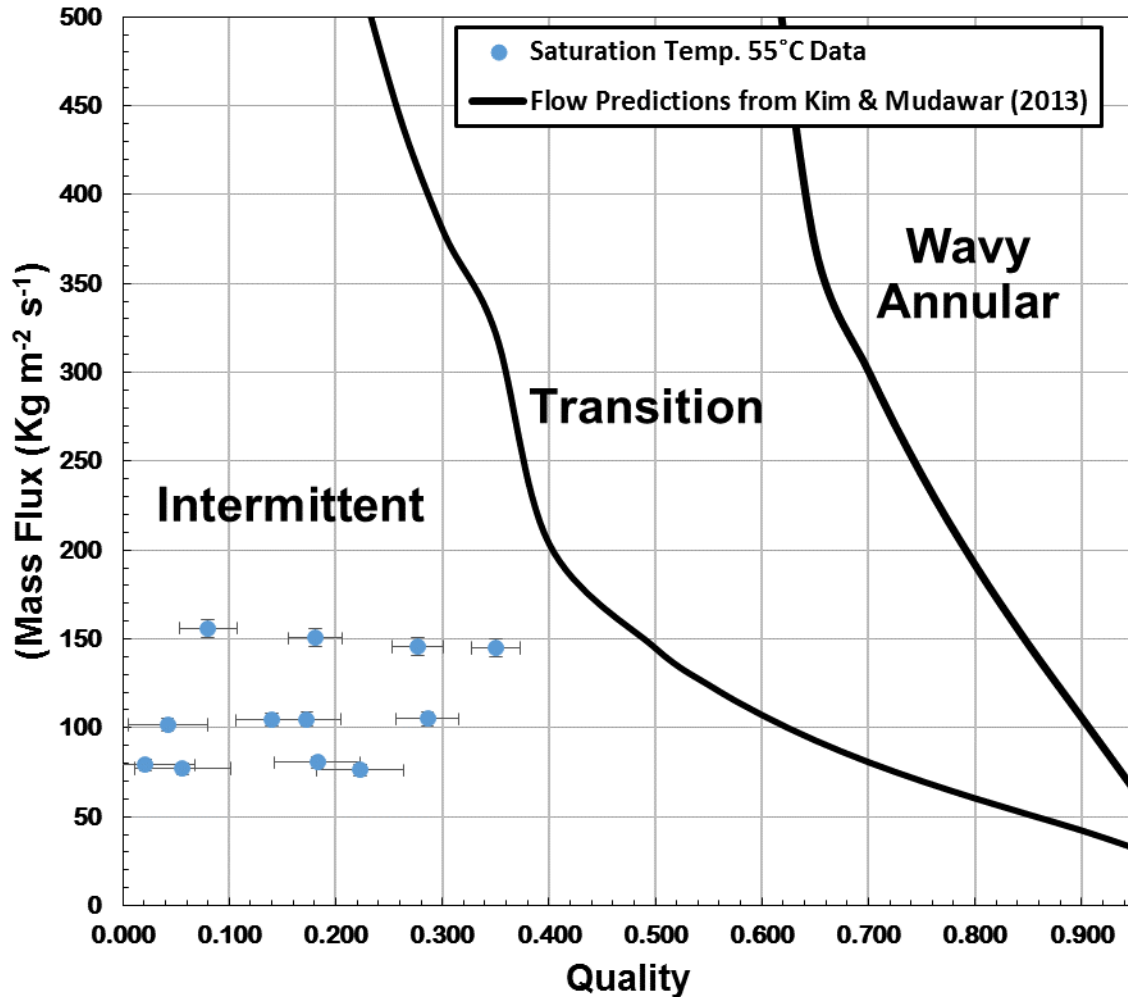


Figure 4.16 - Experimental data ($T_{sat} = 55^{\circ}\text{C}$) plotted against the Kim & Mudawar (2012) proposed map at that temperature

All but one of the data points captured by the present study were expected to be well within the intermittent flow regime. The wavy bend seen in the transition criteria occurring around a quality of 0.3 in both graphs represents the transition region where $Re_L = 1250$, and the transition undergoes a slight discontinuity – shown in the graph as a continuous, and therefore somewhat wavy, function.

While an argument could be made for the observed data representing the wavy-annular regime, no data point was predicted to be within that regime. Comparing the predicted and observed flow regimes, it is clear that the model proposed by Kim & Mudawar (2012) does not well predict the data.

4.3.2.5 Nema et al. (2014)

The flow map proposed by Nema et al. (2014), makes use of the Martinelli parameter, Bond number, Weber number, and dimensionless variable T proposed by Taitel & Dukler (1976) to predict flow regimes in micro and macro scale channels. The map relies on the critical Bond number, as defined by Equation (4.28) below, as a criterion to distinguish between large and small channels, defining where surface tension effects begin to play a significant role in the observed flow regime. The microscale regimes predicted by the Nema flow map are dispersed, annular, intermittent, and mist (presented as *dispersed, annular-film, intermittent annular film, and mist*).

$$Bo_{crit} = \frac{1}{\left(\frac{\rho_l}{\rho_l - \rho_v} - \frac{\pi}{4} \right)} \quad (4.28)$$

The transition criteria for flows in the microscale regime are shown below in Table 4.9, and are a functions of the vapor-phase weber number (We_v), modified Martinelli parameter (X_{tt}), and T parameter as defined by Taitel & Dukler (1976).

Table 4.9 - Microscale transition criteria as proposed by Nema et al. (2014)

Flow Regime	As Published	Transition Criteria
Mist	“Mist”	$We_v > 700, X_{tt} < 0.175$
Dispersed	“Dispersed”	$We_v < 35, X_{tt} > 0.3521, \text{ and } T_G \geq T_{trans}$
Annular	“Annular-Film”	Mist and Dispersed flow are not present, $X_{tt} > 0.3521$, and any We_v
Transition (A-I)	“(A-I) Transition”	$6 \leq We_v < 35, X_{tt} > 0.3521$, and Dispersed flow is not present
Intermittent	“Intermittent Annular Film”	$We_v < 6, X_{tt} > 0.3521$, and Dispersed flow is not present

The vapor phase Weber number, We_v , is defined by Equation (4.29) below.

$$We_v = \frac{\rho_v u_v^2 D_h}{\sigma} \quad (4.29)$$

Calculation of the Bond number and critical Bond number shows the flow regime studied to be well within the microscale predicted by the Nema flow model. Selecting an example data point ($T_{sat} = 40.84^\circ\text{C}$, $x = 0.57$, $G = 102 \text{ kg m}^{-2} \text{ s}^{-1}$), with vapor and liquid densities of 51.33 and 1143 kg m^{-3} respectively, the critical Bond number is calculated to be 3.822 via Equation (4.28). Calculating the measured Bond number for this

data set, as shown below, it is predicted that for this dataset small tube effects would play a role. The same was shown to be true of all data points collected.

$$Bo = \frac{(\rho_l - \rho_v) D_h g}{\sigma} = 1.265$$

Knowing that the dataset is operating in the microscale regime, the remainder of the necessary dimensionless parameters were calculated and compared to the model to make predictions on the expected flow regime of each datapoint. The collected data was plotted against the predictions made by the Nema et al. (2014) model, and are shown below in Figure 4.17 and Figure 4.18.

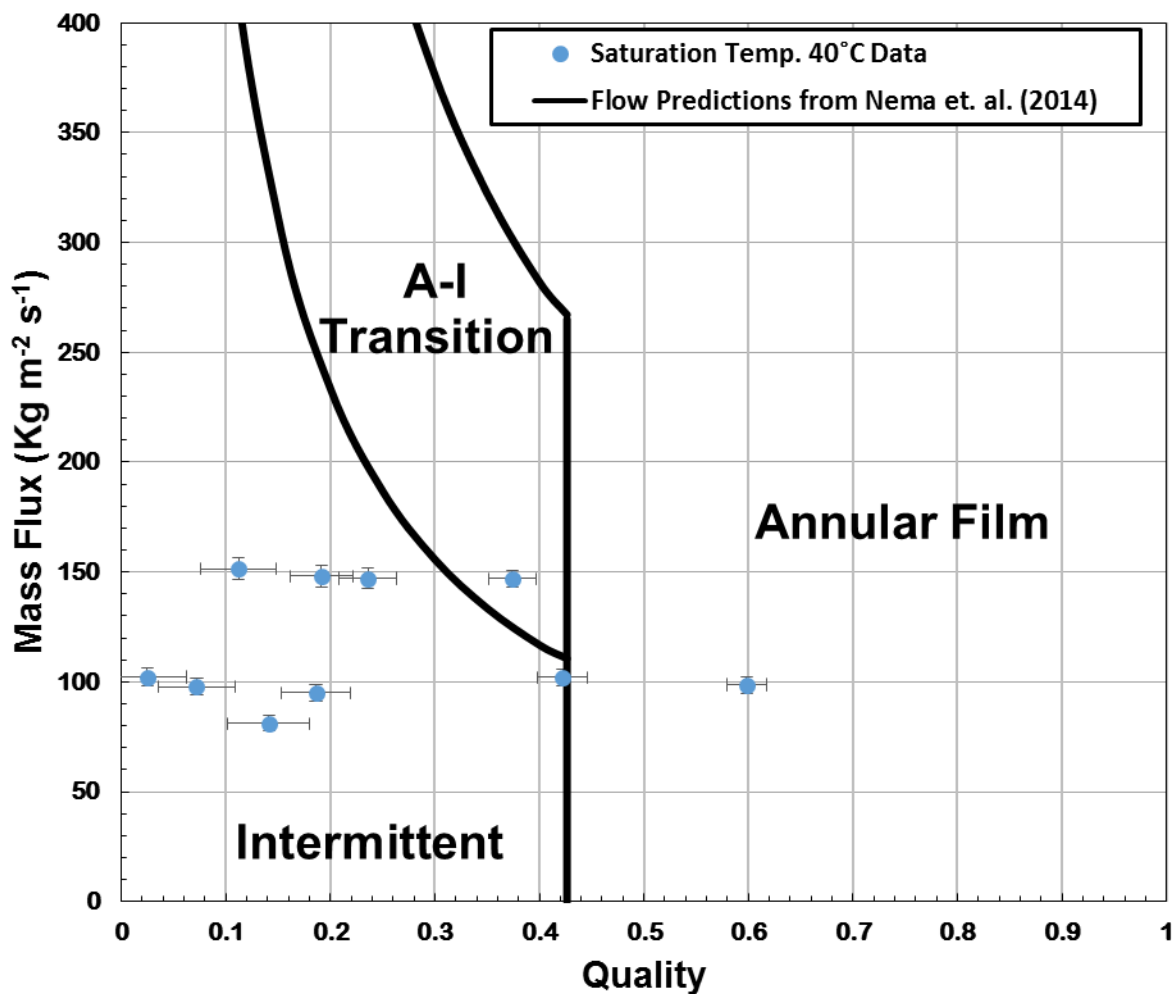


Figure 4.17 - Experimental data ($T_{sat} = 40^{\circ}\text{C}$) plotted against the Nema et al. (2014) proposed map at that temperature

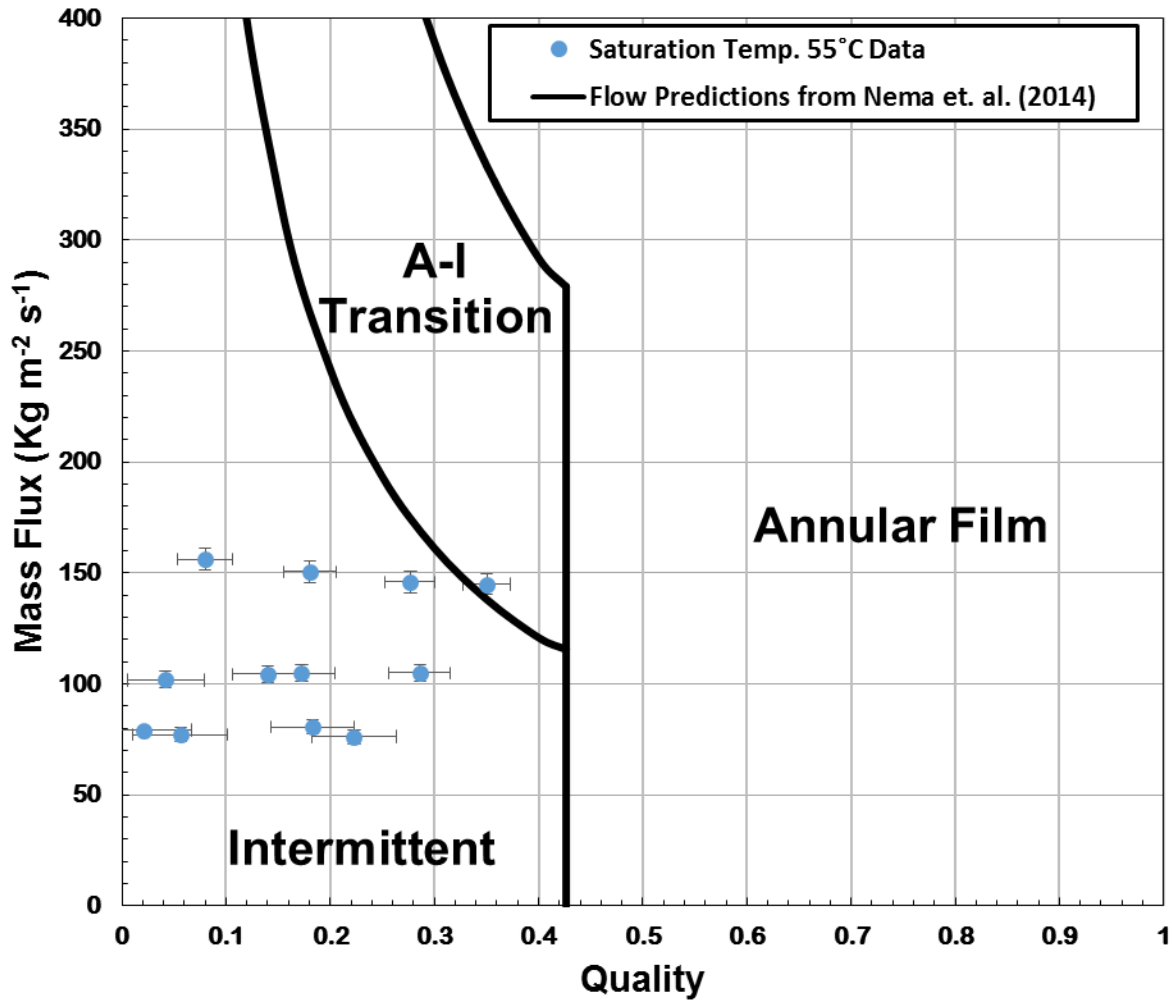


Figure 4.18 - Experimental data ($T_{sat} = 55^{\circ}\text{C}$) plotted against the Nema et al. (2014) proposed map at that temperature

The model predicted a majority (86%) of the data to be within the intermittent regime, as was originally expected during the development of the present study. Notice that of the three flow regimes predicted by the model, none of the three were observed in the present research. Due to the scaling of the figures, the mist and dispersed flow regime predictions are not visible.

4.4 SUMMARY

Of the flow maps considered, flow was predicted to be stratified, wavy, annular, intermittent or dispersed. Many of the flow maps predicted some percentage of the points to be intermittent flow, seen below in Table 4.10. As evident by the photo and video data, there were no data points clearly in the intermittent flow regime. This over prediction of intermittent flow is important, as the heat transfer and pressure drop mechanisms for intermittent versus annular and wavy flow are significantly different, and different types of mechanistic models would be developed and used. It is also interesting to note that none of the models exhibited particularly good agreement with one another for the range of conditions considered in this study. These results suggest that further work is required to refine flow transition criteria of refrigerants at low mass fluxes.

Table 4.10 - Summary of flow regime predictions by maps investigated

Proposed Model	Percent of data predicted to be within designated flow regime					
	Stratified	Wavy	Annular	Intermittent	Dispersed	Mist
Taitel & Dukler (1976)	0%	0%	36%	50%	14%	0%
Cavallini et al. (2002)	0%	55%	9%	36%	0%	0%
El Hajal et al. (2003)	100%	0%	0%	0%	0%	0%
Kim & Mudawar (2013)	0%	0%	0%	100%	0%	0%
Nema et al. (2014)	0%	0%	14%	86%	0%	0%

5 CONCLUSION & RECOMMENDATIONS

5.1 CONCLUSIONS

In the present study, a test bed was developed capable of high speed visualization and measurement of adiabatic two-phase fluid flow through microchannels at low mass fluxes. The test bed was used to collect data ($75 < G < 150 \text{ kg m}^{-2} \text{ s}^{-1}$, $0.05 < x < 0.75$, $D_h = 0.842 \text{ mm}$) at two different saturation temperatures ($T_{\text{sat}} = 40, 55 \text{ }^\circ\text{C}$) to validate the accuracy of a variety of flow maps when applied to fluid flow in microchannels at such low mass fluxes. While visualization was captured only from above the test section, all data points appeared to be the same flow regime of either wavy-annular or wavy-stratified flow.

5.1.1 EXPERIMENT

The test bed consisted of three major components – the working fluid loop, cooling fluid loop, and test section. The working fluid loop was charged with R-134a and was used to pump a measured flowrate of superheated refrigerant into the test section at a known temperature and pressure. An inline cartridge heater was used to control the fluid temperature, controlled by a variable voltage source and measured via thermocouples swaged into the system.

Upon entering the test section, fluid was condensed to a desired state via the cooling loop, acting as a counterflow heat exchanger upon the underside of the test section. Deionized water was used as the source of cooling fluid, chilled via a counterflow tube-in-tube heat exchanger with high mass-flux fluid from a chiller, supplied at 5°C . The water flowrate was supplied via a syringe pump, working as both a pump and a volumetric flow meter, and the temperature of the water was measured at test section inlet and outlet. Using the ΔT measured across the water supply, the amount of enthalpy absorbed from the system could be known, and the quality of flow entering the viewing section known.

With the superheated vapor entering the test section cooled to the saturation temperature, and then brought to the desired thermodynamic quality, the flow entered an adiabatic length of test section. The test section was constructed as a layered series of plates to allow for both the inlet and outlet of both working and cooling fluids, as well as the viewing of the adiabatic length of flow. An aluminum plate with microchannel features machined into one face was sandwiched between a polycarbonate viewing plate (sealing off the open face microchannels) and a Delrin® base with flow features for the cooling fluid to run along the opposite face of the aluminum plate. By condensing the superheated vapor inside the test section, optimal distribution of fluid mass could be achieved prior to the fluid becoming a two-phase mixture of differing densities, avoiding the issue of maldistribution.

5.1.2 SETUP

A Phantom v310 high speed camera was suspended above the exposed viewing face of the test section (all else being heavily insulated) to capture visualization footage of the flow data points. Three separate 500 W halogen lamps, as well as a diffusive photopaper screen, were used to illuminate the test section during photo capture. Flow data was collected using a custom LabVIEW VI capable of making live estimations of flow quality and mass flux, with visual data being recorded using the Phantom PCC software.

5.1.3 RESULTS

Flow results from the data collected were compared to flow maps presented by a variety of authors, with none of the maps accurately predicting the flow regimes observed. While the flow map presented by Cavallini et al. (2002) predicts the majority of the data points to be within the wavy regime, data was also predicted to be within the annular and intermittent regimes as well, with neither of those flow types being observed.

5.1.4 RESULT CONCLUSION

With the little amount of agreement between the most commonly used flow maps and the empirical data captured in the present study, it is clear that further development is required in order for the predictive models to accurately model microchannel flow of low surface tension fluids at such low mass fluxes. Additionally, a wider variety of data is required to determine the conditions under which transition to flows such as intermittent and stratified occur. While the data collected provide little evidence of where these transitions can be expected, it is clear that the present models do not properly predict the effect of scaling variables to flows of this nature.

5.2 RECOMMENDATIONS FOR FUTURE WORK

While the primary goal of this work was in the development of a test bed capable of measuring and visualizing flows, the work has identified a large host of additional work that could be performed to better understand two-phase microchannel flows. The following are a few considerations to make in pursuing future work:

- Exploration of additional data points, both at lower and higher mass fluxes to determine the conditions under which flow regime transition can be expected in the given test section geometry
- Observation of flow from a horizontal viewpoint, with channels arranged vertically to allow for the distinction between stratified and annular flow regimes
- Characterization of flow heat transfer and pressure drop, in comparison to presently used models to qualify the validity of those commonly accepted by industry

6 SOURCES CITED

- Agarwal, Akhil, and Srinivas Garimella. 2010. "Representative Results for Condensation Measurements at Hydraulic Diameters ~100 Microns." *Journal of Heat Transfer* 132 (4): 041010. doi:10.1115/1.4000879.
- Akers, W.W., and H.F Rosson. 1960. "Condensation inside a Horizontal Tube." In *Chem. Eng. Prog. Symp.* 56, 145–49.
- Baird, J. R., D. F. Fletcher, and B. S. Haynes. 2003. "Local Condensation Heat Transfer Rates in Fine Passages." *International Journal of Heat and Mass Transfer* 46 (23): 4453–66. doi:10.1016/S0017-9310(03)00287-4.
- Baker, Ovid. 1954. "Simultaneous Flow of Oil and Gas." *The Oil and Gas Journal*, 185–95.
- Barnea, D., Y. Luninski, and Y. Taitel. 1983. "Flow Pattern in Horizontal and Vertical Two Phase Flow in Small Diameter Pipes." *The Canadian Journal of Chemical Engineering* 61 (October): 617–20. doi:10.1002/cjce.5450610501.
- Brauner, N, and David M Maron. 1992. "Flow Pattern Transitions in Two-Phase Liquid-Liquid Flow in Horizontal Tubes." *International Journal of Multiphase Flow* 18 (1): 123–40.
- Brauner, N., and D. Moalem Maron. 1992. "Flow Pattern Transitions in Two-Phase Liquid-Liquid Flow in Horizontal Tubes." *Int. J. Multiphase Flow* 18 (1): 123–40.
- Breber, G., J.W. Palen, and J. Taborek. 1980. "Prediction of Horizontal Tubeside Condensation of Pure Components Using Flow Regime Criteria." *Journal of Heat Transfer* 102 (3): 471–76. doi:10.1115/1.3244325.
- Canière, H, C T'Joen, a Willockx, M De Paepe, M Christians, E Van Rooyen, L Liebenberg, and J P Meyer. 2007. "Horizontal Two-Phase Flow Characterization for Small Diameter Tubes with a Capacitance Sensor." *Measurement Science and Technology* 18 (9): 2898–2906. doi:10.1088/0957-0233/18/9/020.
- Cavallini, A., G. Censi, D. Del Col, L. Doretti, G. A. Longo, and L. Rossetto. 2001. "Experimental Investigation on Condensation Heat Transfer and Pressure Drop of New HFC Refrigerants (R134a, R125, R32, R410A, R236ea) in a Horizontal Smooth Tube." *International Journal of Refrigeration* 24 (1): 73–87. doi:10.1016/S0140-7007(00)00070-0.
- Cavallini, Alberto, Giuseppe Censi, Davide Del Col, Luca Doretti, Giovanni Longo, and Luisa Rossetto. 2002. "Condensation of Halogenated Refrigerants Inside Smooth Tubes." *HVAC&R Research* 8 (4):

429–51. doi:10.1080/10789669.2002.10391299.

Cavallini, Alberto, Davide Del Col, Luca Doretti, Marko Matkovic, Luisa Rossetto, Claudio Zilio, and Giuseppe Censi. 2006. “Condensation in Horizontal Smooth Tubes: A New Heat Transfer Model for Heat Exchanger Design.” *Heat Transfer Engineering* 27 (8): 31–38. doi:10.1080/01457630600793970.

Chai, Wai Siong, Kean How Cheah, Kai Seng Koh, Jitkai Chin, and Tengku Farah Wahida K. Chik. 2016. “Parametric Studies of Electrolytic Decomposition of Hydroxylammonium Nitrate (HAN) Energetic Ionic Liquid in Microreactor Using Image Processing Technique.” *Chemical Engineering Journal* 296. Elsevier B.V.: 19–27. doi:10.1016/j.cej.2016.03.094.

Coleman, John W., and Srinivas Garimella. 1999. “Characterization of Two-Phase Flow Patterns in Small Diameter Round and Rectangular Tubes.” *International Journal of Heat and Mass Transfer* 42 (15): 2869–81. doi:10.1016/S0017-9310(98)00362-7.

———. 2000. “Two-Phase Flow Regime Transitions in Microchannel Tubes: The Effect of Hydraulic Diameter.” *ASME-PUBLICATIONS-HTD*.
<http://scholar.google.com/scholar?hl=en&btnG=Search&q=intitle:two-phase+flow+regime+transitions+in+microchannel+tubes-+effect+of+hydrolic+diameter#0>.

———. 2003. “Two-Phase Flow Regimes in Round, Square and Rectangular Tubes during Condensation of Refrigerant R134a.” *International Journal of Refrigeration* 26: 117–28. <http://www.sciencedirect.com/science/article/pii/S0140700702000130>.

Damianides, C. A., and J. W. Westwater. 1988. “Two-Phase Flow Patterns in a Compact Heat Exchanger and in Small Tubes.” In , 1257–68.

DEA. 2016. DEA Nutating Flowmeter, issued 2016.

Dobson, M K, and J C Chato. 1998. “Condensation in Smooth Horizontal Tubes.” *Journal of Heat Transfer* 120 (1): 193–213. <http://dx.doi.org/10.1115/1.2830043>.

Dobson, M.K. 1994. “Heat Transfer and Flow Regimes During Condensation in Horizontal Tubes.” University of Illinois, Urbana-Champaign, IL.

Doretti, L., C. Zilio, S. Mancin, and A. Cavallini. 2013. “Condensation Flow Patterns inside Plain and Microfin Tubes: A Review.” *International Journal of Refrigeration* 36 (2). Elsevier Ltd and IIR: 567–87. doi:10.1016/j.ijrefrig.2012.10.021.

- DuPont. 2016. "DuPont HFC-134a Properties, Uses, Storage, and Handling."
- EdgeCam. 2014. "EdgeCam."
- El Hajal, J., J. R. Thome, and A. Cavallini. 2003. "Condensation in Horizontal Tubes, Part 1: Two-Phase Flow Pattern Map." *International Journal of Heat and Mass Transfer* 46 (18): 3349–63. doi:10.1016/S0017-9310(03)00139-X.
- Engineers Edge. 2016. "Bending, Deflection and Stress Equations Calculator for Fixed at Both Ends with Uniform Loading."
- F. P. Bretherton. 1961. "The Motion of Long Bubbles in Tubes." *Journal of Fluid Mechanics* 10 (02): 166–88.
- F-Chart Software. 2016. "Engineering Equation Solver."
- Fukano, T., A. Kariyasaki, and M. Kagawa. 1989. "Flow Patterns and Pressure Drop in Isothermal Gas–liquid Cocurrent Flow in a Horizontal Capillary Tube." In *ANS Proceedings of National Heat Transfer Conference: Technical Sessions*, 153–61.
- Govier, G. W., and K. Aziz. 1972. "The Flow of Complex Mixtures in Pipes." Van Nostrand-Reinhold, New York.
- Griffith, P, and K Lee. 1964. "The Stability of an Annulus of Liquid in a Tube." *Journal of Basic Engineering* 86: 666.
- Jassim, E.W., T.A. Newell, and J.C. Chato. 2006. "Probabilistic Determination of Two-Phase Flow Regimes Utilizing an Automated Image Recognition Technique." In *International Refrigeration and Air Conditioning Conference*, 1–8. <http://docs.lib.purdue.edu/cgi/viewcontent.cgi?article=1825&context=iracc>.
- Jassim, E.W., T.a. Newell, and J.C. Chato. 2007. "Prediction of Two-Phase Condensation in Horizontal Tubes Using Probabilistic Flow Regime Maps." *International Journal of Heat and Mass Transfer* 51 (3-4): 485–96. doi:10.1016/j.ijheatmasstransfer.2007.05.021.
- Kattan, N, John R. Thome, and D Favrat. 1998. "Flow Boiling in Horizontal Tubes: Part 1–Development of a Diabatic Two-Phase Flow Pattern Map." *Journal of Heat Transfer* 120 (1): 140–47.
- Kawahara, A, PMY Chung, and M Kawaji. 2002. "Investigation of Two-Phase Flow Pattern, Void Fraction and Pressure Drop in a Microchannel." *International Journal of Multiphase ...* 28: 1411–35. <http://www.sciencedirect.com/science/article/pii/S030193220200037X>.

- Keinath, Brendon. 2012. "Void Fraction, Pressure Drop, and Heat Transfer in High Pressure Condensing Flows through Microchannels." Georgia Institute of Technology.
- Kim, Sung Min, and Issam Mudawar. 2012. "Flow Condensation in Parallel Micro-Channels - Part 2: Heat Transfer Results and Correlation Technique." *International Journal of Heat and Mass Transfer* 55 (4). Elsevier Ltd: 984–94. doi:10.1016/j.ijheatmasstransfer.2011.10.012.
- . 2013. "Universal Approach to Predicting Heat Transfer Coefficient for Condensing Mini/micro-Channel Flow." *International Journal of Heat and Mass Transfer* 56 (1-2). Elsevier Ltd: 238–50. doi:10.1016/j.ijheatmasstransfer.2012.09.032.
- Kline, S. J., and F. A. McClintock. 1953. "Describing Uncertainties in Single Sample Experiments." *Mechanical Engineering*.
- Koyama, S, K Kuwara, and K Nakashita. 2003. "Condensation of Refrigerant in a Multi-Port Channel." In *ASME 2003 1st International Conference on Microchannels and Minichannels*, 193–205.
- Mandhane, J.M., G.A. Gregory, and K. Aziz. 1974a. "A Flow Pattern Map for Gas—liquid Flow in Horizontal Pipes." *International Journal of Multiphase Flow* 1 (4). Pergamon: 537–53. doi:10.1016/0301-9322(74)90006-8.
- . 1974b. "A Flow Pattern Map for Gas—liquid Flow in Horizontal Pipes." *International Journal of Multiphase Flow* 1 (4): 537–53. doi:10.1016/0301-9322(74)90006-8.
- Mas, Nuria De, and A Günther. 2003. "Microfabricated Multiphase Reactors for the Selective Direct Fluorination of Aromatics." *Industrial & Engineering ...*, 698–710. <http://pubs.acs.org/doi/abs/10.1021/ie020717q>.
- Matkovic, Marko, Alberto Cavallini, Davide Del Col, and Luisa Rossetto. 2009. "Experimental Study on Condensation Heat Transfer inside a Single Circular Minichannel." *International Journal of Heat and Mass Transfer* 52 (9-10). Elsevier Ltd: 2311–23. doi:10.1016/j.ijheatmasstransfer.2008.11.013.
- Moser, K. W., R. L. Webb, and B. Na. 1998. "A New Equivalent Reynolds Number Model for Condensation in Smooth Tubes." *Journal of Heat Transfer* 120 (2): 410–17. doi:10.1115/1.2824265.
- National Instruments. 2016. "LabVIEW."
- Nema, Gaurav, Srinivas Garimella, and Brian M. Fronk. 2014. "Flow Regime Transitions during Condensation in Microchannels." *International Journal of Refrigeration* 40 (April). Elsevier Ltd and IIR: 227–40. doi:10.1016/j.ijrefrig.2013.11.018.

- Niño, VG, PS Hrnjak, and TA Newell. 2003. "Two-Phase Flow Visualization of R134A in a Multiport Microchannel Tube." *Heat Transfer Engineering*. <http://www.tandfonline.com/doi/abs/10.1080/01457630304042>.
- NIST. 2013. "NIST Standard Reference Database 23: Reference Fluid Thermodynamic and Transport Properties-REFPROP."
- Ong, C. L., and J. R. Thome. 2010. "Macro-to-Microchannel Transition in Two-Phase Flow: Part 1 - Two-Phase Flow Patterns and Film Thickness Measurements." *Experimental Thermal and Fluid Science* 35 (1). Elsevier Inc.: 37–47. doi:10.1016/j.expthermflusci.2010.08.004.
- Rabas, T. J., and Bayram Arman. 2000. "Effect of the Exit Condition on the Performance of In-Tube Condensers." *Heat Transfer Engineering* 21 (1): 4–14. doi:10.1080/014576300271112.
- Sacks, P.S. 1975. "Measured Characteristics of Adiabatic and Condensing Single Component Two-Phase Flow of Refrigerant in a 0.377 In. Diameter Horizontal Tube." In *ASME Winter Annual Meeting, 75-WA/HT-24 Houston, Texas*.
- Shah, M. M. 1979. "A General Chart Correlation for Heat Transfer during Condensation Inside Pipes." *International Journal of Heat and Mass Transfer* 22: 547–56.
- Steiner, D. 1993. *Heat Transfer to Boiling Saturated Liquids. VDI Heat Atlas*.
- Suo, Mikio, and Peter Griffith. 1964. "Two-Phase Flow in Capillary Tubes." *Journal of Fluids Engineering*. <http://fluidsengineering.asmedigitalcollection.asme.org/article.aspx?articleid=1431728>.
- Systemes, Dassault. 2014. "Solidworks." Dassault Systemes.
- Taitel, Y., and A. E. Dukler. 1976. "A Model for Predicting Flow Regime Transitions in Horizontal and near Horizontal Gas-liquid Flow." *AIChE Journal* 22 (1): 47–55. <http://onlinelibrary.wiley.com/doi/10.1002/aic.690220105/pdf>.
- Tandon, T.N., H.K. Varma, and C.P. Gupta. 1982. "A New Flow Regime Map for Condensation inside Horizontal Tubes." *Journal of Heat Transfer* 104: 763–68.
- Thome, J.R., J. El Hajal, and A. Cavallini. 2003. "Condensation in Horizontal Tubes, Part 2: New Heat Transfer Model Based on Flow Regimes." *International Journal of Heat and Mass Transfer* 46 (18): 3365–87.
- Triplett, KA, and SM Ghiaasiaan. 1999. "Gas-liquid Two-Phase Flow in Microchannels Part I: Two-Phase Flow Patterns." *International Journal of Multiphase Flow* 25: 377–94.

<http://www.sciencedirect.com/science/article/pii/S0301932298000548>.

VanderPutten, Michael. 2016. "Analysis of Heat Rejection in Space Using Capillary Pumped Systems." In *2016 AIAA Region VI Student Paper Conference*, 1–11. Corvallis, OR.

Waelchli, Severin, and Philipp Rudolf von Rohr. 2006. "Two-Phase Flow Characteristics in Gas–liquid Microreactors." *International Journal of Multiphase Flow* 32 (7): 791–806. doi:10.1016/j.ijmultiphaseflow.2006.02.014.

Weisman, J, D Duncan, J Gibson, and T Crawford. 1979. "Effects of Fluid Properties and Pipe Diameter on 2-Phase Flow Patterns in Horizontal Lines." *International Journal of Multiphase Flow* 5 (6): 437–62. doi:10.1016/0301-9322(79)90031-4.

Yang, CY, and CC Shieh. 2001. "Flow Pattern of Air–water and Two-Phase R-134a in Small Circular Tubes." *International Journal of Multiphase Flow* 27. <http://www.sciencedirect.com/science/article/pii/S0301932200000707>.

Zhao, TS, and QC Bi. 2001. "Co-Current Air–water Two-Phase Flow Patterns in Vertical Triangular Microchannels." *International Journal of Multiphase Flow* 27: 765–82. <http://www.sciencedirect.com/science/article/pii/S0301932200000513>.

7 APPENDIX

Table 7.1 - Measured and calculated values of data points used in study

Calculated Variables						Measured Variables						
Saturation Temperature [°C]	Thermo-dynamic Quality	Mass Flux [kg·m ⁻² ·s ⁻¹]	Test Section Heat Loss [W]	Fluid Superheat [°C]	System Pressure [PSI]	Pump Temp. [°C]	Fluid Flow Rate [ml/min]	T _{f,in} [°C]	T _{f,out} [°C]	Water Flow Rate [ml/min]	T _{w,in} [°C]	T _{w,out} [°C]
40.54	0.60	98.66	-4.10	6.23	149.70	12.10	16.72	46.77	39.86	10.00	11.33	42.12
40.84	0.42	102.10	-4.45	6.86	150.90	12.12	17.30	47.69	40.16	15.00	10.06	41.28
41.49	0.14	81.00	-5.86	13.35	153.50	12.16	13.73	54.83	40.75	17.00	10.13	42.78
41.44	0.19	94.97	-4.55	6.10	153.30	12.02	16.09	47.54	40.63	20.00	10.08	40.60
41.00	0.07	97.74	-4.41	6.05	151.50	11.90	16.56	47.05	40.19	25.00	10.42	39.47
39.92	0.02	102.20	-4.37	7.61	147.20	11.84	17.30	47.54	39.18	30.00	10.71	37.93
39.15	0.37	147.00	-4.76	11.49	144.20	11.19	24.86	50.65	38.23	29.50	10.96	38.22
40.47	0.24	147.10	-4.85	9.36	149.40	10.87	24.84	49.83	39.57	37.00	11.84	37.49
40.29	0.19	148.20	-5.12	11.00	148.70	10.77	25.02	51.29	39.44	43.00	12.69	36.45
40.05	0.11	151.50	-4.73	9.36	147.70	10.62	25.57	49.40	39.11	55.00	13.88	34.63
55.36	0.08	156.10	-2.36	8.55	218.30	11.06	26.33	63.90	54.65	27.00	11.12	52.86
55.35	0.18	150.50	-2.03	9.21	218.30	11.27	25.40	64.56	54.64	22.50	10.43	54.12
55.12	0.28	145.80	-1.60	10.35	217.10	11.45	24.63	65.47	54.42	19.00	10.55	56.07
55.80	0.35	144.90	-1.65	8.82	220.70	11.39	24.46	64.62	55.13	16.50	10.34	56.46
55.92	0.04	101.70	-1.35	9.40	221.30	12.19	17.20	65.32	55.21	17.00	10.28	55.46
54.96	0.14	104.40	-2.67	8.35	216.20	12.35	17.68	63.31	54.34	15.50	10.71	55.35
55.78	0.17	104.80	-2.77	6.46	220.60	12.35	17.74	62.24	55.17	14.50	10.79	55.67
55.18	0.29	105.00	-2.69	7.98	217.40	12.33	17.78	63.16	54.47	13.00	10.78	55.25
55.99	0.22	76.20	-1.93	7.49	221.70	12.54	12.91	63.48	55.40	10.00	12.11	57.12
55.88	0.18	80.51	-2.16	7.37	221.10	12.49	13.64	63.24	55.20	11.00	11.75	57.04
56.12	0.06	77.09	-2.40	6.41	222.40	12.40	13.05	62.53	55.50	12.00	11.53	56.42
55.77	0.02	79.08	-2.21	7.69	220.60	12.38	13.39	63.47	54.97	13.00	11.37	56.43